

# **POLITECNICO DI TORINO**

Department of Mechanical and Aerospace Engineering

**Master of Science in Mechanical Engineering**

Master's degree Thesis

## **OPTIMISATION OF COPPER PRODUCTION BY LASER POWDER BED FUSION (L-PBF)**



**Supervisors:**

prof. Manuela Galati

prof. Abdollah Saboori

**Candidate:**

Marta Roccetti Campagnoli

April 2021

# Abstract

Additive Manufacturing (AM) refers to a family of layer-upon-layer building technologies capable of producing geometrically intricate parts in a single step. In the last twenty years, it has gained a huge interest in both academia and industry. Today still, the processability of many materials through AM is under development. One of the most interesting studies concerns the adoption of copper, a metal characterized by high thermal and electrical conductivity.

The first part of this thesis presents a global review of the current state of art on copper's manufacturing through AM. In the pages that follow, the main studies conducted so far concerning this issue are reported. As a result, all the challenges that arise in copper processing and the solutions proposed to overcome them and realize high-quality copper components are exposed.

Further, in the present experimental activity, a new material solution is proposed in order to improve the processability of copper powder through Laser Powder Bed Fusion (LPBF). The idea is to add graphite to copper powder. As a matter of fact, graphite reduces thermal expansion and improves the thermal conductivity of copper. Due to graphite's higher laser absorption rate, the resultant mixture should be easier to manufacture through laser techniques. Thus, graphite can be one of the best candidates to improve the processability of copper powder significantly through Laser AM (LAM). At the same time, the spreadability of the mixture can be negatively affected by the elevated lubricant property of graphite. In addition, if the quantity of graphite added is too much, Van der Waals forces will induce agglomerations. Finally, the addition of a small quantity of an alloying element would also drastically decrease copper's electrical conductivity. Consequently, it is fundamental to choose the quantity of graphite to be added carefully. So far, however, very little attention has been paid to the role of graphite added to the copper powder. The central thesis of this experimental work is to study the effects of the addition of different amounts of graphite to copper powder and to define the processing parameters suitable to produce copper 3D printed components.

# Contents

<b>Abstract</b> .....	2
<b>Contents</b> .....	3
<b>Chapter 1</b> .....	5
<b>Introduction</b> .....	5
1.1. Additive Manufacturing.....	5
1.1.1. Advantages and disadvantages of AM.....	7
1.1.2. Applications.....	9
1.1.3. Metal AM.....	12
1.1.3.1. Powder for PBF.....	12
1.2. On the processability of Copper parts via AM; Potentials, challenges and feasible solutions.....	14
1.2.1. Additive Manufacturing of Copper.....	16
1.2.1.1. LPBF.....	17
1.2.1.2. EBM.....	35
1.2.1.3. DED.....	37
1.2.1.4. BJ.....	39
1.2.1.5. ADAM and BMD.....	40
1.3. Conclusions.....	41
<b>Chapter 2</b> .....	43
<b>Materials and methods</b> .....	43
2.1. Materials.....	43
2.2. Mixtures preparation and characterization.....	43
2.3. Processability via LPBF machine.....	45
2.4. Samples preparation and characterization.....	45
<b>Chapter 3</b> .....	47
<b>Results and Discussions</b> .....	47
3.1. Characterization of the mixtures.....	47
3.1.1. Apparent and tapped density.....	47
3.1.2. Spreadability test.....	48
Pure Cu.....	50
Pure Cu sieved.....	51
Milled graphite.....	52
Cu – 0.25% C.....	52
Cu – 0.5% C.....	53
Cu – 0.5% milled graphite.....	53
Cu – 1.0% C.....	54

Cu – 1.5% C .....	54
Cu – 2.0% C .....	55
<b>3.2. Processability trials .....</b>	<b>55</b>
JOB 1 .....	55
JOB 2 – Cu- 2wt.%C.....	59
JOB 3- Cu-1 wt.%C.....	62
JOB 4.....	65
SSTs .....	67
Pure copper SSTs .....	70
Cu – 0.5% wt. milled C SSTs.....	77
<b>Chapter 4.....</b>	<b>84</b>
<b>Conclusions .....</b>	<b>84</b>
<b>Bibliography.....</b>	<b>86</b>
<b>Appendix .....</b>	<b>91</b>
SEM images .....	91
SEM chemical analysis .....	101
JOB 1.....	103
JOB 2.....	105
JOB 3.....	109
JOB 4.....	111

# Chapter 1

## Introduction

### 1.1. Additive Manufacturing

Additive Manufacturing (AM), as defined by ASTM International (American Society for Testing and Materials International) in the F2792-12a-Standard Terminology for AM Technologies, is “a process of joining materials to make objects from 3D model data, usually layer upon layer, as opposed to subtractive manufacturing methodologies” [2]. Therefore, the key concept in AM processes is that the final piece will be created by adding material in a layer wise manner.

This group of technologies has gained much attention in the last twenty years thanks to the innovative advantages related to its implementation. AM technologies, indeed, allow to produce high performance near net shape components starting from 3D CAD (Computer Aided Design) models. The major benefits linked to AM are unrivalled design freedom and short lead times [3], [4]: through AM, it is possible to create final parts characterized by complex shapes and hollow structures with a single-step process, ensuring a limited waste of both time and material. Finally, it is possible to customize components and even control the microstructure and the mechanical properties of the final part [5].

AM methods can be classified according to the nature and the aggregate state of the feedstock as well as to the binding mechanism between the joined layers of material [3]. The perceived standard subdivides AM techniques in seven different categories: vat photopolymerization (VPP), power bed fusion (PBF), material extrusion (ME), material jetting (MJ), binder jetting (BJ), sheet lamination (SL), and directed energy deposition (DED). A schematic of each technology is presented in Figure 1.

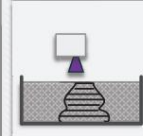
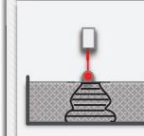
	Material Extrusion	Vat Photo-polymerization	Material Jetting	Binder Jetting	Powder Bed Fusion	Direct Energy Deposition	Sheet Lamination
Scheme							
Process	Layer by layer deposition of molten material	Selective curing of photo-curable material in a liquid container	Material deposition and subsequent curing	Selective dispense of binder for joining powder in a bed	Fusing of powder in a bed by melting the selected region	Direct fusion of the material	Bonding of individual sheets of material
Name	FDM RC MJS SFF	SLA DLP LAMP 2PP	DOD MJ NPJ	BJ	SLS SLM DMLS EBM MJF	LENS EBAM DMT	LOM UC

Figure 1 - Categorization of AM processes in the current state-of-the-art [6].

These technologies differ from each other for type of source energy used, type and state of materials, but the basic process sequence is the same for all of them [3], [7].

The first step in the 3D printing process is the design of the final component through a CAD software [8]. Once completed, the 3D model is converted in a .STL (Standard Triangle Language) file. This format allows to describe the surface of the component using triangles: each basic element is characterized by three points and a normal facet vector, which indicates the outward side in a three-dimensional Cartesian coordinate system [9]. This format allows to slice the 3D component in a series of 2D parallel layers, with the normal perpendicular to the x-y building plane, creating the manufacturing path to be followed during the process. An important parameter to take care of during this passage is the layer thickness: the non-perpendicular edges of a 3D printed component is characterized by an unavoidable stair-stepping effect which can be minimized with the use of a smaller layer thickness (Figure 2). On the other hand, by adopting a higher resolution, the manufacturing time increases: it is fundamental to find a trade-off between resolution and production time.

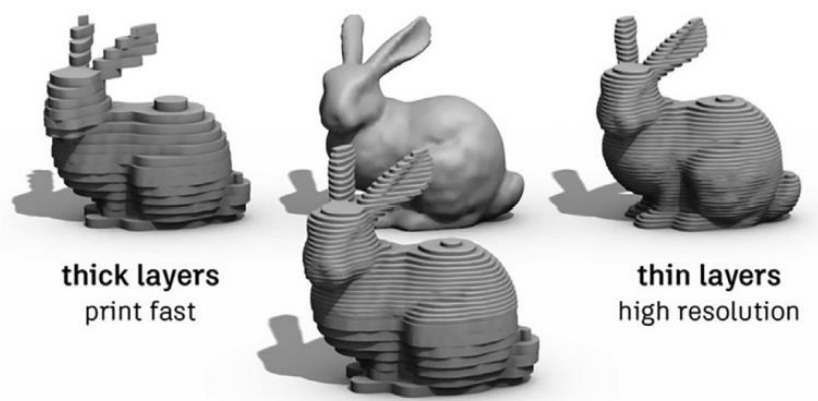


Figure 2 - Slicing of an object using different thickness [8].

The last procedure before the real building phase is to correct the eventual errors generated in the model during the conversion of format: non manifold, redundant or crossing faces, inverted normal vectors, gaps between cells. One or more .STL files can be the input of the machine, according to the quantity of different components that is going to manufacture.

Subsequently to the file transfer, the machine is ready for the setup. First the hardware setup takes place, during which the building chamber is prepared, and some process controls are set. Finally, the process control is actuated, selecting the correct process parameters and the build phase can start. This procedure is entirely controlled by the software of the machine, reducing to minimum the human intervention.

Once the last building step is completed it is possible to remove the component from the platform [10]. Depending on the process used, this can be done immediately or require some time to cool the environment. Successively it is possible to remove the excess of material, if present.

The last passage of the process sequence is the finishing of the part: eventual supports are removed and, when required, some stages to improve the surface quality and the mechanical properties of the component are performed. There are different post processes according to the technology and material choose and to the final result that is desired. Examples of post processes are heat treatments, hot isostatic pressure (HIP), polishing.

### 1.1.1. Advantages and disadvantages of AM

There are several advantages as well as disadvantages related to the implementation of additive processes, that should be carefully considered. Both advantages and disadvantages can be linked to the product and to the process.

The main product advantages that can be evidenced are exposed:

- Design freedom: undercuts and freeform geometry are allowed. There are very few geometrical limitations in the design for AM printed components. It is used to say that in AM “complexity is for free” [9]. As a matter of fact, the realization of complex geometries is not a challenge and does not influence the final cost of the component. In this optic it is interesting to print lattice structures which simultaneously ensure high mechanical properties and low density, and so lightweight structures.
- Integrated design and assemblies: assemblies are simplified thanks to the reduction of number of parts printed. The final component can present hinges and movable parts. Moreover, it is possible to tune the mechanical properties inside the part thanks to the microstructural control.
- Customization individualization: by modifying the 3D CAD model, is possible to personalize the production of specific parts according to the client needs without affecting the manufacturing cost. This is of particular interest in the biomedical field where there is the necessity to realize parts anatomically personalized.
- Material complexity: it is possible to realize component with multiple materials, which can also differ from each other in physical and thermal behavior.

For what concern the process advantages, instead, they are:

- One manufacturing step: the production process consists in one single step performed with the same machine. Even for the creation of complex shapes, there is no need for changing machine or tools. The only exception is represented by the cases in which post processing is needed.
- Flexibility and speed: AM technologies are counted as established means of accelerating the product development cycle in numerous applications [7]. It is possible to produce unlimited geometries by simply modifying the 3D CAD model according to the different requirements. The supply chain management is simplified and there is no need for storage of components.
- Low material waste: AM techniques allow to the production of near net shape components depositing materials only where is actually needed. The waste of material is limited to the surface finishing steps. For PBF processes, the powder that is not melted can be filtered and recycled for next work.
- Reduced human intervention: the manufacturing process is entirely controlled by the machine, while the operators are required mainly for the set up and part removal steps. This prevent possible human errors and reduces the risk of dangerous and harmful operations.

The field of AM is just over thirty years old [7] and, despite the significant progress achieved so far, there are still several challenges to be faced before a wide spread adoption of the technology is economically viable. The drawbacks from the point of view of the final product are:

- Material cost and variety: the materials available for AM technologies are limited and usually requires particular specifications which make them highly expensive.
- Finishing: the surface roughness of 3D printed parts is usually worse than the one obtained with traditional manufacturing. For this reason, post processing is commonly needed, increasing the production's cost and time. Moreover, it is not always feasible to finish inner surfaces of hollow components.
- Overhangs and support structures: in most AM techniques, below a certain value of angle, a downward-facing surface is no more self-supporting and support structures are required. These structures will be removed once the built of the part is completed, so they are a waste of material and generate an increase in manufacturing's cost and time as well. For this reason the component should be designed and oriented in order to reduce to minimum the need for support structures.
- Thermal residual stress: according to the AM technology adopted, the final piece can present thermal gradients and residual stresses which affect its mechanical properties.
- Anisotropy and porosities: typical defects of 3D printed components are inner porosities and anisotropy in microstructure and mechanical properties, linked to an insufficient bonding between layers during the manufacturing process [5]. These bugs negatively affect the final mechanical properties of the part.

Finally, the drawbacks linked to the machines currently available are:

- Small build rates: the build rate of AM technologies is lower if compared to the traditional manufacturing ones, due to the time required for the manufacturing process itself. This limits the opportunity for AM to reach a larger market where a batch production is required.

- Small building size: the volume available for the built of the part inside the machines is limited, hindering the possibility to create components of big dimensions.
- Elevated machinery costs: today the equipment for AM is still highly expensive, limiting the chance to be implemented in a vast scale.

### 1.1.2. Applications

Historically the principal application of AM is the prototyping process. Prototyping is the process of design and construction of objects, often in plastic material, which act as models to optimize the manufacturing process of the final product. In this way, indeed, it is possible to evaluate the part and check for errors in the manufacturing process, in connections and assemblies, in mechanical properties. In its early developments, AM was defined as Rapid Prototyping (RP), namely technologies which create prototypes starting from 3D CAD models. The main advantages resulting from the involvement of AM in the prototyping process is to reduce the design and production time and limit wastage of materials used [8].

However, in the last years, as AM methods advance, new application areas became possible [3], [7], [11]. In particular, with the improvement of technologies and the development of new materials for AM, these techniques are adopted also for the fabrication of final products.

Today AM is economically favored in small batch production. As a matter of fact, the cost associated with manufacturing can be divided in fixed costs, not dependent from the volume of production, and variable costs, which are directly dependent from the number of parts produced [12]. In general, the fixed costs of AM are about 1/10 of the conventional means. On the other hand, the recurring costs are way higher. As is possible to see from Figure 3, the total costs of manufacturing is a function of the number of parts and the slope of AM costs is deeper than the conventional one's. This means that over the break-even point, where the costs are equivalent, AM is no longer economically competitive.

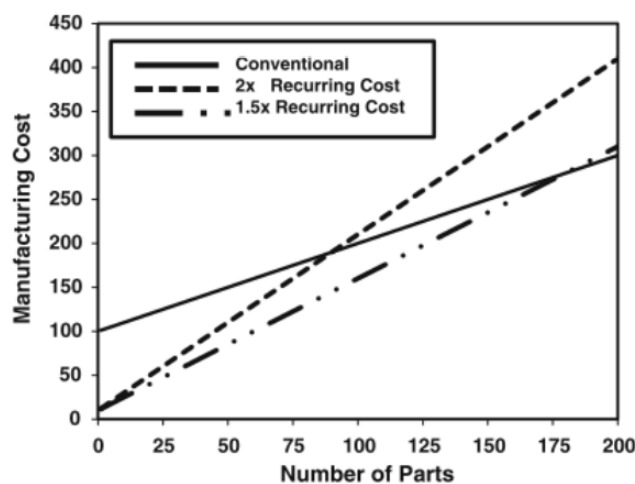


Figure 3 – Manufacturing cost versus number of parts manufactured through AM [12]

Hence, AM is expanding over those industrial sectors characterized by high production costs, low production volumes and difficulties in finding raw materials at low prices. The main fields are:

➤ **Aerospace/Energy:** AM is particularly suitable for the production of aerospace components which often complex geometries and are made usually from advanced materials, such as titanium alloys, nickel superalloys, special steels or ultrahigh-temperature ceramics, which are difficult to traditional manufacture. Moreover, the production is limited to a maximum of several thousand parts per year [13]. Examples of these components are combustors, nozzles and blades for turbines. Thanks to the topology optimization and to the adoption of high-performance materials, it is possible to drastically reduce the part's weight. Another interesting advantage which comes from the implementation of AM technology is the opportunity to repair damaged expensive components.

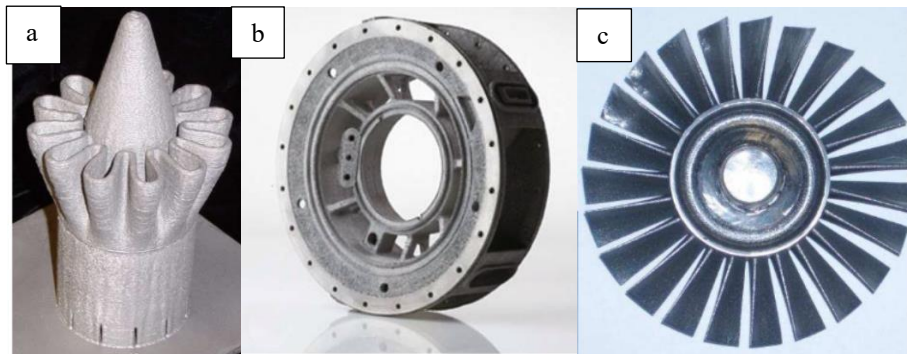


Figure 4 - Examples of AM aerospace components. a) Mixing nozzle for gas turbine exhaust produced by LENS [13]; b) Compressor support case for gas turbine engine produced by EBM [13]; c) Turbine wheel printed in EOS Nickel Alloy IN718 [9].

➤ **Automotive:** similarly to the aerospace field, also automotive can benefit from the use of lightweight 3D printed components. This is particularly true for motorsports vehicles, unlike passenger cars. In motor race cars suspensions, uprights, exhaust manifolds, engine block, drive shafts, gear box and water pumps have been redesigned through topological optimization, increasing their mechanical characteristic and reducing their weight [13].

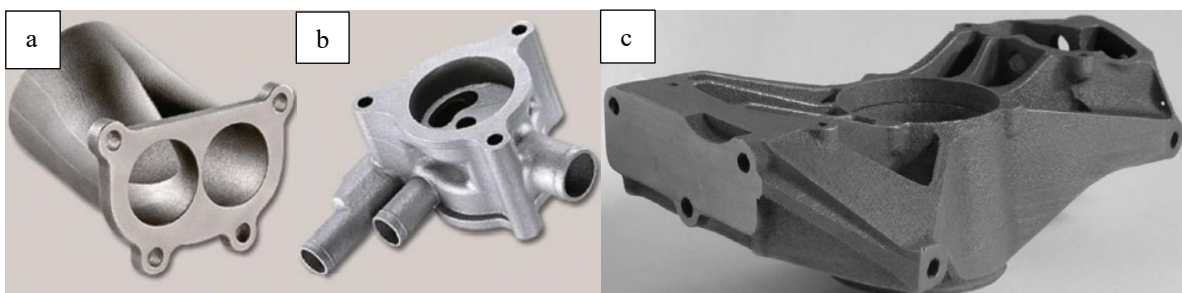


Figure 5 - Examples of AM automotive components. a) Exhaust manifold produced by SLM [13]; b) Oil pump housing produced by SLM [13]; c) Race car upright in Ti6Al4V printed with Arcam EBM [14].

➤ **Biomedical:** AM technologies are particularly suitable for the production of orthopedic and dental implants. The prosthesis can be easily customized for the patient. It is also possible to create particular surface textures in order to make the implant integrates better with the surrounding tissues. Finally, continuous technical development and research in material engineering provides opportunity to utilize improved biomaterials in medical field [15].

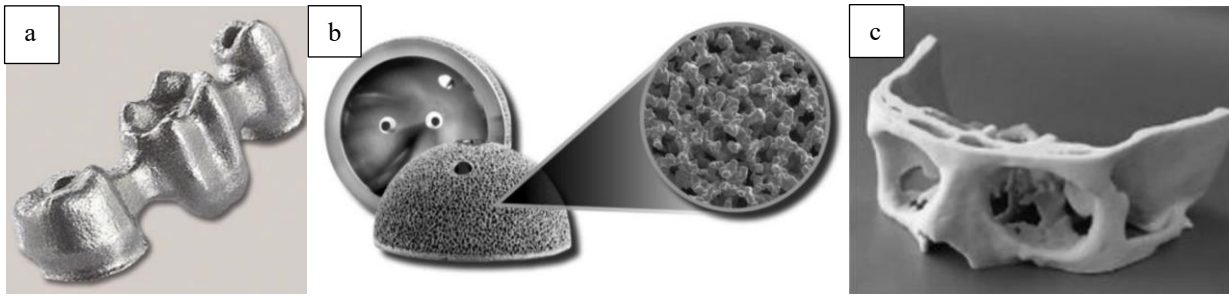


Figure 6 – Examples of AM biomedical components. a) 3-unit dental bridge produced through SLM [13]; b) Ti6Al4V acetabular cup with surface design improved for osseointegration [16]; c) Cranial segment manufactured in FMD technique [15].

➤ **Art, architecture and fashion industry:** AM is also used for the production of prototypes of elaborated architectural models, but also for highly aesthetic components such as shoes, clothing, jewelry and furnishing. Moreover, with some technologies like Polyjet, the products can be directly printed in full colors.



Figure 7 - Examples of AM fashion components. a) Silver ring [17]; b) Polyjet printed butterfly-design nails [18]; c) Clocks produced through stereolithography [9].

➤ **Electronics:** examples of electronic devices that can be 3D printed are resistors, capacitors, inductors, antennas, transistors, LEDs and batteries. In this field new materials suitable for AM are being developed like electronically-conductive carbon black and graphene-based filaments [19]. In this optic, the most interesting goal is to envision and print devices with embedded miniaturized electronics [20].



Figure 8 - Examples of AM electronic components. a) Graphite composite bipolar plates for PEM fuel cell fabricated by SLS [13]; b) 3D printed sample of an x-axis expansion testbed [19]; c) A touch pad 3D printed using conductive paint [20].

### 1.1.3. Metal AM

Thanks to the new developments in 3D printing technology, and so to the improvements achieved in equipment and powders, Metal additive manufacturing (MAM) is one of the most attractive research field today [6]. Above all, the most important AM technologies that are implemented to print metals are PBF techniques. The energy source used can be laser beam or electron beam. For what concerns the materials, instead, the metal can be manufactured starting from powders or wires. In particular in this thesis Laser Powder Bed Fusion (LPBF), also referred as Selective Laser Melting (SLM), is going to be adopted. With this technology metallic materials in the form of powder are selectively melted by a laser beam.

#### 1.1.3.1. Powder for PBF

In PBF the heat source is applied to particles contained within a powder bed. The resulting component consists of many thousands of melt powder layers. The properties of the final component depend on the uniformity of these layers, that depends on the properties of the powder used. For this reason, the choice of the correct powder is not trivial and is crucial for the success of the manufacturing process [21]–[23]. In particular, the material's characteristics that have the major influence on the PBF process are the particle shape, particle size (PS), particle size distribution (PSD), the resulting powder bed density (PBD), but also the chemical composition, the melting temperature and the laser absorbance [22].

For what concerns the PSD of the mixture, it should be wide enough to ensure that the finer particles can fill the voids between larger ones. In this way is possible to obtain a higher density of the powder layer, and so, a higher density of the printed component [24]. On the other hand, the presence of a high amount of extremely fine particles has a negative effect on the flowability: the smaller elements can easily form agglomerates around the bigger particles and induce higher inter-particle friction, creating an inhomogeneity in the spread layer [21].

PBD, indeed, has a significant impact on the manufacturing step: a highly dense powder bed enables the minimization of by-products porosity and improves the powder absorptivity. Further, a uniform powder bed is a key factor to ensure homogeneous interactions with the laser beam, avoiding dynamic variation which would lead to processing issues [21].

Regarding the shape, spherical, regular and equiaxed particles show a better rheological behavior and a more efficient particle packing. While, the use of irregular shape powder led to the creation of higher porosities. Hence, the type of atomizing procedure must be carefully selected. Gas atomization is one of the most used technology, which, as opposed to mechanical methods, ensure the realization of highly spherical particles. It is adopted for the atomization of metallic powder such as iron, aluminum, copper, cobalt, titanium, steel and other alloys. The atomizing gas can be air, nitrogen, argon or helium: the latter are inert gas usually adopted for the atomization of more reactive materials. The resulting particles have dimensions ranging from 50 to 300  $\mu\text{m}$ . Although the particles are generally spherical and smooth, some defects can occur. A common flaw is the presence of satellites, namely smaller particles that can remain stacked to the surface of the bigger one, inducing a deviation from their perfect spherical shape. Moreover, another defect promoted by this method of atomization is the creation of porosities inside the particles, where the atomizing gas can remain entrapped.

Finally, another important aspect to be considered in the selection of the powder for PBF process is its chemical composition. In many cases the powder is not completely pure, but there is a considerable content of impurities, such as oxide layers or other gases absorbed inside the porosities of the particles themselves. The presence of external elements can hinder the possibility to print high quality components and can reduce the mechanical properties.

In conclusion, highly spherical powders with a limited number of fine particles and defects are a necessary condition to the realization of a highly dense powder bed and so, of printed parts with superior densities, surface finish, dimensional accuracy and mechanical characteristics.

## 1.2. On the processability of Copper parts via AM; Potentials, challenges and feasible solutions

Above all metals, copper is the most suitable for the production of heat exchanger components, thanks to its high electrical and thermal conductivity. The heat transfer capability of a heat exchanger can be further improved with the use of Additive Manufacturing (AM) techniques, which allow to produce intricated channels with a maximized surface to volume ratio. Unluckily, mainly due to the high thermal conductivity and reflectivity of copper, its processability through AM processes is particularly challenging. Thus, over the last decade, many studies have been conducted to investigate the problems faced and to present new possible solutions to be adopted. This paper aims to contribute to this growing area of research by exploring the actual state of art of the 3D printing of copper parts. This study traces the developments achieved so far and the obstacles still present in the production of high-quality copper components through the most important AM techniques.

Copper (Cu) as a malleable and ductile metal presents a good corrosion resistance and low chemical reactivity [25]. In humid air it forms a greenish surface film, which protects the metal from further attacks. In addition, copper is characterized by extraordinary machinability and formability as well as high electrical ( $60 \times 10^6$  S/m, which is equal to 100% International Annealed Copper Standard (IACS)) and thermal conductivity (400 W/mK) [26]. Owing to these interesting features, copper attracts many attentions in different applications like microelectronics, roofs and plumbing implants, radiators, charge air coolers and heat exchangers [27]. This wide range of characteristics and applications make copper a promising material in various industrial sectors like electro packaging, automotive and construction industries [28]. On the other hand, copper is also frequently used as a base material for different alloys such as brass and bronze, that, in addition to copper, consist of zinc and tin, respectively [29].

Owing the high malleability and formability, copper is commonly processed via Powder Metallurgy (PM) or conventional manufacturing processes (e.g. forging, machining, extrusion and casting) [30]. However, these manufacturing techniques suffer from a variety of limitations mainly related to the difficulties in the production of optimized finned heat exchangers and heat sinks [31]: traditional manufacturing processes are characterized by high production costs, complex and time-consuming post-processing steps. The design of heat exchange components aim to minimize their size while using optimized thin fins to increase the surface area and the heat transfer rate between the heat exchanger surface and the surroundings [31]. In this context, Additive Manufacturing (AM) processes result to be attractive thanks to the possibility to produce topologically optimized geometries layer by layer [11], reducing the period of manufacturing and tooling requirements. Additionally, from the point of view of the production of heat exchanger and heat sink, the possibility to obtain monolithically components without joints or any additional coupling operations allows for a better resistance to the liquid pressure during operation and avoid leakages [31]. Furthermore, AM processes provide an efficient solution to produce low volume customized parts, easy on-demand manufacturing, the integration of multi functions, assemblies and high component. AM processes are also characterized by small environmental footprint, since it is possible to use only the material needed, limiting wastes [32].

Today, a large variety of AM techniques are available on the market for producing metal components. The most common technologies are based on powder feed. Laser Powder Bed Fusion (L-PBF) and Electron Beam Melting (EBM) are powder bed fusion based AM processes, in which a laser or an electron beam, respectively, is used to melt selectively the powder particles [33][16]. Powder Bed Fusion (PBF) is an advanced AM technology that has matured over an extended period of research and industrial development. [34] PBF techniques share the basic principles of all AM techniques as well as common advantages such as cost-effective customization and reduced assembly [35]. Today this technology is particularly used for the production of high-value products that are not technically feasible with traditionally manufacturing processes. In particular, commercial opportunities exist for the manufacture of highly complex geometry at small production volume; for example, as required for medical and aerospace applications.

Another interesting technique adopted is Binder Jetting (BJ) in which no heat source is used to fuse the powder, but a binder is selectively distributed above the powder bed [36]. In this way material's reflectivity, melting point and thermal conductivity do not affect the process. Once the green part is completed, it undergoes a sintering phase, during which the binder is removed, and the component's strength and density are improved.

Direct Energy Deposition (DED) is an AM process, in which a powder flow is melted using a laser and fed into the process through a nozzle into the melt pool that is already generated by a heat source. In this process, the melting and deposition of material also follow the 3D model that is loaded inside the machine [37].

Atomic Diffusion Additive Manufacturing (ADAM) and Bound Metal Deposition (BMD) are relatively new AM techniques for metal components. Both processes are based on the combination of Fused Deposition Modelling (FDM) process for polymers and Metal Injection Molding (MIM), a traditional process to obtain a close full density metal part with high complexity. In this case, the feedstock material is a filament which is made of metal powders enclosed in a thermoplastic polymer that works as a binder for the metallic particles. The material is added layer-wise manufacturing through a heated nozzle. After the production the as-built part (green part), is washed to remove the binder, and then is sintered in a furnace that allows the densification of the material.

Despite the clear advantages presented by the adoption of AM technologies, it is well documented that the processability of copper and copper alloys via metal AM processes faces with several challenges [38]. The high electrical and thermal conductivities of copper and its alloys increase the heat transfer rate from the melt pool to the surrounding area and generate high thermal gradients and detrimental consequences for the process and the part quality [39]. In addition to that, for laser based processes, the low laser absorption rate in the near infrared region is another greatest issue [30]. Both the rapid heat transfer and the high reflectivity hinder the absorption of the laser power, resulting in high porosity and poor mechanical, thermal and electrical properties. The ductile nature of copper has a negative effect on the post powder removal and recovery [38], [40], probably because the built copper piece can be easily deformed during this stage. The high sensitivity of copper to oxidation makes the powder handling difficult [38]: it requires inert atmosphere during

the process and special storages. The risk connected to the presence of copper oxides is the formation of gas bubbles inside the matrix of the final component, which reduces the density and electrical conductivity.

Nevertheless, the opportunity of obtaining high-performance components layer by layer approach is boosting a wide scientific research with the aim to develop or enhance the feasibility of copper and its alloys by AM processes [39], [40]. In this context, a large number of works have been published, in particular during these last years. The adopted solutions can be grouped into technological based or material based. In this paper, the term technological will be used in its broadest sense to refer to all the modification and optimization of the design machine or process parameters. Material-based solutions, instead, concern the addition of other elements to the pure copper and/or the possibility to chemically modify the surface of copper powder.

Whilst several researches have been carried out on the challenges and possible solutions of the processability of pure copper through AM techniques, there is still very few review articles that are able to give a global overview of the thematic. The only review paper that is possible to find at the moment in literature is the one presented by Tran et al. [40], but there are some substantial differences with the present article. First of all, it is a review of the main 3D printing methods for fabricating highly pure copper, including also Ultrasonic Additive Manufacturing (UAM), which is not considered in our study. This technique allows to build components without the help of any heat source: metallic foils are bonded with the application of ultrasonic waves and mechanical pressure. Another technique that is presented by Tran et al. is indirect SLM, a method that is no longer used for metallic materials. ADAM and BMD instead are not treated in their review paper. Moreover, Tran et al., with their article, demonstrated the potential applications of 3D printed copper, which is not object of this discussion.

The objective of this article is to review the literature available and provide a thematic overview of the current state of art on the fabrication of copper and its alloys through AM processes. The target of this work is also to point out the importance, the challenges and the opportunities when the potentialities of AM processes are integrated with the unique characteristics of copper. First of all, the main challenges in processing of copper by AM processes are discussed in detail. Then, the current solutions to improve the processability of copper via AM processes are presented, including their relative advantages and limitations. In conclusion, this review highlighting the best practices that may be considered for future works to accelerate the developing of copper processed by AM.

### 1.2.1. Additive Manufacturing of Copper

By the progress of technology, production of functional circuits, electronics and energized devices of high performance, and excellent electrical, thermal and mechanical characteristics is a crucial need. This vital need motivates the R&D focus toward the integration of advanced manufacturing methods such as AM with potential materials that can full fill the aforementioned criteria. For this reason, AM of copper which is a promising material for electronics and electronic cooling, could attract lots of attentions [41]. However, it is reported that owing to some inherent characteristics of copper such as high laser reflectivity, high thermal conductivity and high sensitivity to oxidation

make the processing of copper through the AM processes, in particular the laser-based ones, very challenging.

In literature it is reported that the more suitable technologies that can be used to process pure copper and its alloys are LPBF, EBM, DED, BJ and ADAM. Each technique presents different advantages and disadvantages, different challenges to face and so, different solutions that can be adopted. The studies conducted till today, in order to enhance the processability of copper through AM techniques, have proposed different possible solutions, that can be subdivided in two main groups: technological based solutions, in which the machine components and/or the processing parameters are adjusted, and material based solutions, where the copper powder is modified by the addition of other elements or surface treatments. In the next paragraphs, the current literature is presented, subdivided according to the different technology used to process pure copper or its alloys.

### 1.2.1.1. LPBF

Laser Powder Bed Fusion, also called Selective Laser Melting (SLM), is a powder-based process particularly suitable to print metallic component [11]. The powder is spread above the plane with the use of a recoater blade, ensuring a uniform distribution. The laser with a wavelength in the near infra-red region ( $\lambda \sim 1\mu\text{m}$ ), selectively fuses the part in the XY plane. Once a layer is completed, the platform is lowered, and the process is repeated till the completion of the part. The main parameters that characterize the process are laser power ( $P$ ), scanning speed ( $v$ ), layer thickness ( $s$ ) and hatching distance ( $h$ ) (Figure 9). In order to ensure an inert atmosphere, the chamber is filled with argon or nitrogen: in this way the risk of oxidation is reduced.

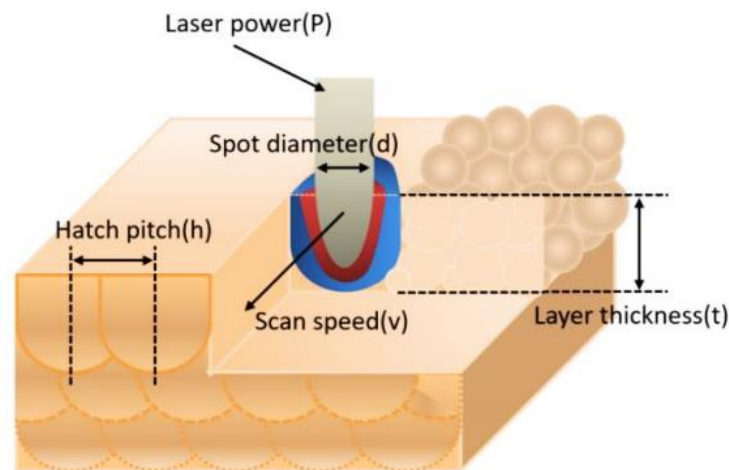


Figure 9 – Schematic of the LPBF process showing its main process parameters [42]

In general, metallic materials suitable for the LPBF process have to meet three basic requirements; I) low thermal conductivity, II) high laser absorption, and III) contain high boiling point elements [43]. It is very interesting to highlight that the lack of the first criteria results in difficulty in creating a stable melt pool. More specifically, due to the high thermal conductivity of copper, the heat is rapidly dissipated away from the melt pool area, resulting in high local thermal gradients. As a

consequence, this high local thermal gradient results in the formation of some defects such as layer curling and delamination during the process that finally can lead to part failure.

The second challenge in the processability of copper is associated to the lack of the second criteria for the processability of materials through LPBF process (low laser absorption). In fact, as can be seen in Figure 10 (a), in the near-infrared region the mean absorptance rate of copper is lower than 6% at room temperature, which is much lower than the other metallic alloys. However, as it is shown in Figure 10 (b), this quantity for copper increases a bit near its melting temperature [44], but still restricted at a very low value. It is also reported that for the laser beams with higher wavelength, the mean absorptance is even lower, up to 2.6% at 10 $\mu$ m [30]. This implies that the one of the most feasible solutions to increase the laser absorptance of copper is using lasers with wavelengths shorter than 1  $\mu$ m which would be green or blue laser.

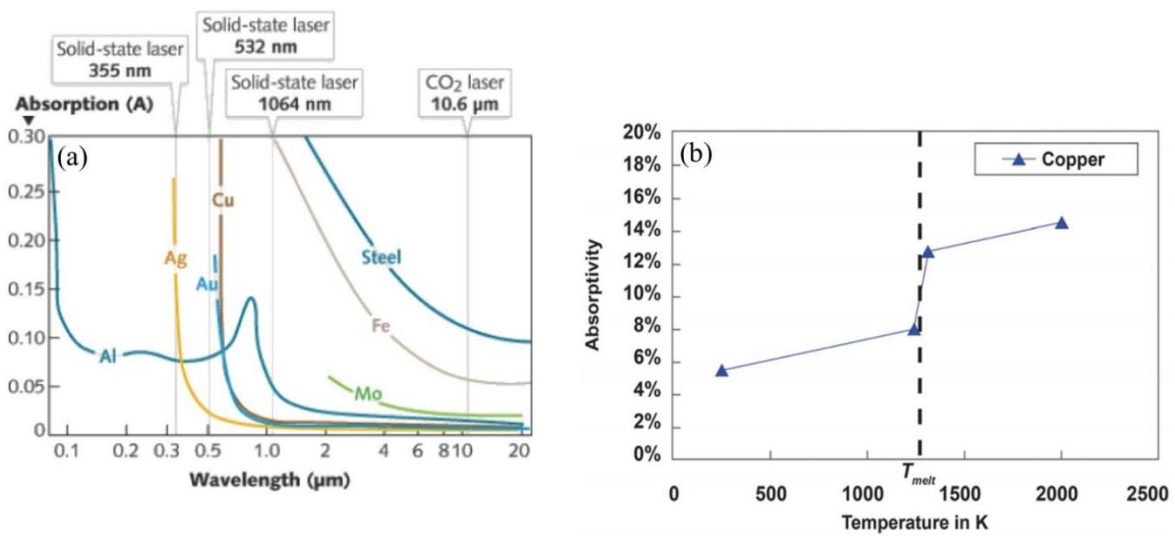


Figure 10 - Laser absorption of copper as a function of (a) wavelength [45], (b) temperature [1].

Both high thermal conductivity and low laser absorption of copper reduce the amount of energy available to melt the material. Therefore, the powder would not be able to wet the substrate and tends to agglomerate in the form of balls or tubes with a diameter larger than the powder diameter along the laser track [46]. As a matter of fact, this phenomenon, which is called balling effect, generates a high level of porosity in the part (Figure 11) that as a consequence, deteriorates its mechanical and electrical properties [30]. Hence, a higher volumetric energy density (VED) should be provided to facilitate the formation of a stable melt pool. However, it should be pointed out, owing to the high reflectivity of copper, a fraction of this VED is back reflected. This back reflection of laser energy into the source can cause all types of havoc. One of the main issues of the back reflection is damaging the optical coating on the laser mirror as shown in Figure 12 [47].

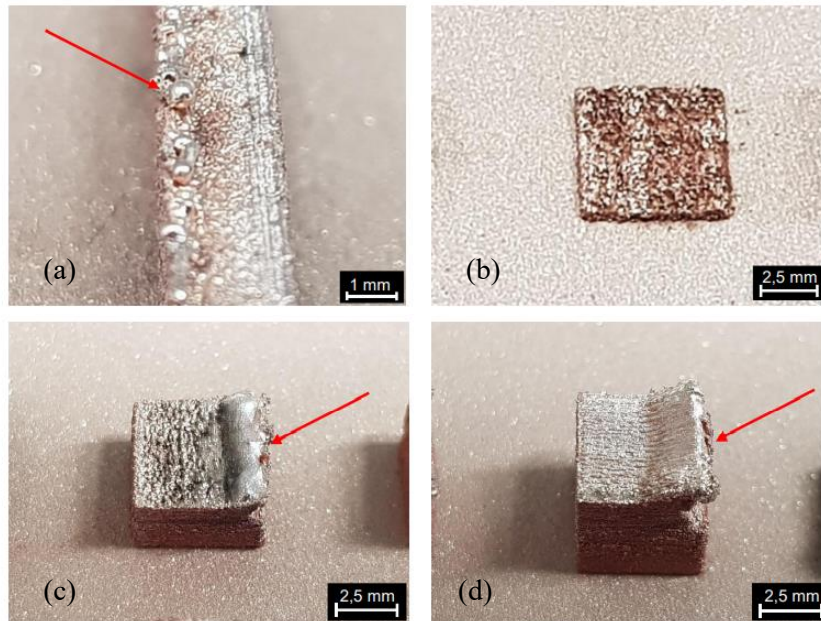


Figure 11 - Common defects in LPBF pure Cu parts: (a) balling effect and (b) micro balling effect, due to insufficient wetting behavior between melt pool and solidified layer; (c) elevated edge, when a big melt pool is not able to completely wet the underlying layer. This effect adds up over several layers and appears as an elevated edge; (d) delamination of a layer, generally caused by thermal gradients [48].

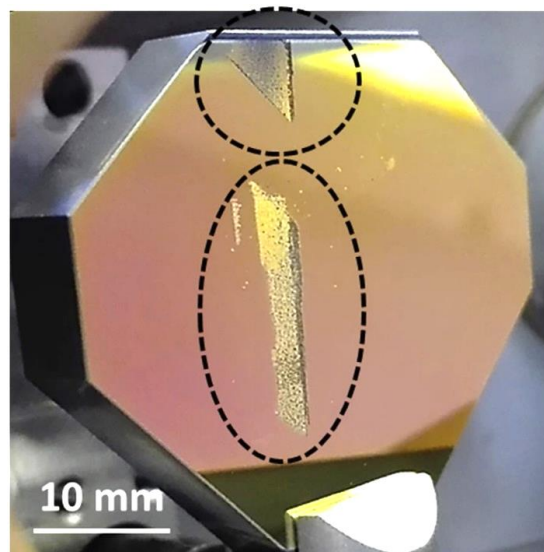


Figure 12 - An example of a damage to the optical mirror as a consequence of being exposed to laser back reflection for 12 h [47]

Another challenge is related to high sensitivity of copper to oxidation (Figure 13). In fact, it is well documented that copper oxides will tend to decompose during the LPBF process in copper and oxygen gas, which remains entrapped inside the matrix and leave porosity [38] Therefore, the resulting component is characterized by lower density and electrical conductivity with respect to defect free parts. Hence, copper powder requires special handling and storage before and after the fabrication of the components, and an inert atmosphere during the LPBF process.

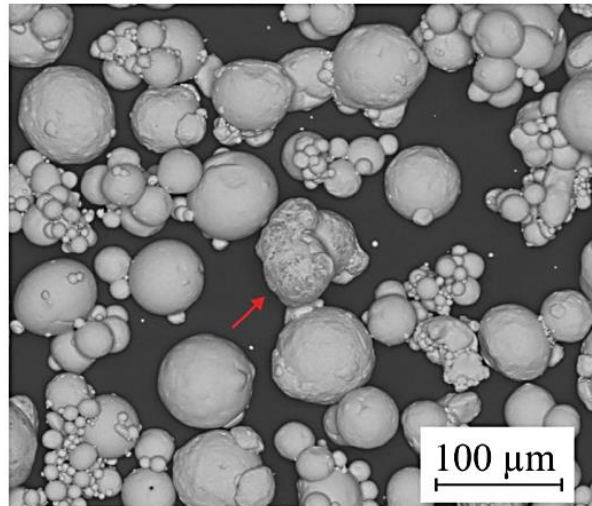


Figure 13 - Copper oxide indicated by the red arrow [28].

Another secondary problem is related to the tendency of copper particles to agglomerate, reducing flowability and obstructing powder deposition [40]. Finally, the high ductility of copper hinders post-build powder removal and recovery of the printed parts [38].

As already stated, there are several solutions proposed so far to improve the processability of copper, and they can be subdivided in technological based and material-based solutions. As one of the main technological-based solutions, process parameter optimization is considered and employed in order to obtain the fully dense copper components. In this optimization process, the main parameters that are considered as the effective ones are laser power, laser scanning speed, hatching space, laser beam diameter and layer thickness. By adjusting and controlling these parameters it is possible to improve the quality of the final component significantly by reaching the right quantity of energy density. In general, as mentioned earlier, copper requires a high VED, which is calculated as  $\frac{P}{vhs} \left( \frac{J}{mm^3} \right)$  therefore a high laser power, low scanning speed, low layer thickness and low hatching distance can fulfill this requirement. However, there should be a threshold for the high VED in order to reduce the risk of back reflection and of severe convective motion and vaporization of the molten pool [49].

It has been experimentally revealed that the values of laser power lower than that of the standard one (around 200 – 400 W), is not sufficient to correctly process copper powder, resulting in a very porous structure [50]. For instance, Benedetti et al. [32], processed pure copper using a 94 W laser source. In fact, in their work, at a constant laser power of 94 W, different layer thicknesses (0.075 to 0.1 mm) and scanning speeds (20 to 200 mm/s) were studied as well as the effect of remelting. This range of parameters from the VED point of view lies in the range of 45 to 290 J/mm<sup>3</sup>. They found that this range of VED is not sufficient to completely melt and consolidate the copper powder. As a matter of fact, their microstructural analysis proved that over the wide range of VED a very porous structure full of lack of fusion were achieved (Figure 14). In addition, the role of remelting on the consolidation was found to be positive, when applied ones, whereas in the case of using twice it would be deteriorated.

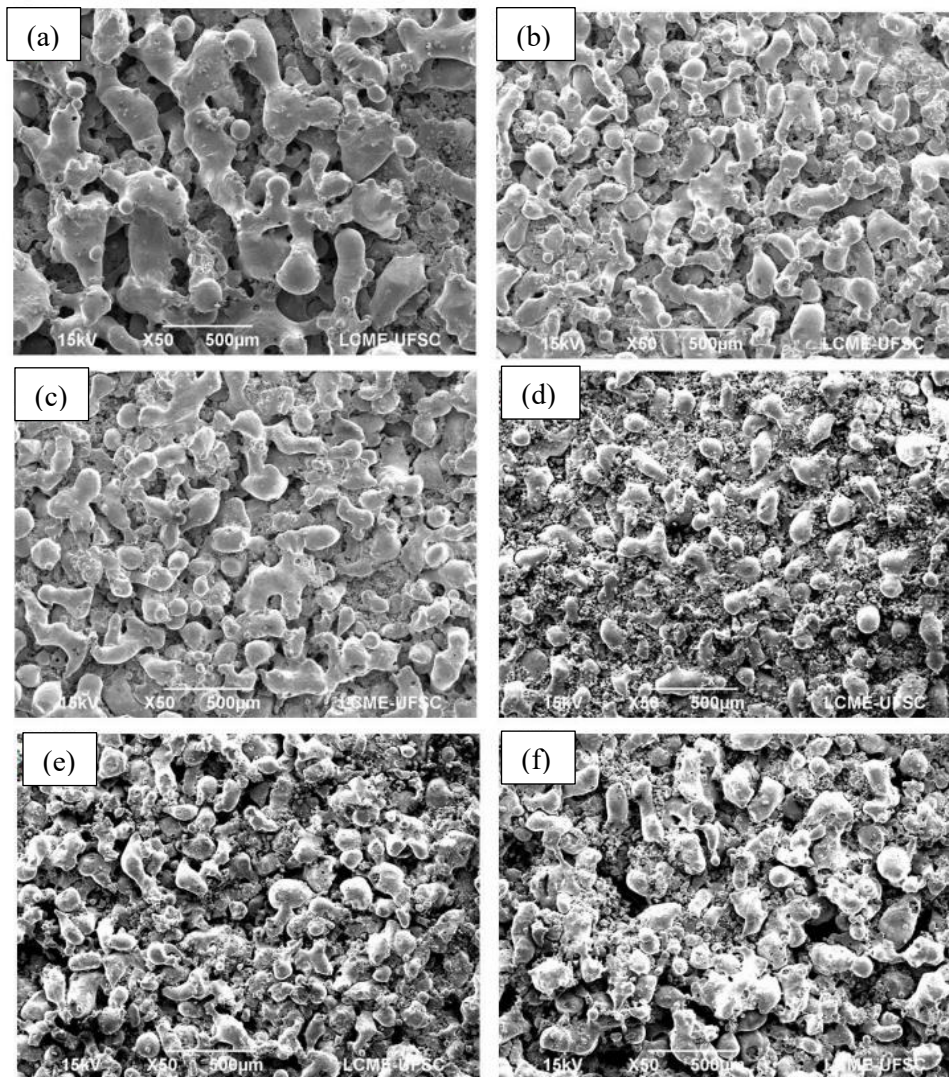


Figure 14 - SEM analysis highlighting elevated porosities – (a) VED 289.23 J/mm<sup>3</sup>, highest value, (b) VED 141.00 J/mm<sup>3</sup>, (c) VED 113.94 J/mm<sup>3</sup>, (d) VED 125.34 J/mm<sup>3</sup>, (e) VED 192.82 J/mm<sup>3</sup>, (f) VED 47.00 J/mm<sup>3</sup>, minimum value [32].

In another work, Jieren et al. [51] produced pure copper thin walls with a YAG fiber laser operating at 1,060 nm in the NIR region, with a power of 190W and a scanning speed of 500 mm/s. For this reason, at first, in order to narrow down the window of parameters, a single scan track experiments using a different combination of laser power (130-190 W) and scan speed (400 to 700 mm/s) was performed on a steel platform. Their outcomes exhibit the effect of the Linear Energy Density (LED) on the track continuity is such a way that, as can be seen in Figure 15, at low LED (less than 260 J/m), the single track is discontinuous and irregular. The method of single scan experiment also in the case of copper, was found to be very helpful in the optimization of process parameters. Nevertheless, even with the optimized set of parameters achieved from the single scan track analysis, the bulk components showed a maximum relative density of 82%. It was found that to instability of the molten pool induced by Marangoni convection, in addition to the porosities, cracks and cavitation were observed in the microstructures (Figure 16).

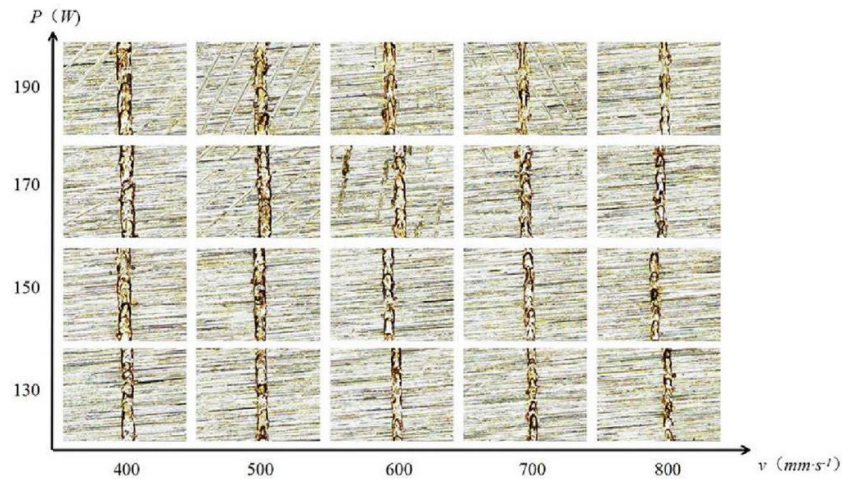


Figure 15 - Morphology of a single track with a different combination of process parameters [51].

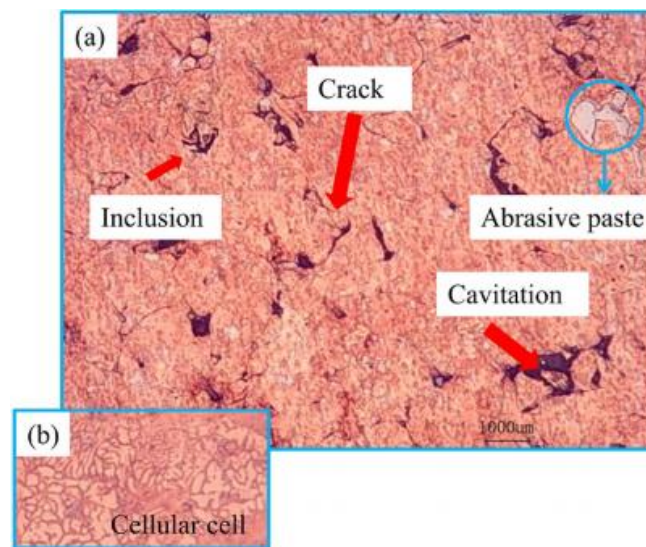


Figure 16 - Metallographic microstructure of pure Cu with optimized process parameters [51].

Silbernagel et al. [52] also found as the optimal set of variables with a laser power of 200 W, a layer thickness of 45  $\mu\text{m}$ , the laser spot size of 35  $\mu\text{m}$  and a scan speed of 300 mm/s. Even in this case, the highest relative density was about 85.8% while cracks and cavitation were observed as well. Moreover, the produced copper part presented an electrical resistivity that was almost double of the one of commercially pure one. They concluded that a 200 W, 1070 nm wavelength laser is not suitable to fully fuse a new layer of powder with the solid layer below, even with small spot size. As a matter of fact, the copper powder absorbs more energy and retains more heat with respect to the solid layer. Thus, it is not possible to re-melt the previous layer and obtain sufficient consolidation.

It is well documented that, pure copper components fabricated through the LPBF process can show low values of porosity if processed with very high laser power [53]. An example is reported by two studies, from Imai and Ikeshoji et al. [54] [55], which detected as an optimum set of processing parameter a laser power of 800 W coupled with a scan speed of 300 mm/s (Figure 17) and hatch distance of 0.01 mm. The influence of the hatch distance was evaluated through the Finite Element Method (FEM) analysis, showing that for a narrower hatch space, the melt pool becomes unstable,



to the consequent lower thermal gradient as well as more homogeneous heat distribution, the action of surface tension forces is reduced and thus the formation of the balling instability decreases. Compared to the mono-scan strategy, an improvement of the apparent density was achieved through the energy redistribution strategies, from 98.7% to 99.1%.

Since the building platform exerts a crucial influence in maintaining the powder bed temperature and hence the process stability [44], three alternative solutions for the building platform materials have been investigated by Colopi et al.. In their work, in order to highlight the impact of the building platform materials on the densification of the built component a 12-mm-thick AISI 316L platform, a 5-mm C110 (Oxygen-free copper) platform and a hybrid solution constituted by a 1-mm-thick C110 mask overlapped to an AISI 316L platform were used (Figure 18).

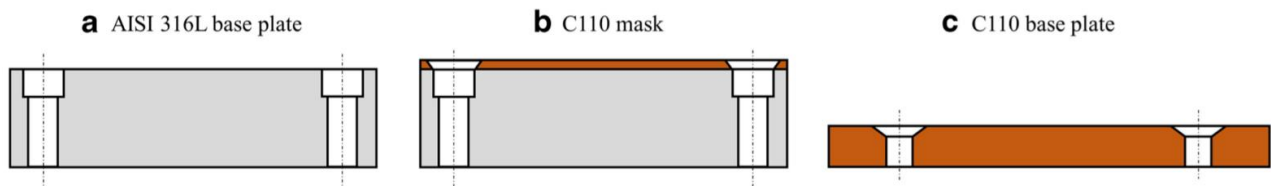


Figure 18 - Schematic representation of the (a) AISI 316L, (b) C110 mask, (c) C110 building platforms [1].

Their study proved that the material of the building platform and its thermal conductivity have a marked influence on the process stability. In fact, it is revealed that owing to the high thermal conductivity of the copper platform, the melt pool on this plate would not be stable and constant, whereas the use of a stainless-steel, instead, as a substrate for pure copper would be beneficial mainly because of its lower thermal conductivity that assures heat accumulation at the bottom of the sample. As is possible to deduce from Figure 19, for some combinations of process parameters it was not possible to fully process samples on C110 base plate and mask. Moreover, the apparent density of the specimens shows a very dispersed behavior in the case of copper base plate and mask, indicating the difficulty in maintaining a stable melt pool. With a AISI 316L base plate, instead, the apparent density showed an interesting stabilization area where it reaches the highest values.

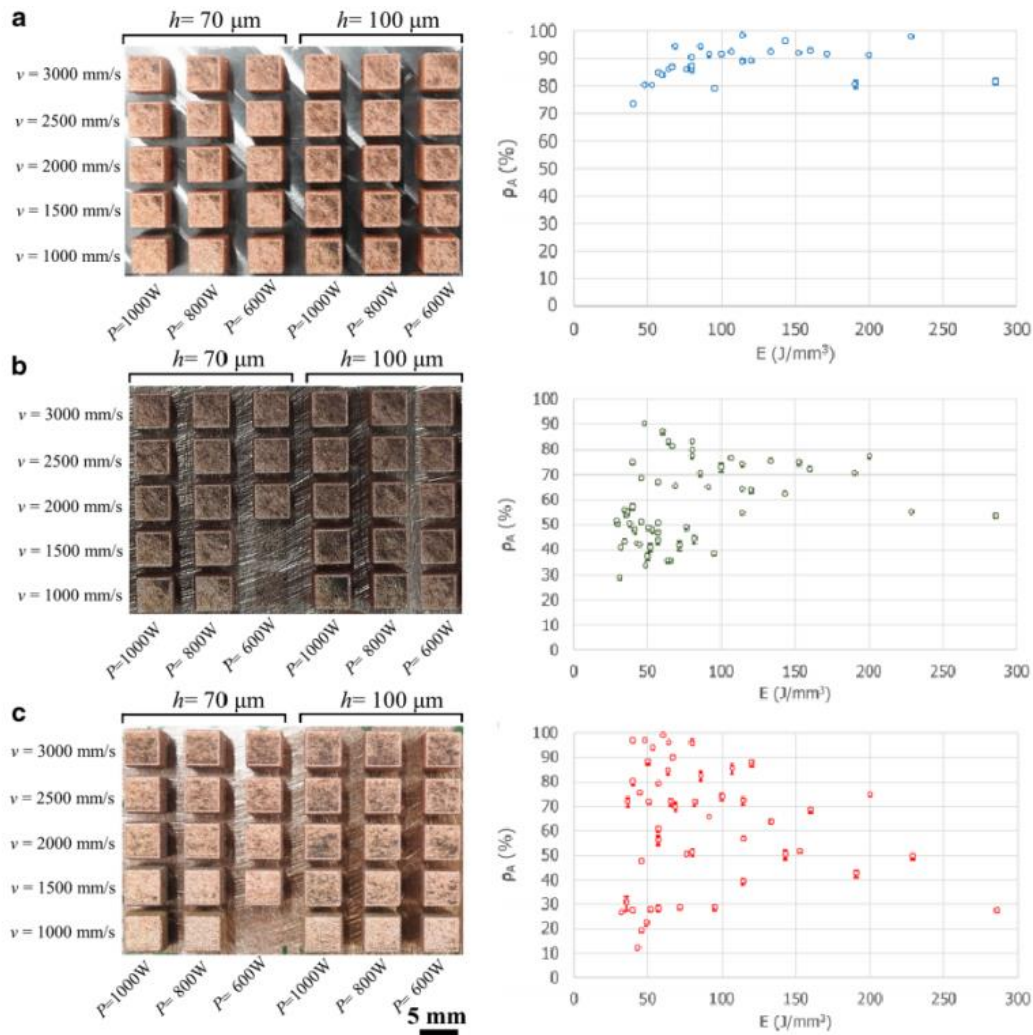


Figure 19 - Left: an overview of cubic samples built on (a) AISI 316L base plate, (b) 5-mm-thick C110 base plate and (c) 1-mm-thick C110 mask. Right: mean apparent density of pure Cu deposited on AISI 316L, C110 base plate and C110 mask [1].

In another work, Guan et al., studied the effect of aluminum platform on the process stability and then compared with the influence of the steel one [51]. In fact, in their work the adhesion of the copper specimens with both platforms was studied and compared (Using the same process parameters: 190 W as laser power and 500 mm/s as laser scan speed). They revealed that in the case of Al platform because of its high thermal conductivity a rapid heat dissipation from the sample to the dense platform was facilitated and as a consequence the bonding between the platform and Specimen was poor and warpage and distortion were taken place at the bottom of copper samples (Figure 20 (a)). Therefore, this led to an unstable melt pool and non-uniform temperature distribution and results in formation of thermal stresses that induces deformations. Instead, in the case of steel platform the heat accumulation that can take place as a result of its low thermal conductivity facilitate the formation of a metallurgical bonding without warpage and distortion and consequently help the process to be more stable (Figure 20(b)).

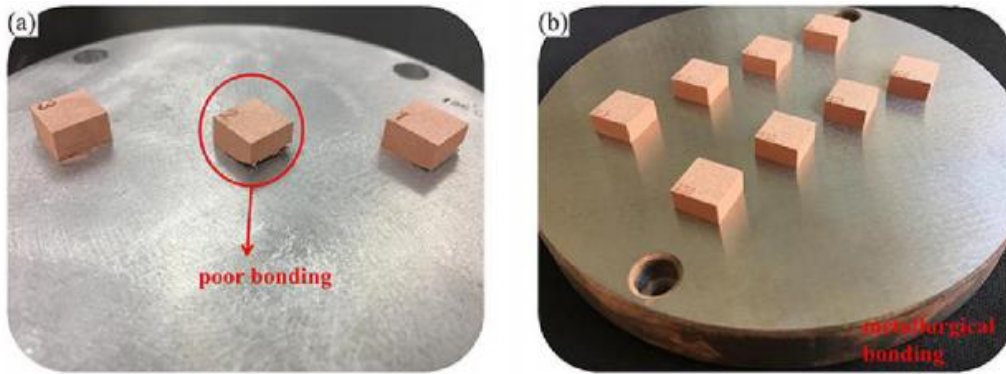


Figure 20 - LPBF copper samples produced on (a) Aluminum, (b) steel platform [51].

Lykov et al. [50], studied the processability of copper using a 200 W CO<sub>2</sub> laser with a higher wavelength with respect to the Nd:YAG one. In their work, a small laser beam diameter of 35  $\mu\text{m}$  was used in order to compensate the low laser power. However, even in this case in spite of using a low laser spot size, higher laser wavelength, layer thickness of 50  $\mu\text{m}$  and hatching distance of 0.012 mm, 88.1% was the highest relative density. Nevertheless, recently, Stoll et al. [48], succeeded to produce a fully dense copper component (99.82%) using a laser wavelength of 1070 nm thanks to the definition of an optimum set of parameters; laser power of 400 W, scan speed of 600 mm/s and a laser beam diameter of 35  $\mu\text{m}$ . So far, this density is the highest value that have been achieved. Thanks to this high level of densification (Figure 21), the resulting specimen had an electrical conductivity of 56.88 MS/m, which was assessed within a four-wire-conductivity test.

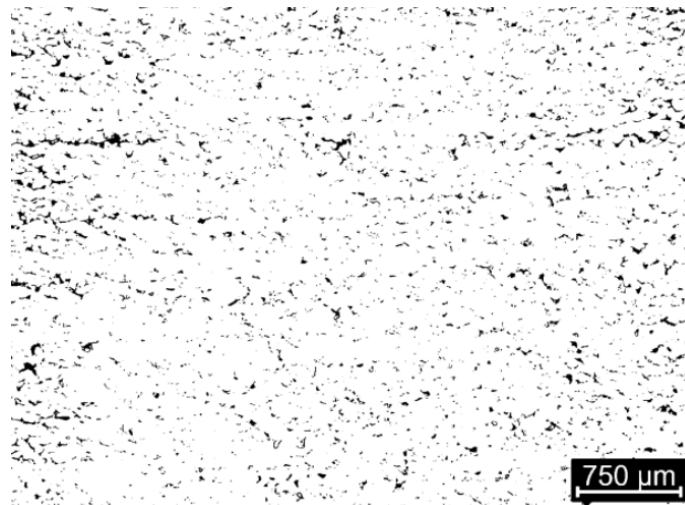


Figure 21 - Binary image of the cross-section After grinding to an accuracy of 4  $\mu\text{m}$  [48].

Despite the extensive efforts that have been made on the optimization of process parameters for LPBF of copper, its mechanical properties, electrical and thermal conductivities have been rarely investigated. For instance, Yan et al. [49], investigated the tensile properties and microhardness of fully dense copper specimens with a maximum relative density over 99%. Under the optimal processing condition (optimal LED of 0.50 J/mm), the mechanical properties reached the highest values: yield strength of 187MPa, the ultimate tensile strength of 248MPa, elongation to rupture of 9.2% and microhardness of 84 HV<sub>0.05</sub>. In fact, this high mechanical performance was achieved mainly owing to a very low defect content (Figure 22). However, they found that after annealing at a temperature of 773 K for 4 h in vacuum and then air cooling in atmosphere, recrystallization

took place inducing a sharp decrease in Yield Strength (YS) and Ultimate Tensile Strength (UTS), and a significant increment in ductility.

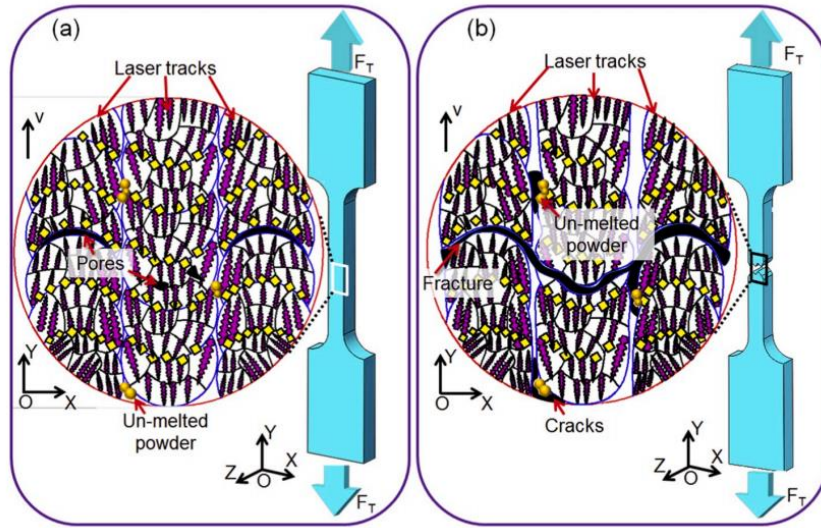


Figure 22 - Relationship between microstructure and tensile behavior of the LPBF copper samples. (a) Before and (b) after tensile test [49].

Huang et al. [43] compared the electrical conductivity, tensile strength and microhardness of pure copper specimens produced via LPBF and Cold Spray (CS) processes. Interestingly, their results proved that owing to the principles of the technologies a higher relative density in the case of CS samples was achieved (99.2% instead of 98.8% for the LPBF samples). As a consequence, this higher relative density resulted in a higher electrical conductivity and microhardness in the samples produced by CS technology (Figure 23). However, as can be seen in Figure 23(b), the CS samples exhibited a very brittle behaviour in comparison with the LPBF ones.

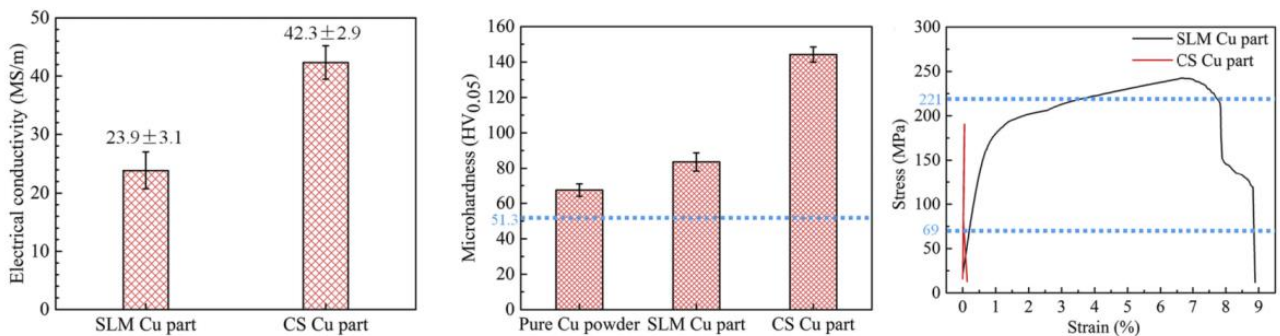


Figure 23 - Averaged electrical conductivity, microhardness and stress-strain curve of LPBF and CS Cu parts [43].

As discussed earlier, copper presents a very low laser absorption rate in the near-infrared region, that results in a low densification of the bulk parts which are processed via the lasers in this wavelength range [30]. In addition, it is reported that If the wavelength increases, the absorptance decreases even more, while at shorter wavelengths increases. For instance, for the green and blue lasers with the wavelengths around 520 nm, the laser absorptance increases up to 40% (Figure 24). For this reason, using the laser with shorter wavelengths such as green or blue laser was found to be a reliable technological solution to produce fully dense copper components. As an example,

Trevisan et al. [30] suggested to adopt a combined green and infrared laser system in order to improve the powder bed absorptance.

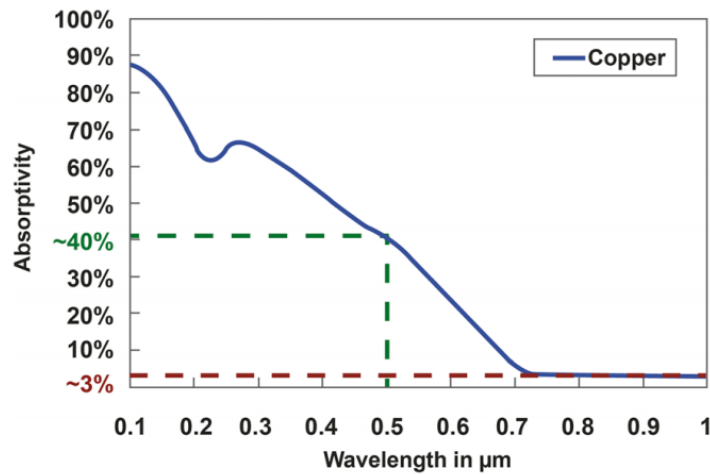


Figure 24 - Variation of pure Cu absorptivity as a function of wavelength [1].

Shibata et al. [56] compared the quality of the pure copper components using of a blue diode laser of 450 nm wavelength and an infrared laser. Their result confirmed that the absorption rate of pure copper processed via the blue laser increased up to six times with respect to those processed via the infrared laser. This discrepancy in the laser absorption then resulted in an interesting increase in filling rate and a sensible reduction in surface roughness of the printed part (Figure 25). In fact, in this work, a tube with a cross-sectional filling rate of 97.8% was built with just 100 W laser power and scanning speed of 5 mm/s. It has to be considered that upgrading an LPBF machine with a green or blue laser is not always economically or technologically feasible [53]. As a matter of fact, the LPBF machines using green or blue lasers in most of the cases can be employed for the production of only copper and copper alloys, and this implies the necessity for more machines in the production plant, if different types of materials need to be processed.

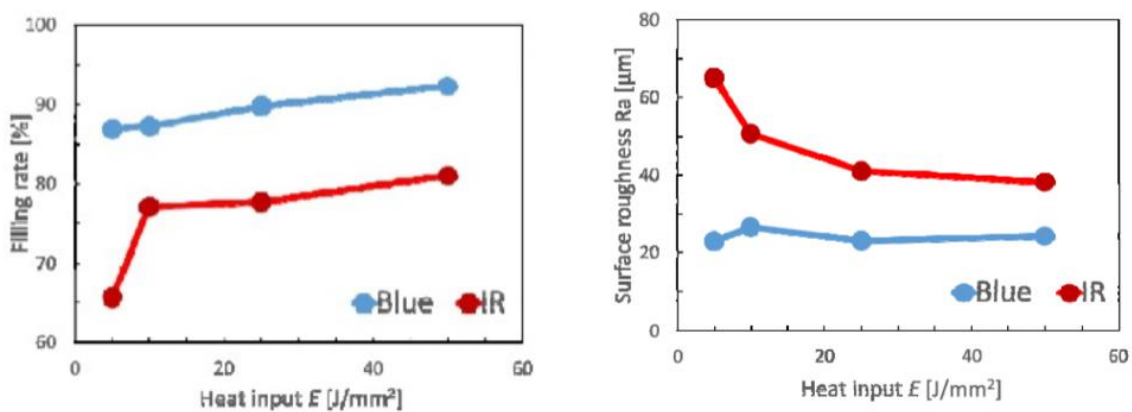


Figure 25 - Filling rate and Surface roughness vs Heat input [56].

Kaden et al. [26] fabricated pure copper cuboids and thin-wall structures with thicknesses below 100 μm using ultrashort laser pulses at MHz repetition rates and a center wavelength of 1030 nm. The ultrashort pulses, thanks to the high peak power, with respect to long pulse or continuous-wave lasers, present several advantages. It is possible to confine the active heating zone to the vicinity of the illuminated area, the thermal spreading can be easily controlled and the resolidification times

are extremely short. The best processing window using this laser was found to be only 20 W of average laser power and scanning velocities in the range of several hundreds of mm/s. The parts in the as-built state were characterized by high porous beads structure (Figure 26) due to the similar dimensions of powder grains and laser spot diameter (35  $\mu\text{m}$ ): as a matter of fact, with ultrashort laser pulses the particles were able to melt together only in the directly illuminated area.

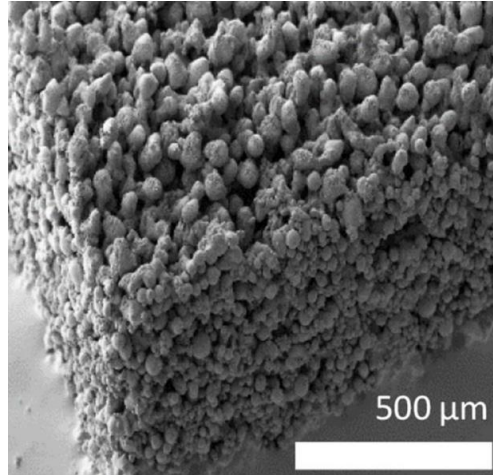


Figure 26 - SEM image of a cuboid showing a porous structure, which is generated by coalesced melting beads [26].

Apart from the technological based solutions such as process parameter optimization, using blue and green lasers, etc., other solutions based on the modification of the feedstock materials have been adopted to enhance the processability of copper through LPBF: material solutions. For example, Tahany et al. [38], applied a surface treatment to the copper powder using a fluidized bed method to reduce oxidation and improve the flowability of the powder. In this way, the new powder has higher process flexibility and productivity, longer storage life and requires a lower amount of laser power (Figure 27). As a second step, they developed two physics-based models, one for LPBF and one for DED, in order to define the optimum process parameters. With optimized LPBF parameters, they were able to produce 91% dense parts. In the case of DED, also powder deposition path and feed rate are optimized, resulting in increasing the copper absorption coefficient by 10–20% during deposition.

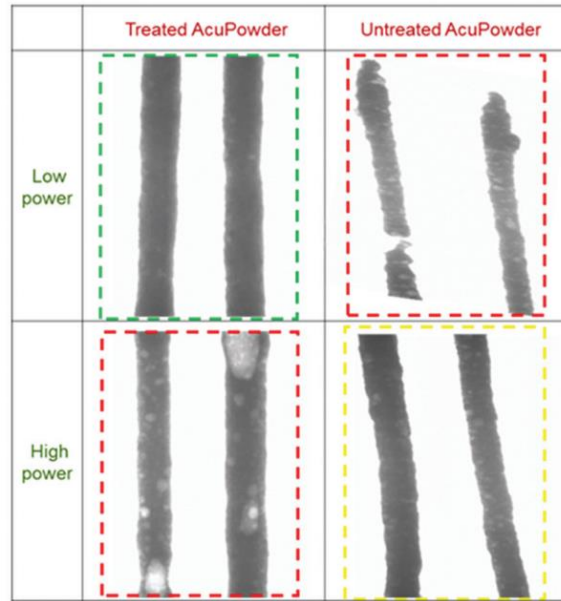


Figure 27 - Treated and untreated Cu powder [38].

Jadhav et al. [53], instead, modified a copper chromium powder by outward diffusion of chromium in a nitrogen atmosphere, forming a rim around the powder particles (Figure 28). This was fundamental in order to improve the optical absorption of the powder: if the alloying element is distributed uniformly within the copper bed, the resulting powder shows similar laser reflectivity as pure copper. The resulting treated powder requires just 20% of the laser energy needed by the virgin one. Moreover, the treatment has improved the flowability and reduced the oxygen pickup.

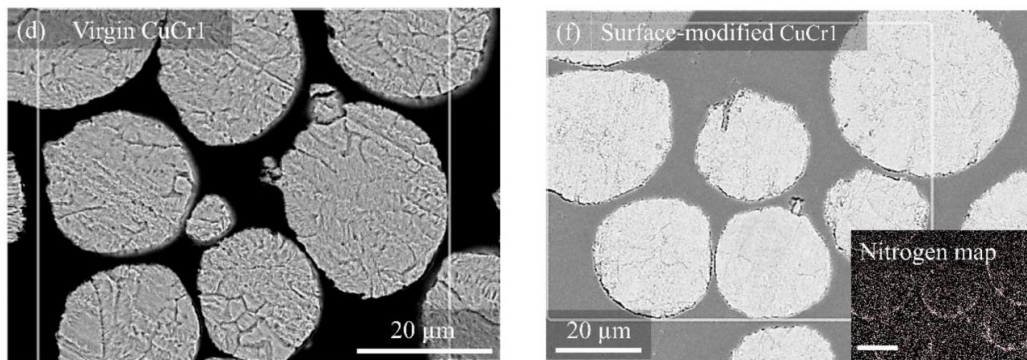


Figure 28 - SEM images of the cross-section of virgin and treated CuCr1 powder [53].

Other studies have proposed to add to copper powder a small quantity of alloying elements [27]. However, it should be highlighted that even a small quantity of a second element can drastically reduce the thermal and electrical conductivities of copper [25]. Jadhav et al. [27] added 0.1 wt.% carbon nanoparticles into the starting copper powder through the mechanically mixing method (Figure 29).

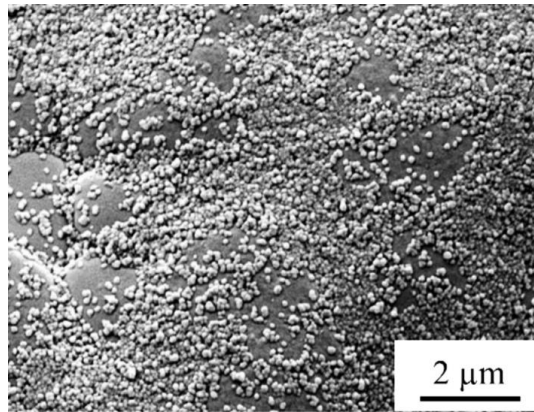


Figure 29 - Uniform distribution of C nanoparticles on the surface of a Cu particle [27].

Their outcomes demonstrated an improved optical absorption rate (precisely from 29% to 67%), enhanced flowability and in situ de-oxidation during the LPBF process. The fabricated components showed a relative density of 98%. However, this addition of carbon nanoparticles was found to be problematic. In fact, it is revealed that carbon nanoparticles and other impurities were segregated along the grain boundaries and consequently deteriorated the mechanical properties and electrical conductivity of the copper components. Therefore, it is necessary to use phosphorous free copper powder and to add some carbon-absorbing elements, such as chromium or titanium.

Finally, the last material solution that must be investigated is the possibility to use not pure copper, but one of its numberless alloys: the idea is to add one or more elements with lower thermal conductivity. Chromium is one of the most used since it enhances the mechanical strength of copper. The processability becomes less challenging with the presence of chromium [29], [41], [57]–[59], giving birth to highly dense components with elevated tensile strength. For instance, Zhang et al. [59] successfully realized Cu-Cr LPBF printed components with high strength and high conductivity. The final density of the samples was 99.98% when processed with optimized set of parameters (laser power of 2000 W, scanning velocity 600 mm/s, hatching space 0.2 mm and layer thickness 0.05 mm). The parts were heat-treated after the built, in this way the Cr particles precipitated from Cu matrix, improving drastically the UTS (468 MPa), YS (377 MPa) and electrical conductivity, which reached the value of 98.31% IACS: those values resulted higher than the one showed by samples fabricated by rolling with post-heat treatment

Zirconium and titanium are added as other promising alloying elements to Cu-Cr alloy, in order to improve hot ductility. An example is proposed by Ma et al. [41], which compared the Cu-Cr-Zr LPBF printed component with the wrought copper alloy: those two materials showed similar UTS, while the elongation at break results way higher in the case of the LPBF printed part. The optimized set of parameters found was of 370 W laser power, 650 mm/s scanning speed, and 120 mm hatching space. The resulting component showed a high density of 99.14%.

Other experiments were carried out by Wallis et al. [57], which focused their attention on the direct age hardening (DAH) of the built parts: the application of this heat treatment results in very fine Cr precipitates, which increase the hardness and UTS (from 287 to 466 MPa), while the ductility decreases slightly, but still presenting an acceptable value. Considering Figure 30 is possible to see that hardness reaches a peak value of 200 HV1 before the averaging, namely when the precipitates grow over the critical size for the restriction of dislocation. Increasing aging temperature, the

hardness peak shifts to shorter exposure times. However, it should be considered that thermal conductivity keeps growing by increasing aging temperature and time: the precipitates grow and become less dispersed, increasing the mean free path of phonons. They concluded that by adjusting the post-heat treatment, and process parameters it is possible to obtain the desired mechanical and thermal characteristics.

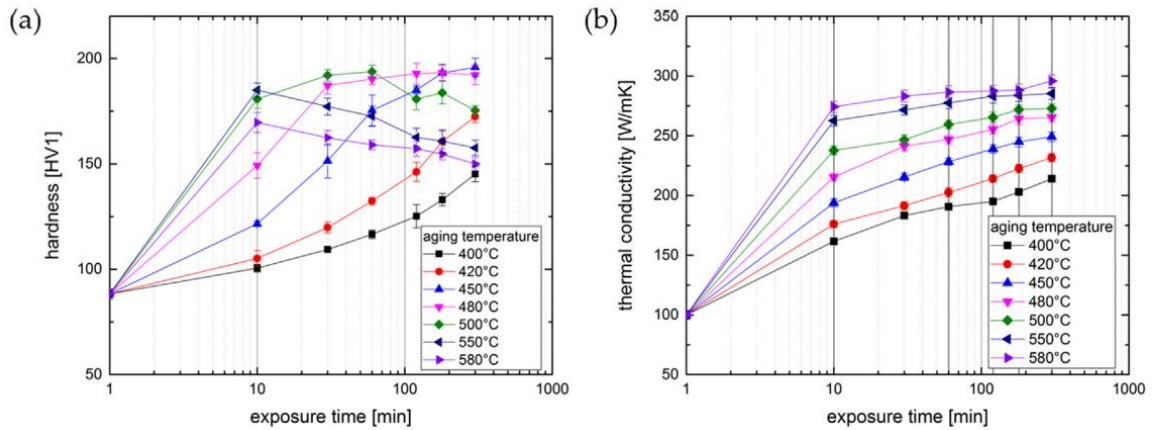


Figure 30 - Curve progression of the hardness (a) and thermal conductivity (b) after DAH as a function of exposing times and temperatures [57].

Popovich et al. [58] produced Cu-Cr-Zr-Ti alloy specimens with a high density of 97.9%. They applied solutions annealing and ageing to the printed parts, which resulted in an enlargement of the elongated grains. Those heat treatments are generally used to improve the strength: with solution annealing a solid solution of the alloying elements in the copper matrix is obtained, subsequently aging is aimed at the formation of further strengthening precipitates. Popovich et al. also evaluated the mechanical properties of the components, which resulted in UTS of about 200 MPa and elongation at break of about 13%. Those values also depend on the building direction: in the case of parallel built samples, the mechanical properties were slightly higher. The tensile test was also performed at 600°C and 800°C in order to highlight the effect of temperature: both UTS and elongation decreased. Finally, a comparison with the hot-rolled samples was carried out, showing that the UTS is 20-25% lower for the LPBF printed samples, due to the presence of residual porosity.

Sufiarov et al. [29], also, printed Cu-Cr-Zr-Ti bulk specimens with a density of 99.2% and smooth surface, by performing the optimization of process parameters. In addition, they compared the effect of uniform and a Gaussian distribution laser on the quality of the copper-based components (Figure 31). It was found that, with the former, a 800 W laser power is required to obtain high relative density, and partial sintering of the powder along the surface occurs, hindering the possibility of realizing complex geometries. With the Gaussian distribution it is possible to use 400 W laser power, obtaining a clean surface without sintering of powders.

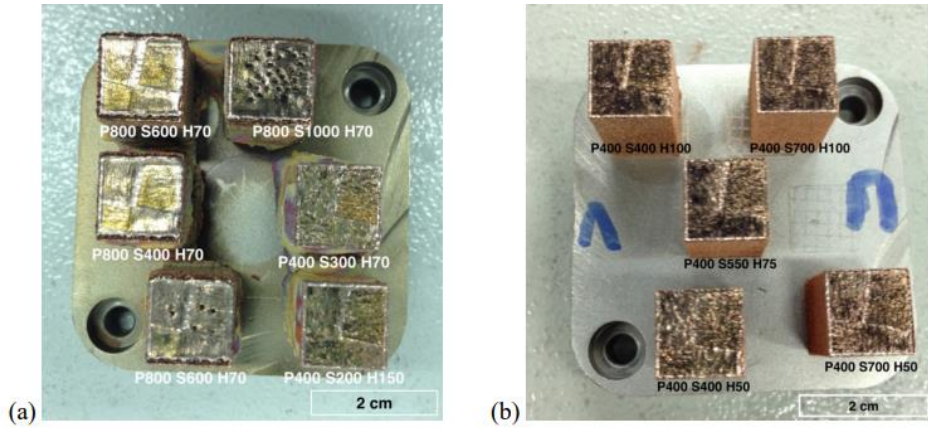


Figure 31 - Cu-Cr-Zr-Ti specimens produced by SLM using (a) laser with uniform beam profile with the laser power up to 800 W; (b) laser with Gaussian beam profile with the laser power of 400 W [29].

Another important alloying element is tin. Bronze processed by LPBF [60]–[62] showed lower laser reflectivity and thus result in fully dense parts (more than 99% relative density) even with a medium laser power input. In particular, Scudino et al. [60] fabricated highly dense bulk Cu-10Sn bronze components and compared them with those produced by casting. They showed that due to the refined microstructure of LPBF material, YS and UTS were much higher than the corresponding values of the as-cast ones. Other investigations regarding bronze were carried out by Mao et al. [61], who produced nearly fully-dense LPBF Cu-15Sn bronze specimens and analyzed their microstructure evolution and mechanical properties before and after annealing (Figure 32). They also performed optimization of process parameters which resulted in 187W laser power, 185 mm/s scanning speed and 0.17 mm hatch space. From this set of parameters, they obtained 99.6% dense parts and mechanical properties higher than traditionally fabricated Cu-15Sn components

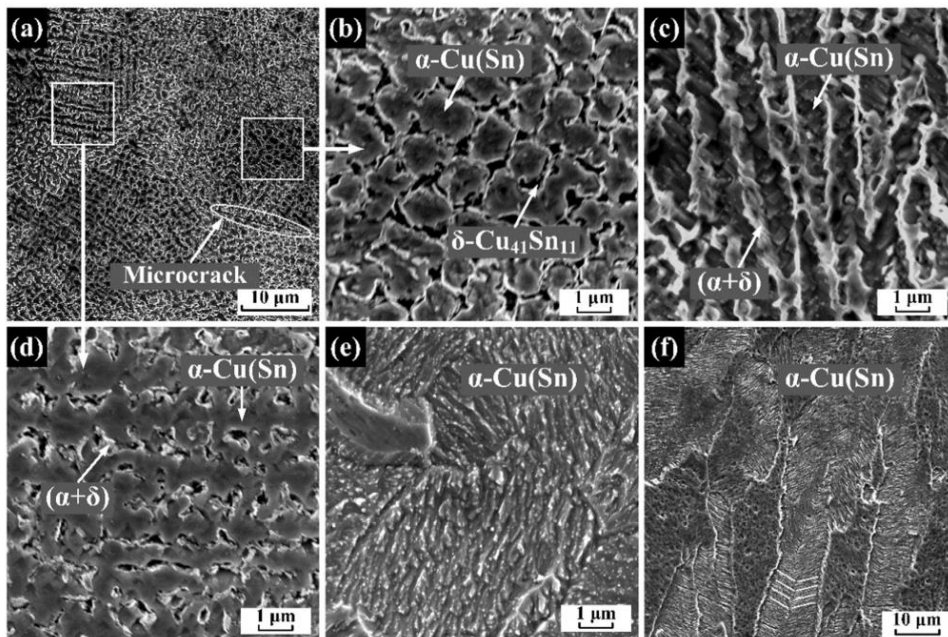


Figure 32 - SEM images of the LPBF Cu-15Sn samples (a–d) before and (e, f) after annealing at 600 °C for 4 h [61].

In Figure 33 (a) it is shown that the microstructure of the as built Cu-15Sn part consists of fine grains, with dimensions underneath  $2\mu\text{m}$ . At higher magnification (Figure 33 (b-d)) is possible to evidence the dendritic microstructure which grows epitaxially along the building direction. After annealing (Figure 33 (e,f)) the microstructure become coarser and a partial recrystallization has happened.

Another interesting result regarding copper-tin alloys is the one achieved by Zhang et al. [62], who manufactured Cu-15Ni-8Sn components by LPBF. Even in this case microstructure evolution and mechanical properties were analyzed. The resulting 99.4% dense part presented a YS of 522 MPa, UTS of 653 MPa, and elongation of 17%, values comparable with the tensile test of an optimized powder metallurgy component

Instead of alloying, it is possible to coat copper powder with other elements, as Lindstrom et al. [46] did with tin and nickel. Using an immersion deposition method, they succeeded in creating a new powder with higher absorptivity. Thus, the samples showed a lower amount of porosities with respect to in-situ alloyed powders with similar composition. In particular, this was visible with tin-coated copper components (Figure 33).

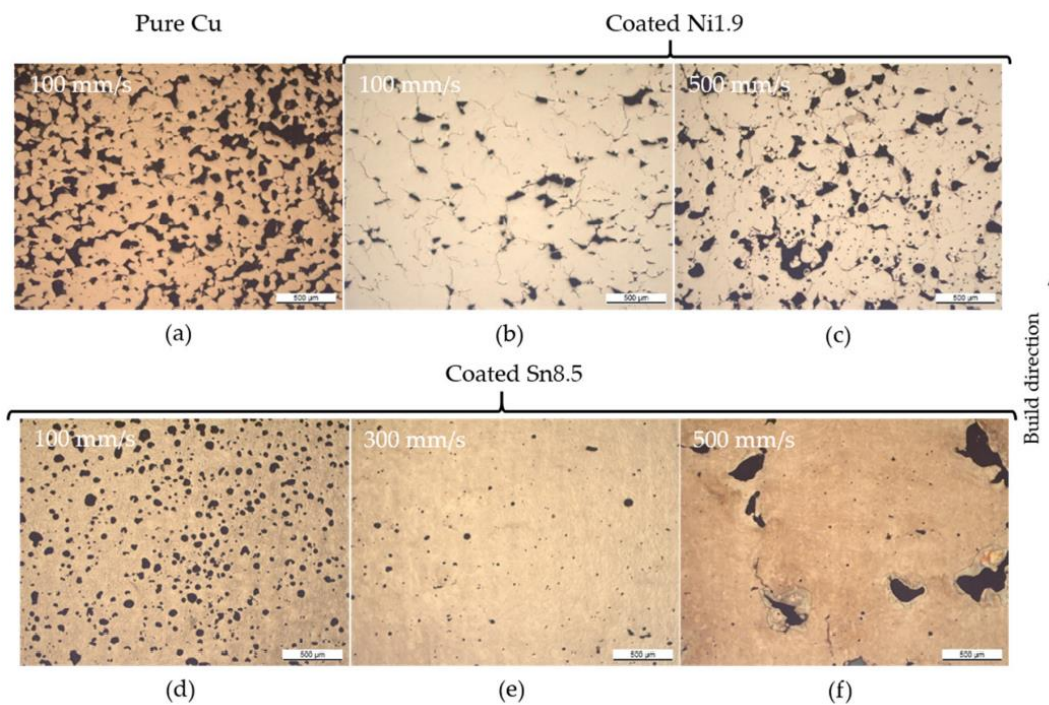


Figure 33 - Optical cross-sections of samples printed (a) Uncoated pure copper where the balling type porosities are evident. (b,c) Coated Ni1.9 where the porosity is reduced with respect to pure copper. (d,e) Coated Sn8.5 with spherical pores in the high energy density regime, large irregular pores in the low energy density regime and a relatively dense sample in the middle [46].

All in all, it can be conclude that through the surface treatment or addition of some alloying element to the feedstock materials it would be possible to overcome the challenges in the production of complex shape copper components and produce fully dense part with proper mechanical and thermophysical properties.

### 1.2.1.2. EBM

As another reliable and productive solution, EBM, which is a PBF technique, has been adopted to produce copper components. In this case, the energy source is no longer a laser, but an electron beam. Metal powder is fed from a hopper and distributed by a rake across a build plate [3]. The beam is generated in an electron gun (Figure 34) and it passes through an acceleration voltage. Then, it is focused by electromagnetic lenses and directed into the x-y plane by a magnetic scan coil. In this way the beam is moved without inertia, providing high build rates. EBM is considered a hot process. As a first step, the powder bed is pre-heated in order to provide a sintering of the particles. Then, the electron beam is focused, and the printing process starts. Analogous to LPBF process, once a layer is completed, the build plate is lowered, and the process is repeated again. EBM process is performed into vacuum, ensuring high purity and avoiding the risk of oxidation [63]. The main process parameters are power, focus and scan speed of the electron beam, which are adjusted by controlling the beam current, focus offset and speed function.

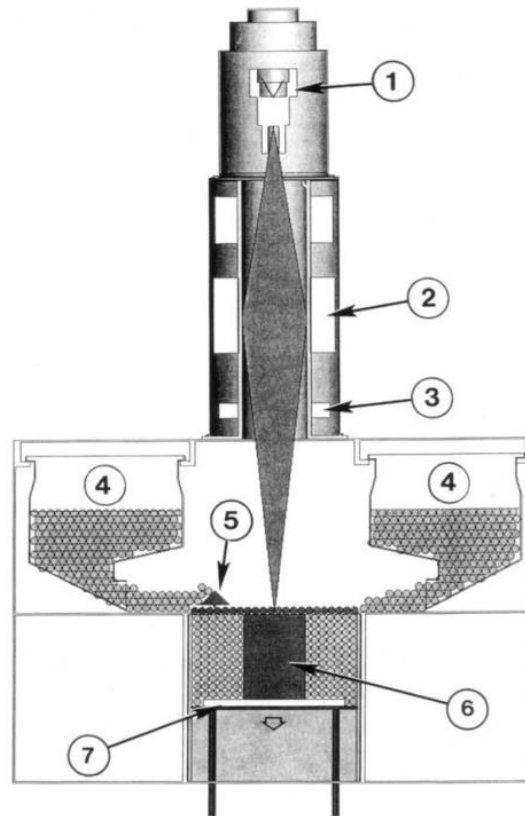


Figure 34 - Schematics of an EBM machine: 1) electron gun, 2) lens system, 3) deflection lens, 4) powder cassettes with feedstock, 5) rake, 6) building component, 7) build table. [64]

With respect to laser, the electron beam undergoes different absorption and reflection mechanism: the electrons are not affected by optical reflectivity [40], in this way all the energy provided, is deposited within the powder layer. This means that a higher percentage of energy input, up to 80%, is absorbed by copper and that the risk of back reflections is avoided. The second main advantage of this technique is, as already stated, the fact that the process is conducted entirely under vacuum, eliminating the concern for oxidation. On the other hand, it has to be highlighted that the spot size of the electron beam is larger than the laser beam diameter. Consequently, with EBM is not possible

to create small details on the components or thin walls and fins. Among all the AM technique, with EBM is possible to reach the highest values of relative density, tensile strength, electrical and thermal conductivity.

Guschlbauer et al. [28] investigated the correlation between processing parameters, microstructure evolution and physical and mechanical properties of EBM-processed pure copper specimens. In particular, it was evidenced that the microstructure changes from columnar to nearly equiaxed grain with the variation of scan speed and beam power (Figure 35). By applying an optimum set of parameters, with a process temperature of 530 °C, they succeeded in manufacturing of a 99.5% dense component with an electrical conductivity of 100% IACS. Although, the specimens showed a quite high crack density, due to internal stresses formed during the manufacturing process.

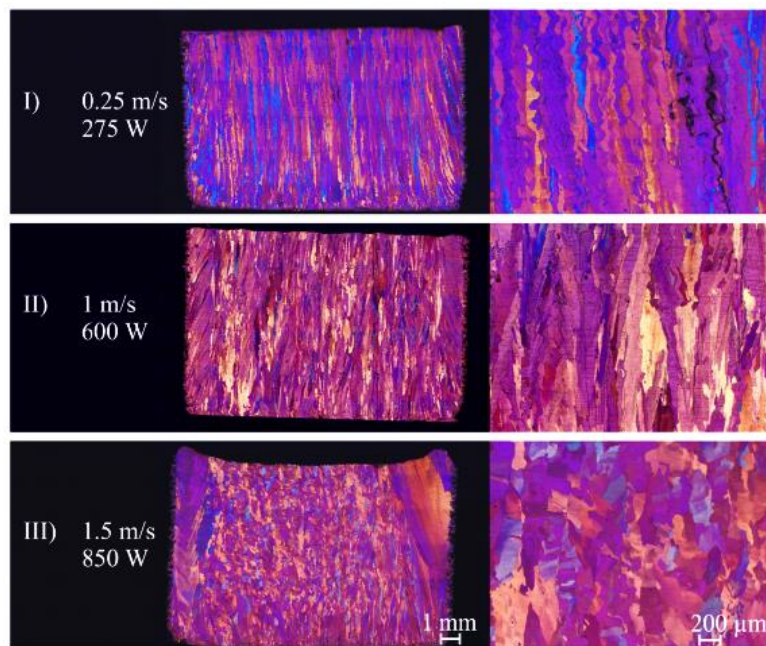


Figure 35 - Effect of scan speed and beam power over microstructure of etched cuboids specimens [28].

Another study performed regarding the influence of process parameters on final porosity was the one by Lodes et al. [63]. They processed 99.94% pure copper powder with a particle size ranging from 45 to 106 μm through an Arcam A2 EBM machine. They found out that with a too low line energy input, the powder is not molten, and the component show a high level of porosity (Figure 36). On the other hand, with an energy input higher than 0.35 J/mm the final density tends to decrease, the samples show balling effect and swelling at the edges, due to local overheating. With a line energy of ca. 0.275 J/mm the printed parts show the higher value of density (99.5%) independently of the beam velocity. In conclusion, they suggest, as technological solution, to adopt a parameter set of 3000 mm/s and 15 mA to process copper with EBM and obtain a relative density of more than 99.9%.

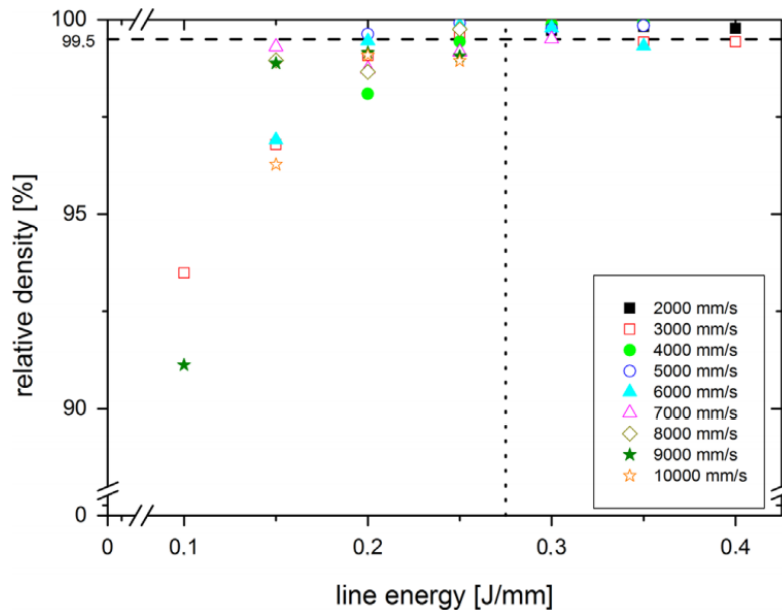


Figure 36 - Relative density of samples built with different combinations of beam velocity and current.

Raab et al. [65], instead, analyzed the electrical and thermal conductivity of the copper parts printed with an Arcam AB A2 EBM machine. Starting from a copper powder with a purity of 99.91%, a relatively high phosphorous content and a size of 45-105  $\mu\text{m}$ , they succeeded in producing 99.95% dense parts with a volume energy higher than 60  $\text{J}/\text{mm}^3$ . They demonstrated that with a higher the porosity content the electrical conductivity decreases, due to the reduced cross section. The highest values of electrical and thermal conductivity are obtained with the densest samples, respectively of 55.82  $\text{MS}/\text{m}$  and 400.1  $\text{W}/\text{mK}$ . The electrical conductivity does not reach 100% of IACS (59.7  $\text{MS}/\text{m}$ ): this is due to the presence of phosphorous in the raw material.

### 1.2.1.3. DED

DED is another laser-based AM process mainly used for metal materials and so also referred to Laser metal deposition (LMD). In contrast to the powder bed-based technologies, LMD provides a high build rate and allows for larger build volumes [3]. In DED the laser energy is used to melt the material as it is deposited on the substrate to generate a single track or a layer (Figure 37). In this way, the starting substrate can be either a flat new plate or an existing part onto which additional geometry will be added. The starting material can be fed in the form of powder or wire. A substantial difference with respect to other PBF processes is that in DED a Computer Numerical Control (CNC) workstation moves the laser beam and the deposition head around the part [66]. After each layer is formed, the deposition head moves away from the substrate by one-layer thickness and the process is repeated till the completion of the part.

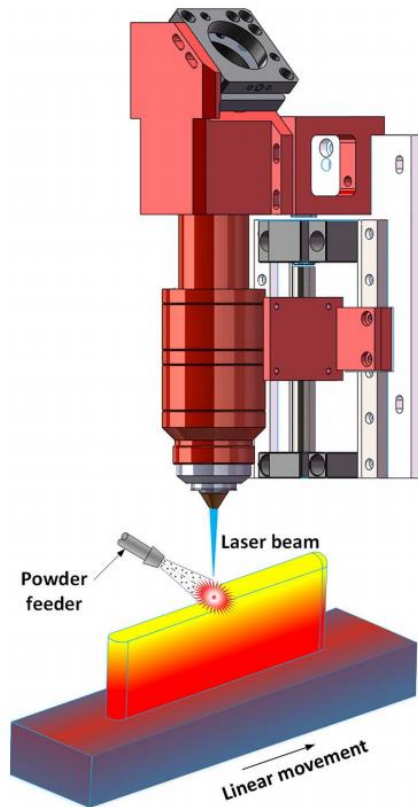


Figure 37 - Schematics of DED [67]

Being DED a laser-based process, it presents the problematics connected to copper's low laser absorption. Thus, a high energy input is required and there is a high risk of back reflections that can damage the machinery. Moreover, in order to avoid oxidation, as for LPBF, an inert gas flow is necessary [38]. Despite all of this, DED has an interesting advantage in building multi-material components. Using a combination of two or more deposition heads, it is possible to employ different materials which will be joined in the final part, achieving the desired properties.

Copper and stainless steel is an interesting combination in automotive and aerospace field, due to the high thermal conductivity, strength and corrosion resistance of the resulting material. Yadav et al. [66] deposited pure copper samples over the stainless steel 304 L substrate, which has different thermo-physical properties with respect to copper. They experimentally perform optimization of process parameters, analyzing the laid tracks from the point of view of porosity, which varied from 6 to 45 % during the tests, and track geometry and quality. They experienced that lower values of laser power and higher powder feed rate results in the discontinuous deposition, while on the contrary, there is a risk of cracked deposits. A continuous and defect-free deposition is observed between 6 to 18 kJ/g LEPPF (ratio of laser power and powder feed rate).

Siva et al. [68] successfully deposited pure copper over four different material substrates: copper, stainless steel, aluminum, and titanium. Those materials are characterized by different absorptivity, surface conditions and thermal conductivity. The energy source was a green laser; in this way, they overcame the problem of low absorptivity. Incorporation times for powder grains in the melt pools, size and geometry of the melt pool, a fraction of the power used for melting material and other aspects are analyzed as a function of the substrate material. In the case of copper over copper, the smallest melt pool with a high angle is found, and no oxides films were detected. This is due to the

instability of copper oxides at the high temperatures reached in the melt pool. Oxidation was quite relevant in the case of aluminum substrate, less for steel and titanium. Considering the same scanning speed, the copper substrate required the highest power, then, in decreasing order, aluminum, steel and titanium substrates.

#### 1.2.1.4. BJ

Binder Jetting (BJ) is also presented as a promising alternative in the production of complex shape pure copper components [40]. This process normally involves the use of two materials: the main material of the part and the binder one [69]. The latter is a liquid agent which glues the powder material between and within the layers. The metal powder is spread, and the binder is selectively deposited over the x-y plane (Figure 38). This process is iterated for building the entire part. Once the “green part” is completed, it undergoes several post-processes: curing, de-binding, sintering, infiltration, annealing and finishing. These post-processes sometimes take longer time than the actual printing and may incur significant costs. One of the significant advantages of BJ is that no support structures are needed: the build parts lie on the loose powder bed, which is not bonded together.

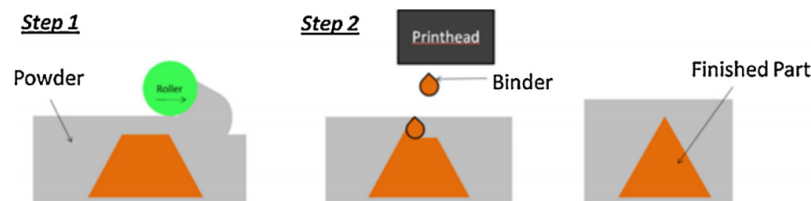


Figure 38 - Schematic of BJ process [70]

The main advantage of BJ over the other metal AM techniques is related to the nature of the process that does not depend on the materials properties. In fact, since the built is performed through the use of the binder, there is no concern over the material’s properties such as reactivity, melting point, thermal conductivity and optical reflectivity. Another benefit coming from the use of a binder is the low printing temperature, reducing the risk of thermally induced deformation and thermal residual stresses on the final component. Finally, BJ requires relatively low power input. On the other hand, part densification and sinterability need to be further improved, and in most of the cases post-heat treatments and HIP are required. Moreover, the parts are expected to have a coarse microstructure, since the parts have to undergo thermal treatments such as curing, sintering, and annealing. Hence, the mechanical properties of BJ parts are not as strong as the parts produced by LPBF and EBM.

Bai et al. [36] were the first to try printing copper components via BJ. They choose powders with median diameter ranging from 15 to 75  $\mu\text{m}$ : particles larger than 20  $\mu\text{m}$  are usually preferred in BJ from spreading point of view; small particles should be used in small volume percentage in order to enhance sinterability, surface quality, and resolution. The main parameters that have been optimized are layer thickness and binder saturation ratio. The first one should be about three times the particle size. Binder saturation ratio is the percentage of the air space between powder particles that is occupied by a binder volume. Its value should be high enough to obtain green part strength,

but at the same time lower than the oversaturation limit at which the powder can result in dimensional inaccuracy and low sintered density after binder burn-out. The maximum relative density obtained by Bai et al. was of 85.5% after sintering, showing a volumetric shrinkage of 43.4%. The highest tensile strength achieved was only 116.7 MPa, owing to the high porosity content.

Kumar et al. [70] investigated the combined effects of bimodal powder mixtures and HIP treatment on the BJ printed copper parts. In order to highlight the importance of powder dimensions, they used three powder configurations: 17 $\mu$ m, 25 $\mu$ m powders and a bimodal powder mixture of 5 and 30  $\mu$ m powders. The latter resulted in the highest relative density (90.52%). Moreover, it was the only one to experience an improvement in density after HIP: this post-treatment was effective only on sintered BJ parts with a minimum density of 90% (Figure 39). Due to the reduction in porosity after HIP application, despite the grain coarsening, both UTS and elongation of the bimodal samples increased from 144.9 to 176.35 MPa and from 18.81% to 31.28%, respectively.

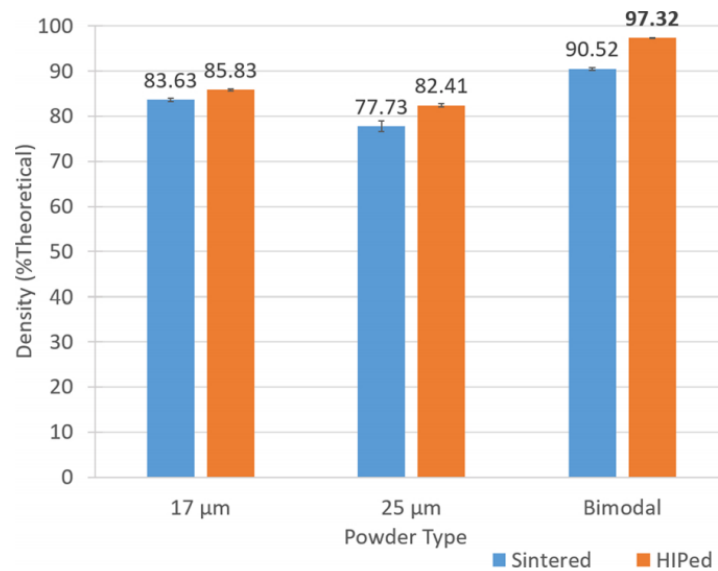


Figure 39 - Relative density of BJ parts, sintered and HIPed [70].

#### 1.2.1.5. ADAM and BMD

Atomic Diffusion is a recent indirect AM technique patented by Markforged. It consists of the extrusion of a filament of metal powder held by a plastic binder [71]. Actually, it can be considered as something in between extrusion printing and metal injection molding. The material is selectively deposited through a heated nozzle, forming the green part. The binder must be removed after the building stage: the green part must be oversized since it will experience shrinkage during sintering in the furnace. The obtained component shows a lower density with respect to other powder bed AM techniques. On the other hand, the precision is very high and can be further improved with finishing operations. Another interesting advantage of this technique is the possibility to use any powder, as no particular feature is required to be processed correctly.

Today only Markforged [72] is able to produce different complex shape components such as heatsinks, bus bars and induction coils, from a 99.8% pure copper powder through ADAM. The pure copper samples (Figure 40) that were produced through this technology exhibit a relative density of 98%, an electrical conductivity of 84% IACS and a thermal conductivity of 350 W/m.K. Both values are much higher than those obtained through the LPBF process, as presented before. For what concerns the mechanical properties, instead, the components printed by Markforged have lower values of UTS (193 MPa) and YS (26 MPa) and higher elongation at break (45%) with respect to LPBF printed parts.

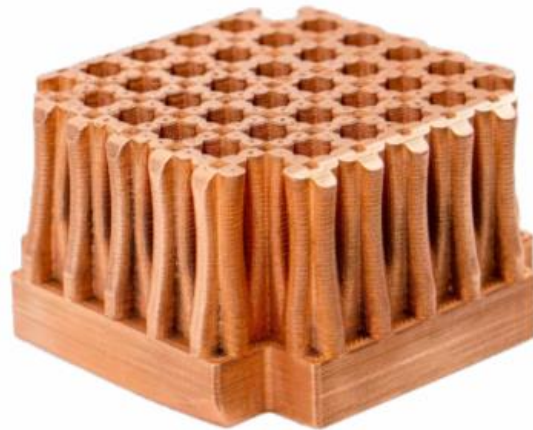


Figure 40 - Markforged example of copper component [72].

Desktop Metal is another company that has recently presented BMD, an AM technique very similar to Atomic Diffusion [71]. The very small differences between BMD and Atomic Diffusion are related to the type of extruder and binder used. At the moment also this company is trying to process copper powder in order to produce heat exchangers, inductors and antennas.

### 1.3. Conclusions

Combining the excellent electrical and thermal conductivity of copper with the ultimate design freedom of additive manufacturing techniques, would lead to the production of highly efficient heat exchanger components. However, several works have proved that the processability of copper through AM faced with several challenges. Thus, most of the resulting pure copper components show a very high level of porosity and poor mechanical and electrical properties. Over the last decade, there have been several research efforts to enhance the processability of copper through different AM techniques.

The laser absorptivity issue presented in LAM techniques can be faced changing the laser wavelength: some studies have successfully achieved the goal using a green or a blue laser, but this solution is not always implementable in the existing LAM machines. Other attempts to enhance the laser absorption rate have been sustained through material solutions. In particular, it is possible to add low quantities of other elements (i.e. carbon or chromium) and chemically modify the surface of the copper powder. On the other hand, the addition of different elements can significantly reduce the electrical conductivity of copper and create segregations at the grain boundaries, reducing the mechanical properties. Surface treatments are also helpful in improving the powder flowability and reducing the oxygen pickup.

For what concern LPBF, Stoll et al. [48] are the one who achieved the highest value of density (99.82%), using a 400 W laser power, scan speed of 600 mm/s and a laser beam diameter of 35  $\mu\text{m}$ . The resulting electrical conductivity was of 56.88 MS/m. Moreover, a multi-pass scan strategy is found to be very effective to stabilize the melt pool, as well as the use of a stainless-steel building platform.

Through EBM is possible to fabricate the most dense pure copper parts (99.95%), reaching 100% IACS [28]. On the other hand, this technique is not suitable for producing small details, due to the dimensions of the electron beam.

Interesting results can be obtained even with DED, BJ and ADAM. The first process is particularly suitable for the printing of multi-material components. With both BJ and ADAM an important reduction of energy requirement can be achieved, but an oversize of the component must be considered to face the evident shrinkage experienced by the green part during sintering.

# Chapter 2

## Materials and methods

In this chapter, the rough materials adopted, the equipment used, and the experimental activity are presented.

### 2.1. Materials

Copper powder employed in the present experimental work has been supplied from LPW Technology of Carpenter Additive (U.K.) Ltd. The powder is 99.8% pure. The particles are gas atomized, and the average size is 20 – 50  $\mu\text{m}$ . As explained in the datasheet, this powder is suitable for the LPBF process.

The graphite used is, instead, from Alfa Aesar by Thermo Fisher Scientific. Even for this material, the purity is higher than 99%. The average particle size is 7 - 11  $\mu\text{m}$ .

### 2.2. Mixtures preparation and characterization

In order to establish the correct amount of graphite to be added to pure copper without negatively affect its processability, different mixtures have been prepared and analyzed: Cu- 0.25 wt.% C, Cu - 0.5 wt.% C, Cu – 1 wt. %C, Cu - 1.5 wt.% C, Cu – 2 wt.% C. To estimate the effect of the addition of the second element, also the available pure Cu powder has been compared as the reference sample.

The mixtures have been prepared by mixing them in a low energy jar mill for 24 hours. The first analyses conducted were the density and flowability evaluation, performed through the Hall Flowmeter. This method is a simple method to assess the density of the loose sample materials, e.g. powders. At first, the apparent density has been measured: the density cup has been filled with the powder, and the weighed mass has been divided by its apparent volume. Secondly, also the tapped density has been gauged: the method was similar to the previous, but in this case, the cup has been filled under standard conditions of tapping. With tapped density, it was possible to evaluate the amount of gas that tends to remain entrapped between powder particles. To increase the reliability of both measurements, the procedure has been repeated three times for each mixture using fresh samples.



Figure 41 – Hall Flowmeter.

From the analysis of bulk and tapped density, it was also possible to obtain information regarding the flowability of the powder by means of the Hausner Ratio (HR). This parameter indicates the particles' ability to arrange themselves optimally in a certain system, and it is determined as in Equation (1).

$$HR = \frac{\textit{tapped density}}{\textit{apparent density}} \quad (1)$$

When its value ranges from 1.0 to 1.1, the powder has excellent flowability; from 1.12 to 1.18, it has good flowability, and finally, if the value is between 1.19 and 1.25, the flowability is fair [73].

The second test applied was the spreadability test. It consisted of spreading a small amount of powder over a plate through a roller. The selected space between the roller and the plate was chosen equal to 20  $\mu\text{m}$ . The plate used for this test was a stainless steel platform employed in the LPBF process. In this way, it has been possible to simulate the flowability and spreadability of the powder mixture. The ability of the powder to be spread as a uniform layer over the substrate is a crucial property in the LPBF process. The spread layers, then, have been analyzed at the stereomicroscope in order to identify the best possible solution.

As the last step of the characterization, all the mixtures have been analyzed at Scanning Electron Microscopy (SEM), with the Phenom PRO SEM machine. This particular instrument uses a focused beam of electrons to scan the surface of the samples and create a highly detailed image of them. The magnification used in SEM ranges from 20x to 30000x. This analysis is crucial to study not only the exact chemical composition of the mixture but also its morphology. Apart from the PSD, the shape of the particles influences the powder mixture's flowability. In fact, as it is well documented, the presence of coarse and irregular particles reduces their ability to rearrange and form a uniform powder layer [24]. For this reason, it is fundamental to highlight the eventual defects due to atomization and oxidation of the particles.

From the analysis just described, it was clear that the complete coverage of the copper particle was not successfully achieved and that the spreadability was drastically reduced. As a result, a sixth

mixture has been prepared: Cu – 0.5 wt.% milled C. Graphite flakes have been milled in order to reduce their dimensions and allow them to better stick to copper particles. Also, this mixture has been observed at SEM and chemically analyzed.

### 2.3. LPBF machine

The machine used to print the copper-graphite specimens and SSTs by LPBF is the Concept Laser MLabR from GE Additive based on the technology LaserCUSING®, present in the Integrated Additive Manufacturing (IAM) lab of the Politecnico di Torino. It is provided with a build envelope of 90 x 90 x 80 mm. The laser used is a fiber laser with a maximum power of 100 W. The specifications of this machine are the following: layer thickness of 15 - 30 µm, the maximum scanning speed of 7 m/s, focus beam diameter approximately of 50 µm. The process is carried out under an inert atmosphere thanks to the presence of argon flow inside the build chamber.

### 2.4. Samples preparation and characterization

In order to show the challenges presented by copper during the built stage through LPBF, it was tried to print cubic specimens of this pure metal. Further, the material solution proposed in this thesis has been adopted, and it was tried to process different mixtures of Cu – C.

The cubic specimens with 10 x 10 mm dimensions in the x-y directions were printed on a stainless steel plate. The stability of the melt pool is influenced by the thermal conductivity of the material of the base plate. According to the study conducted by Colopi et al. [1], stainless steel is very suitable for this purpose, thanks to its reduced thermal conductivity that increases the stability of the melt pool during the process.

The different mixtures employed for the jobs were Cu – 2.0 wt.% C, Cu – 1.0 wt.% C and Cu – 0.5 wt.% milled C. For each set of specimens, different process parameters have been adopted, and the volumetric energy density (VED) is calculated using the following Equation:

$$VED = \frac{P}{vhs} \left[ \frac{J}{mm^3} \right] \quad (2)$$

Due to the poor flowability of the powder mixture as well as the high reflectivity of the powder mixture, the firsts trials were not successful, and so, cubic specimens with an approximate height of 0.2 mm were achieved. Thereafter, these cubes have been analyzed using a stereomicroscope to understand better the source of their low processability. Then, in order to have a basic investigation on the effect of graphite on the laser absorption of copper, it was decided to compare the size and geometry of the melt pool in the Cu-C samples with those of pure copper. Hence, two sets of single scan tracks (SSTs) were printed over the Al discs. The first was pure copper, and the latter Cu – 0.5 wt.% milled C. The schematic of each SST is shown in Figure 42. It should be highlighted that the parameters adopted for the contour tracks are different from the ones used for the internal tracks, which are the melt pools that have been analyzed.

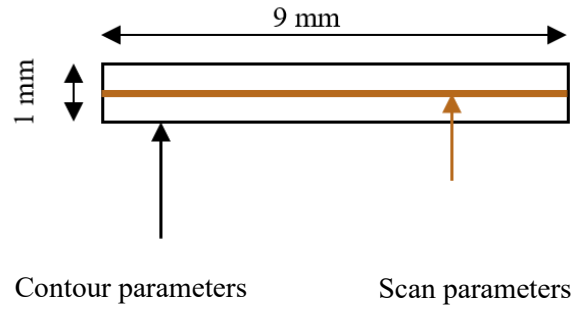


Figure 42 – Schematic of a SST sample

The SSTs were all characterized according to the procedure adopted by Aversa et al. [74]. So, as a first step, the samples have been observed on-top by means of the stereomicroscope Leica EZ4W. Further, the Al discs have been cut in order to mount with acrylic resin the cross-section of the scan tracks. Next, they have been polished with sandpapers from 320 to 4000 and diamond paste up to 1  $\mu\text{m}$ . Finally, the mounted and polished specimens have been chemically etched so to be observed at the optical microscope. Images have been saved, and some geometrical features of the melt pools have been measured with the software ImageJ, as showed in Figure 43.

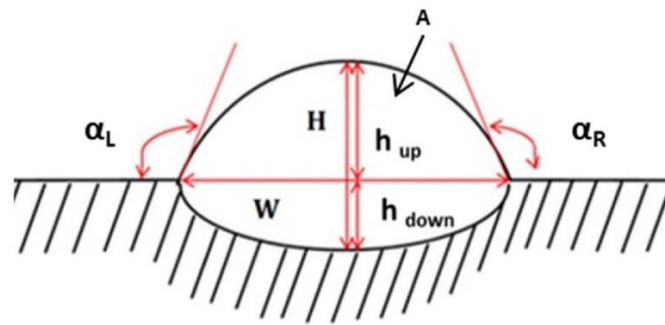


Figure 43 – Geometrical features measured for each scan track [74].

The main objective of this study was to correlate the geometry of the melt pool with the amount of Linear Energy Density (LED) absorbed during the process. The value of LED has been calculated for each SST as

$$LED = \frac{P}{v} \left[ \frac{J}{mm} \right] \quad (3)$$

# Chapter 3

## Results and Discussions

### 3.1. Characterization of the mixtures

In this chapter, the results obtained from the characterization of the powders are reported.

#### 3.1.1. Apparent and tapped density

As explained in the previous chapter, the powders, in order to be selected for the manufacturing of specimens, have been tested and analyzed. The first study performed over the mixtures was the apparent and tapped density: the results were collected and displayed in the following graphs to show the effect of the addition of different amounts of graphite to pure copper powder.

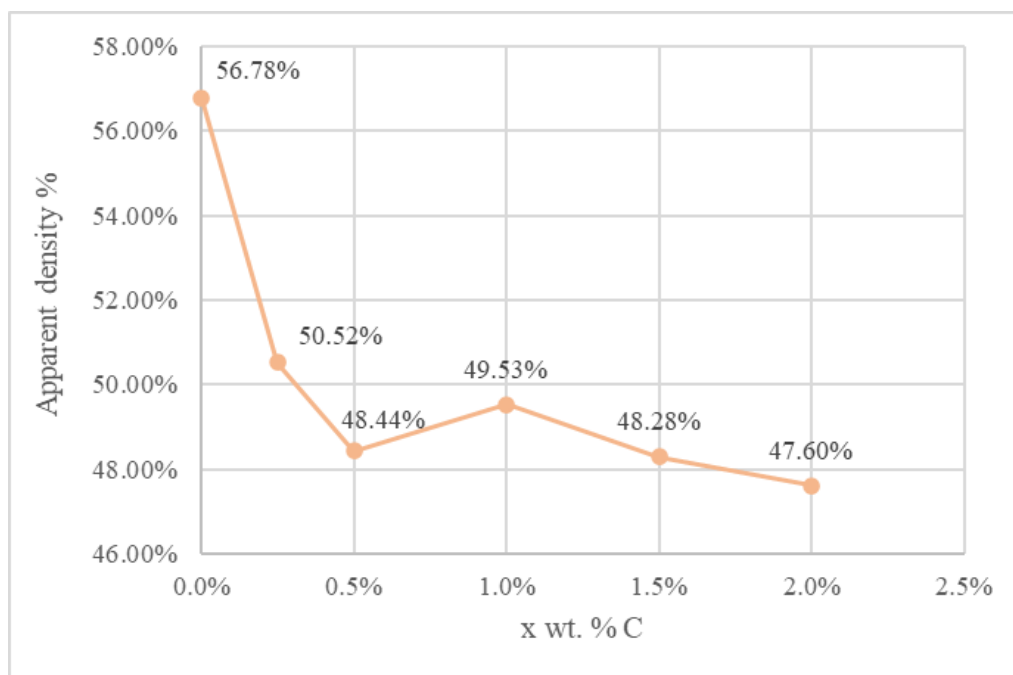


Figure 44 – Apparent density of the mixtures powders as a function of the graphite content.

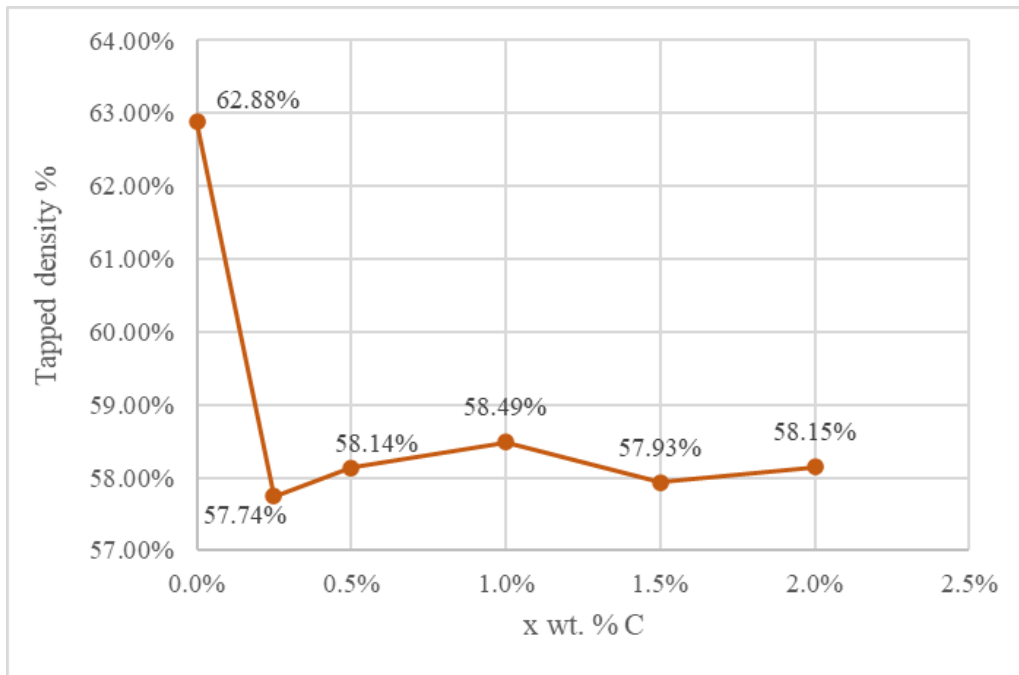


Figure 45 – Tapped density of the mixtures powders as a function of the graphite content.

From this first analysis, it is possible to deduce that any addition of graphite to pure copper reduces both apparent and tapped density: as a matter of fact, graphite has a lower density with respect to copper. However, this phenomenon is also due to the loss of sphericity of the particles: as already explained, more spherical particles are able to achieve a more efficient packing [21].

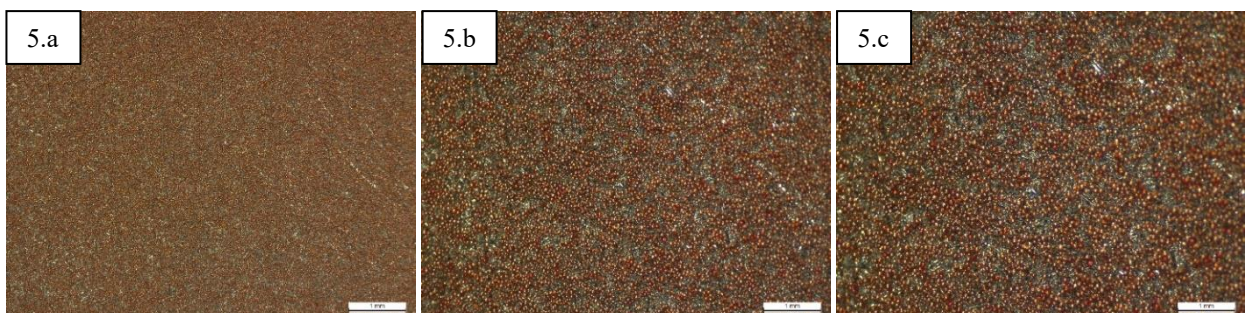
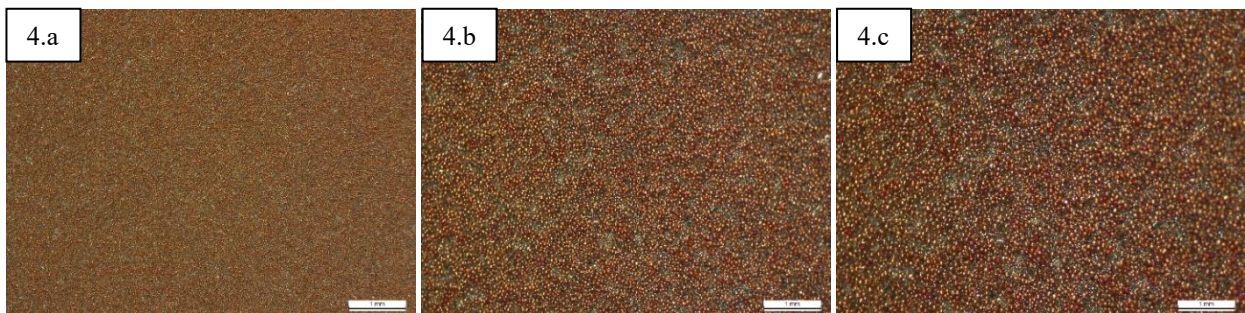
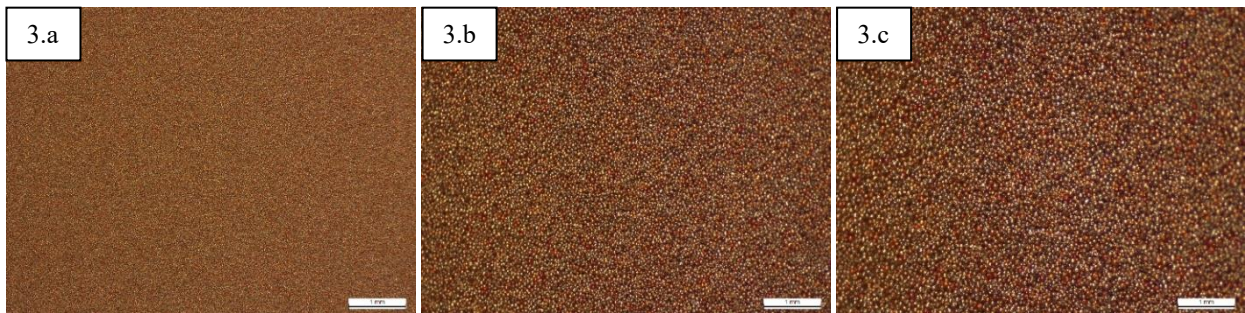
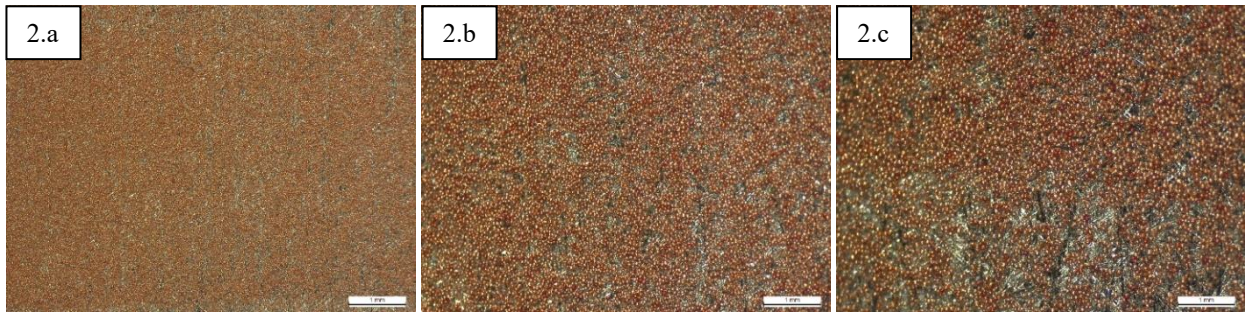
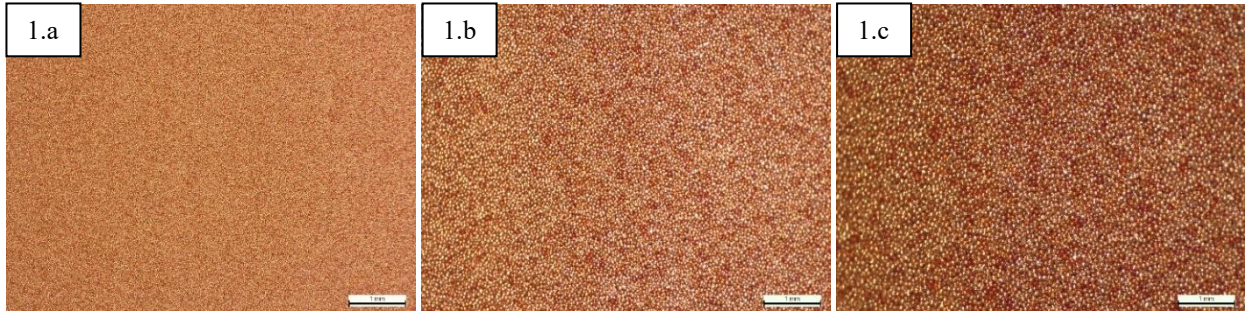
Afterwards, the Hausner ratio (HR) factor was calculated, and the obtained values are reported in the following table. It is clear that only pure copper above all the mixtures presents an excellent flowability ( $1.0 < H < 1.1$ ), while with the addition of even a small amount of graphite flakes, the ability to flow drastically get worse ( $HR > 1.19$  fair flowability).

	pure Cu	Cu - 0.25% C	Cu - 0.5% C	Cu - 1.0% C	Cu - 1.5% C	Cu - 2.0% C
Apparent density	0.57	0.51	0.48	0.50	0.48	0.48
Tapped density	0.63	0.58	0.58	0.58	0.58	0.58
Hausner Ratio	1.11	1.14	1.20	1.18	1.20	1.22

Table 1 – Values of apparent and tapped density and Hausner ratio of the mixtures prepared

### 3.1.2. Spreadability test

The second analysis was the spreadability test. The layers, once spread, were observed at the stereomicroscope. The collected images are reported at different magnifications, respectively 1x, 2x and 4x.



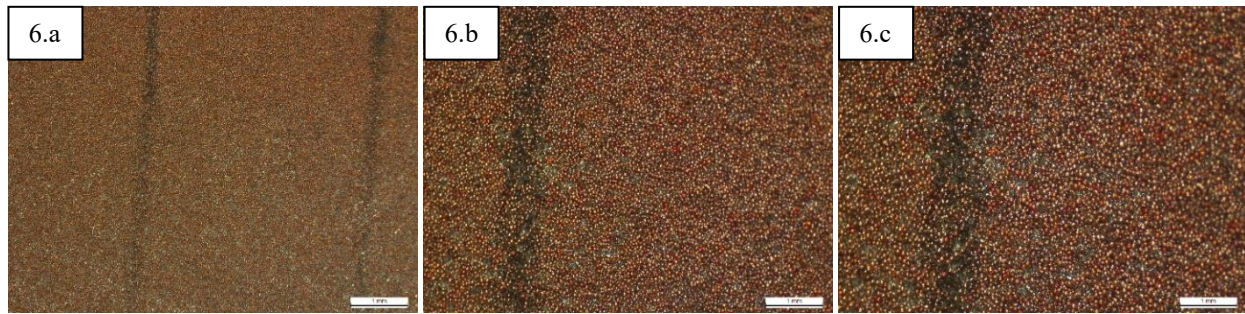


Figure 46 - Stereomicroscope images of the spreaded layers. 1) Pure Cu, 2) Cu – 0.25% C, 3) Cu - 0.5% C, 4) Cu - 1.0% C, 5) Cu - 1.5% C, 6) Cu - 2.0% C. a) magnification at 1x, b) magnification at 3x, c) magnification at 4x

As it is possible to see in Figure 46, pure copper shows a perfect uniform distribution over the plate, thanks to the spherical shape of the particles [21]. By adding a small quantity of graphite, the spreadability is negatively affected, and the mixture cannot fully cover the base plate. In the opposite case, if the amount of graphite is over 1.5 wt.%, it cannot mix homogeneously with the copper and forms agglomerates. From the spreadability point of view, it seems the best solution is to add 0.5% of graphite.

Finally, the last step of the characterization of the mixtures consisted of the analysis through SEM. In the following paragraphs, the results obtained from this observation are reported. The images collected for each powder at different magnifications are reported in the Appendix as well as the chemical composition analysis when effectuated.

### Pure Cu

As for the other characterization tests, the first powder to be analyzed was pure Cu. The first aspect that was analyzed through SEM is the shape of the particles. The powder of copper available is gas atomized and generally shows a spherical shape. Anyway, it is possible to see the presence of some satellites, particles with satellites and elongated or deformed particles: examples are reported in Figure 47. These irregularities, as already explained, negatively affect the flowability and packing density of the powder.

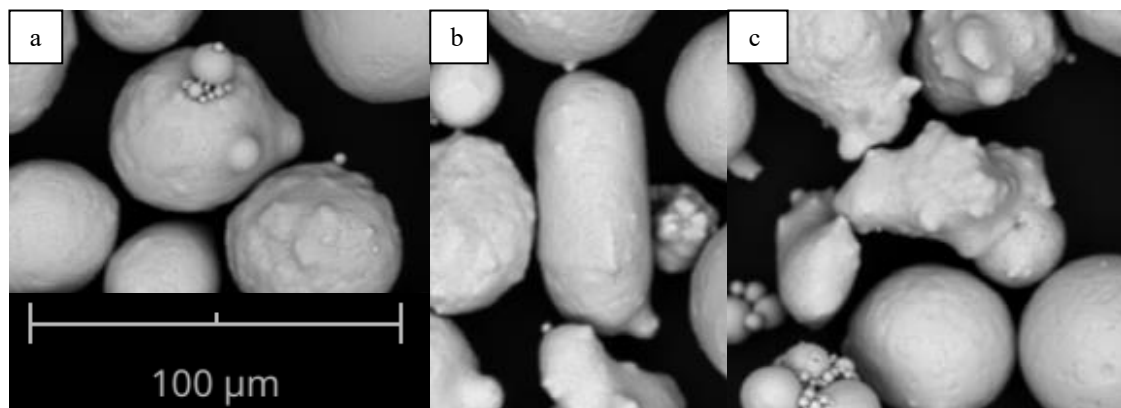


Figure 47 – Defects of gas atomization of pure Cu. a) Satellites. b) Elongated particle. c) Irregular particle.

Another defect that is detectable with SEM analysis is the oxidation of copper. As already stated, copper has a high sensitivity to oxidation, and so it must be kept under a protected environment.

From the chemical composition analysis, a considerable amount of oxygen is evidenced, and some particles are visibly covered by an oxide layer (Figure 48).

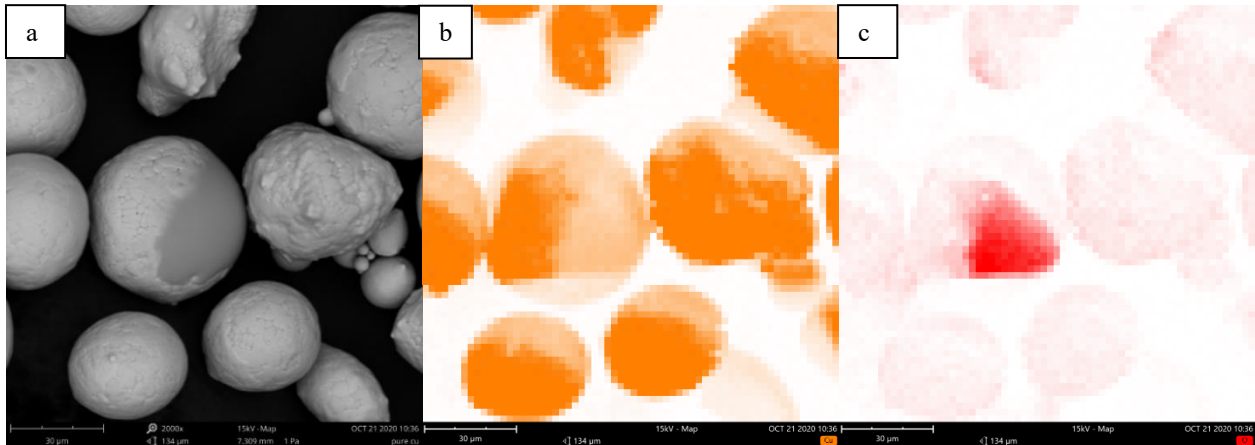


Figure 48 – a) Example of the particle’s surface with evident oxidation. b) Cu of the oxidated particle. c) Oxygen around the oxidated particle.

### Pure Cu sieved

Given that the ideal PSD for LPBF machines should remain below a certain limit, it was decided to sieve copper at 40  $\mu\text{m}$ . In this way, only the powder collected below the sieve will be used for the first job.

Both powders, sieved above and below 40  $\mu\text{m}$ , were observed through SEM (Figure 49).

From the images collected from the analysis of pure copper remained above the sieve, the particles appear perfectly spherical and the PSD is strongly limited, being the dimension ranging from 40 to 50  $\mu\text{m}$ . For what concerns the powder sieved below 40  $\mu\text{m}$ , instead, it has a wider PSD but results more irregular. As a matter of fact, the satellites had passed through the grid of the sieve and remained with the smaller particles.

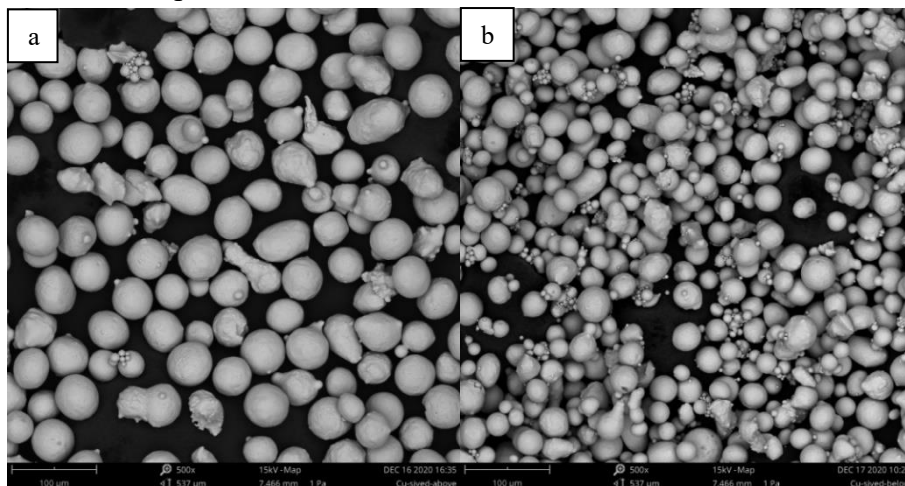


Figure 49 – a) Pure copper sieved above 40  $\mu\text{m}$ . b) Pure copper sieved below 40  $\mu\text{m}$ —magnification of 500x.

## Milled graphite

Graphite flakes have been milled in order to reduce their dimensions and improve their contact with the surface of the copper particles. This graphite has been analyzed using SEM before mixing with pure copper. Images have been taken even at high magnifications suggesting the incredibly small dimensions of the flakes.

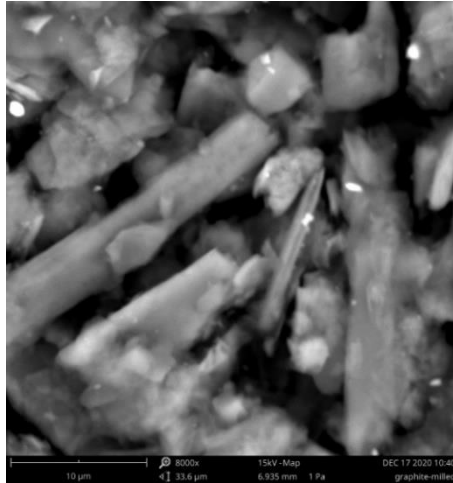


Figure 50 – Milled graphite at 8000x

## Cu – 0.25% C

Secondly, Cu – 0.25% C mixture was analyzed. In Figure 51, at a magnification of 1000x, copper and graphite are highlighted in different colours better to analyze the distribution of graphite in the mixture. The graphite flakes stick to the spherical particles of copper, but they are not enough to fully cover them. This suggests that a maximum of 0.25% in weight is insufficient to be added to pure Cu since it would not show a significant improvement from the absorptivity point of view.

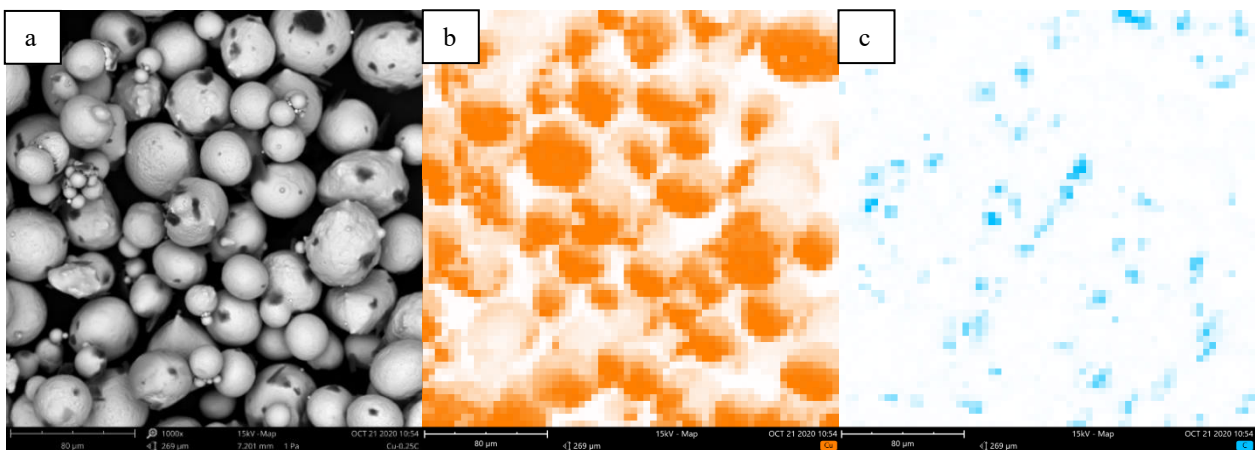


Figure 51 - a) SEM images of Cu – 0.25% C at 1000x. b) Cu in the mixture. c) C in the mixture.

## Cu – 0.5% C

Further, Cu – 0.5% C is analyzed using SEM. In this case, an improvement from the coverage point of view can be detected. The amount of graphite can be considered sufficient to cover copper particles, but the full coverage is still not achieved. The flakes are distributed homogeneously, and no agglomerations are visible.

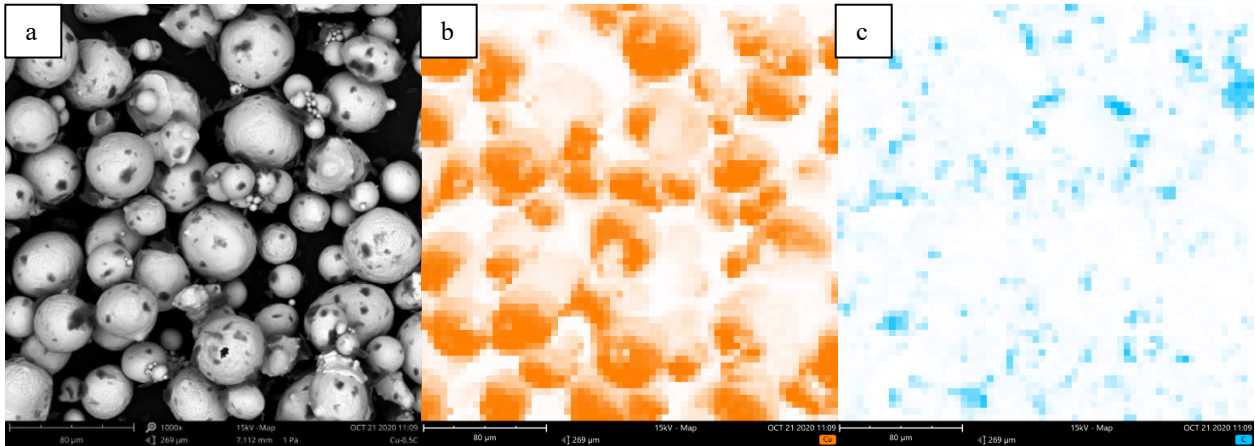


Figure 52 - a) SEM images of Cu – 0.5% C at 1000x. b) Cu in the mixture. c) C in the mixture.

## Cu – 0.5% milled graphite

Cu – 0.5% milled C has been analyzed via SEM as well. In particular, this powder has been compared with the Cu – 0.5% C, where the graphite was not milled. At first sight, it is clear that graphite has mixed more homogeneously around copper particles. By comparing the obtained results in Figure 53 to the one in Figure 52, it is possible to deduce that by adding the same quantity of graphite, the distribution around copper particles significantly depends on the size of the flakes. By using milled graphite, it is possible to get a more homogeneous distribution and a higher coverage. This suggests that this mixture would show higher processability during the printing process with respect to the other mixtures presented before.

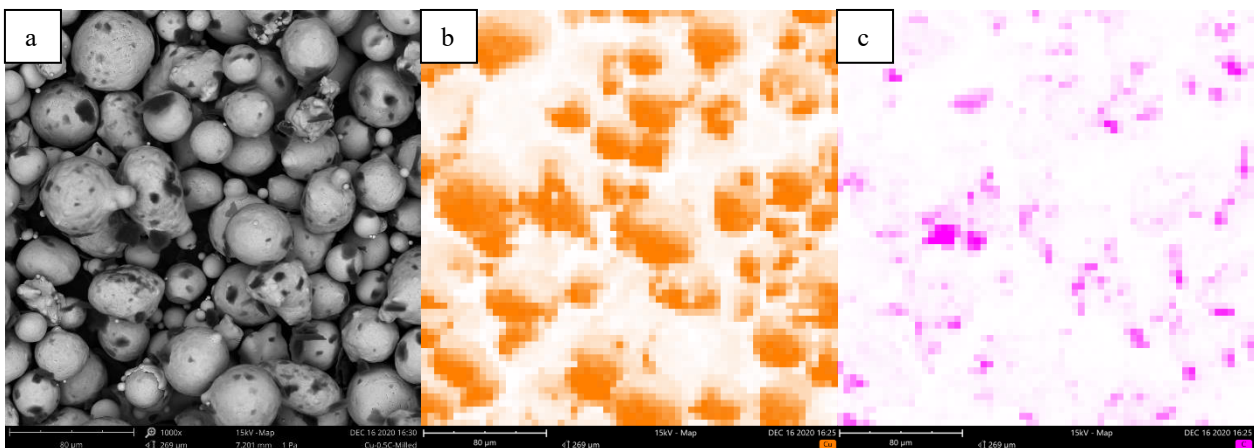


Figure 53 - a) SEM images of Cu – 0.5% milled C at 1000x. b) Cu in the mixture. c) C in the mixture.

## Cu – 1.0% C

The successive mixture prepared and analyzed was Cu – 1% C. From the images taken, it is possible to state that this mixture is as well interesting. Graphite has stuck around the particles providing high coverage. By a deeper observation of the mixture, small agglomerates can be detected. So, by adding 1% of graphite to pure copper, it is possible to achieve a higher coverage of the particles, but, on the other hand, the Van der Waals forces start to hinder the possibility to obtain a homogeneous distribution of the flakes.

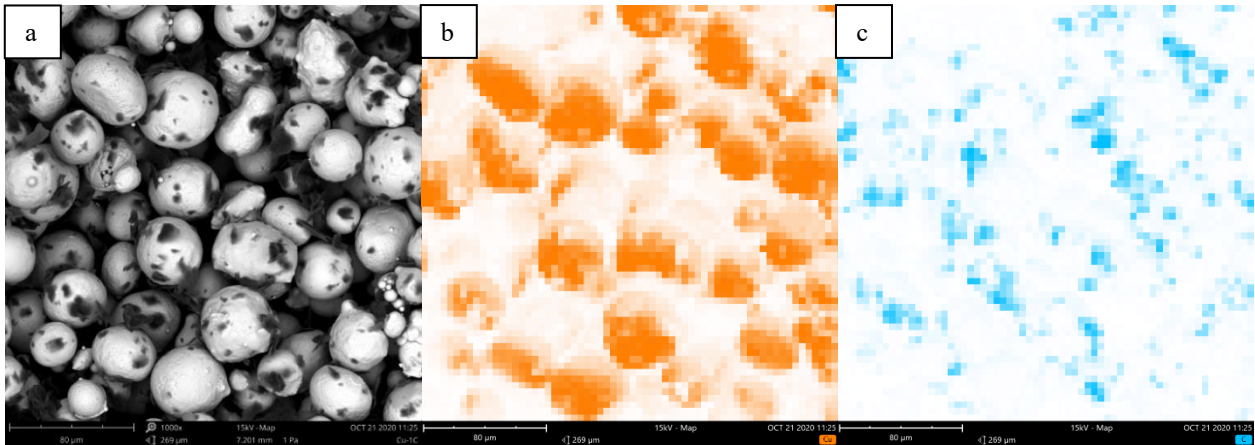


Figure 54 - a) SEM images of Cu – 1.0% C at 1000x. b) Cu in the mixture. c) C in the mixture.

## Cu – 1.5% C

Afterwards, the mixture Cu – 1.5% C has been observed at different magnifications. By adding 1.5% in weight of graphite to pure Cu, the flakes are not able anymore to mix homogeneously and starts to form several agglomerations. From the SEM analysis, it can be concluded that in this mixture, the graphite is not distributed homogeneously and forms agglomerates among the copper particles without giving any further contribute to their coverage.

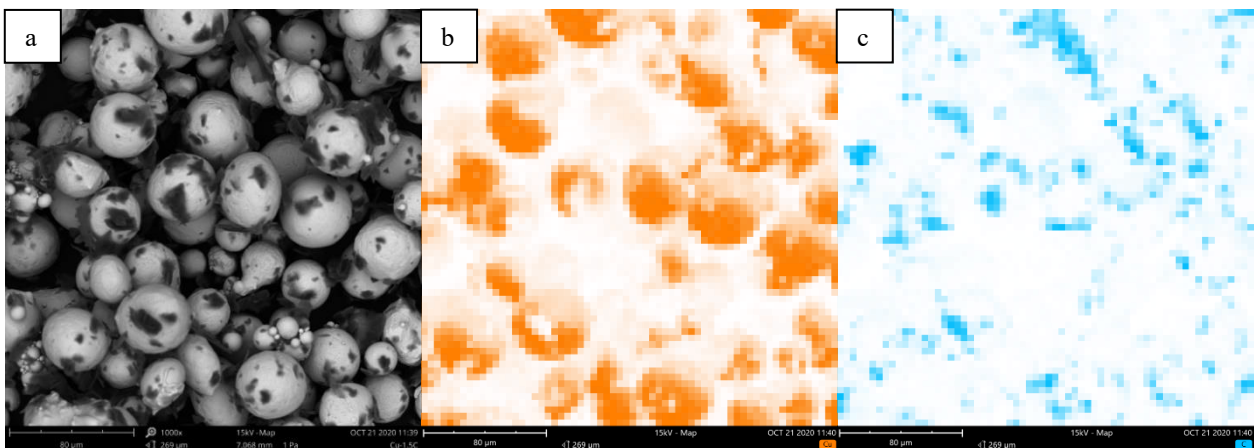


Figure 55 - a) SEM images of Cu – 1.5% C at 1000x. b) Cu in the mixture. c) C in the mixture.

## Cu – 2.0% C

Finally, Cu – 2% C is analyzed. As it was predictable, the major addition of carbon has produced many agglomerates around the copper particles.

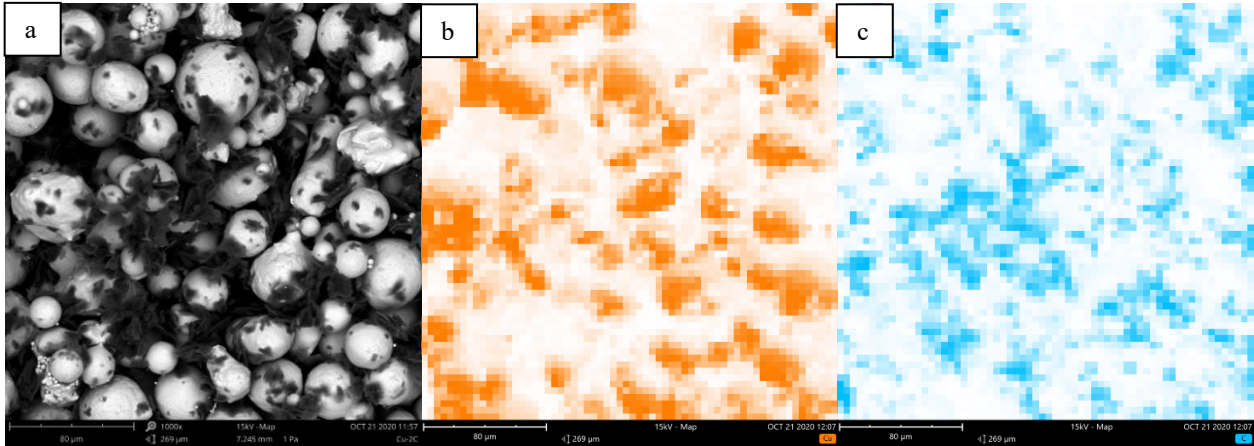


Figure 56 - a) SEM images of Cu – 2.0% C at 1000x. b) Cu in the mixture. c) C in the mixture.

From the study conducted, the best mixture has a value of graphite between 0.5% and 1% in weight. With these parameters, the graphite is able to cover copper particles without forming agglomerates. By increasing the amount of graphite, no further improvements are obtained in the covering of particles, and the flakes are not able to distribute in a homogeneous way. Also, the dimension of the flakes plays a significant role in their distribution: by using milled graphite, the particles of copper result more covered, and no agglomerations are visible.

### 3.2. Processability trials

As already presented in the chapter on Materials and methods, a series of jobs have been carried out in order to evaluate the effect of graphite addition on the processability of pure copper. There trials in the following chapter will be referred to as:

- JOB 1 pure Cu
- JOB 2 Cu – 2 wt.% C
- JOB 3 Cu – 1 wt.% C
- JOB 4 Cu – 0.5 wt.% milled C

#### JOB 1

The first job conducted was to print pure copper in order to evaluate its spreadability and processability. The powder has been previously sieved at 40 μm: the particles with a dimension bigger than 40 μm are rejected. The process of sieving consists of subdividing in different size distributions the powder using vibratory ultrasonic-assisted stainless-steel sieves.

A total of 9 samples with x-y dimensions of 10 mm x 10 mm are printed over a stainless-steel base plate.

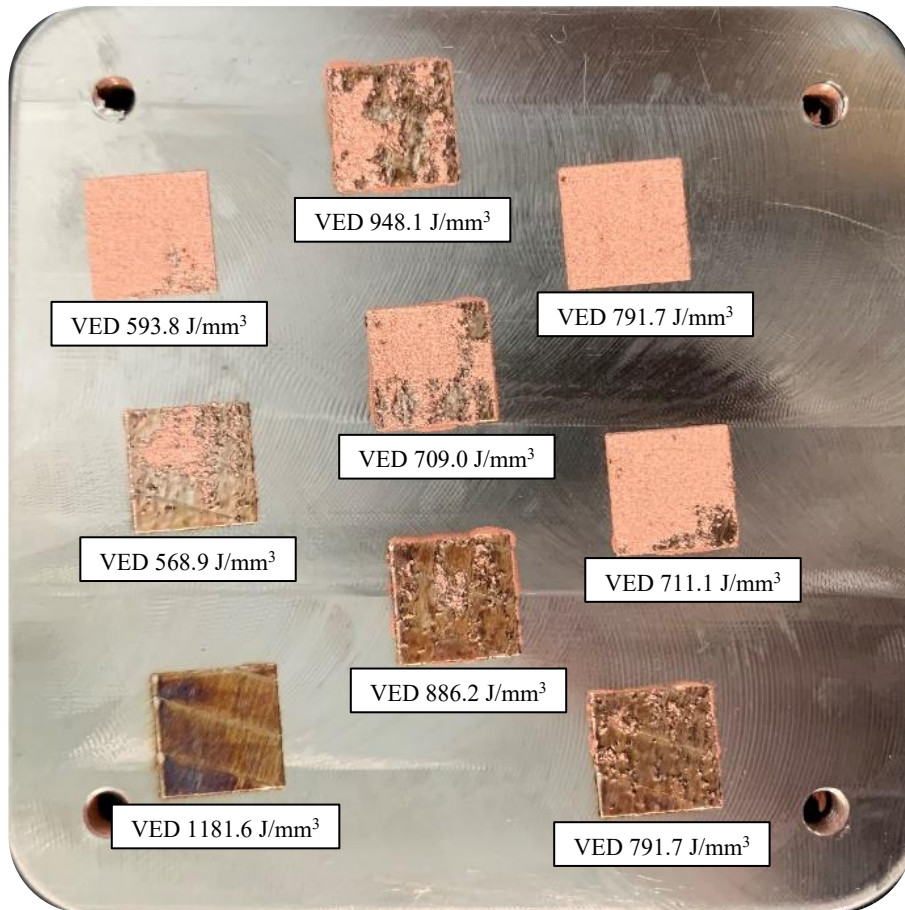


Figure 57 – Job 1. As-built pure Cu samples using powder finer than 40  $\mu\text{m}$ .

The process parameters selected for this first job are reported in Table 2. The laser power is set at the maximum value (95 W) for all the specimens, and the layer thickness is constant at 0.02 mm. Instead, the scanning speed and the hatching distance range respectively between 134 – 300 mm/s and 0.02 – 0.05 mm.

The VED was calculated for each sample as in Equation (2). Its values are reported as well in Table 2 and used in Figure 58 to make a comparison between samples.

Table 2 – Process parameters used in Job 1

Sample	$P$ [W]	$SS$ [mm/s]	$Hd$ [mm]	$Lt$ [mm]	$VED$ [ $\text{J}/\text{mm}^3$ ]
1	95	200	0.04	0.02	593.8
2	95	167	0.03	0.02	948.1
3	95	200	0.03	0.02	791.7
4	95	167	0.05	0.02	568.9
5	95	134	0.05	0.02	709.0
6	95	167	0.04	0.02	711.1
7	95	134	0.03	0.02	1181.6
8	95	134	0.04	0.02	886.2
9	95	300	0.02	0.02	791.7

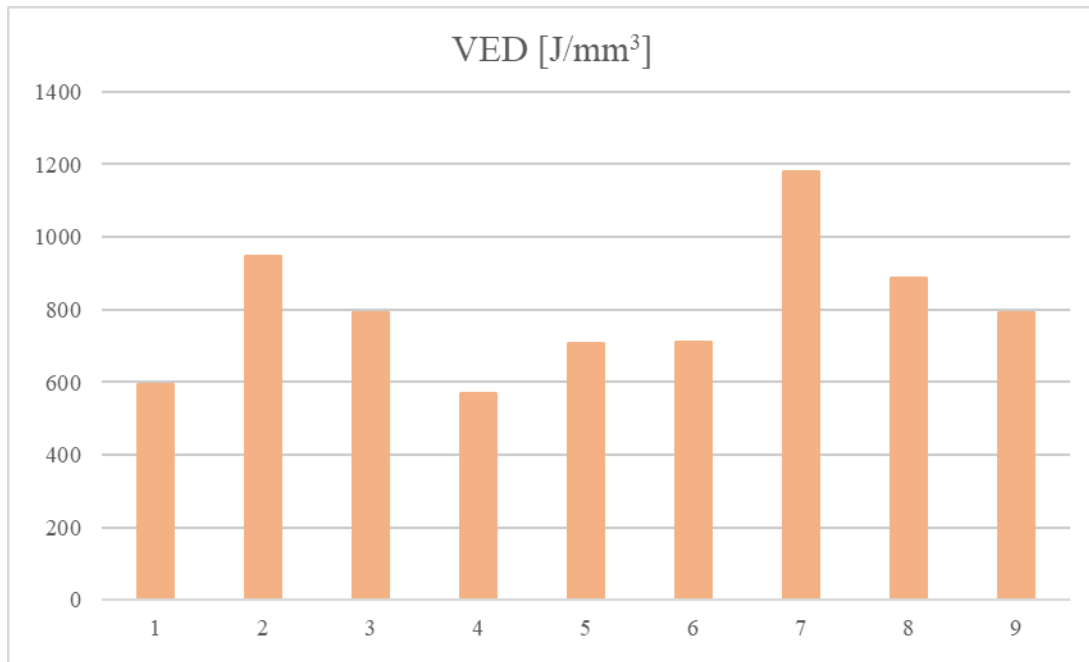


Figure 58 – VED of the samples for the first job

The printing of the samples was interrupted after only 10 layers due to the poor laser absorption and, as a consequence, lack of melting of the material. As a matter of fact, most of the powder is not melted due to its low laser absorption. Only with a VED close to  $1200 \frac{J}{mm^3}$  (sample 7) it is possible to obtain a full solidification of pure copper.

The printed samples, once removed from the machine, have been analyzed at the stereomicroscope. The samples produced respectively, with the lowest, the medium and the highest VED, are reported in Figure 59. The whole set of samples is, instead reported in the Appendix of the present thesis. Three images have been taken at different magnifications for each specimen: 1x, 2x, and 4x.

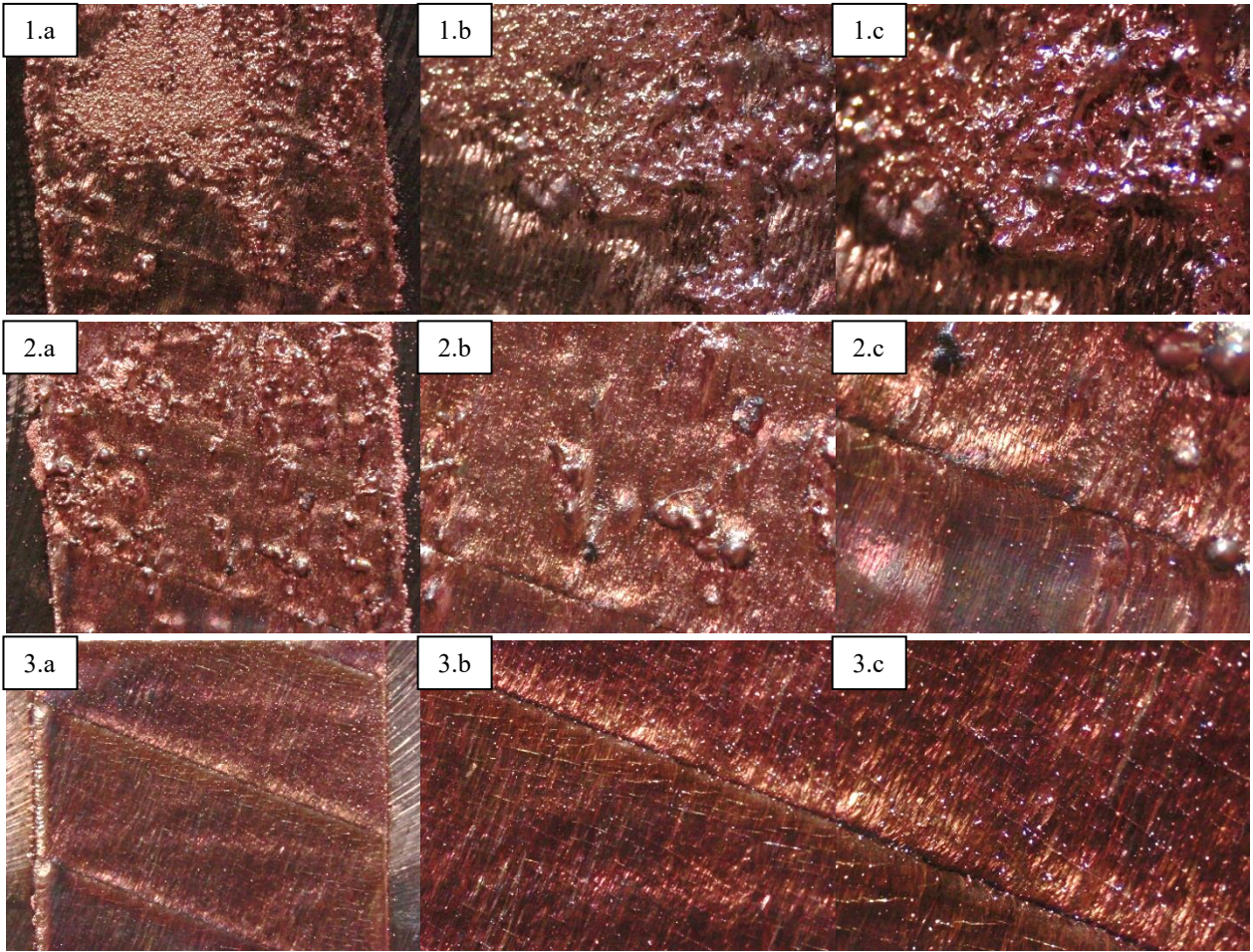


Figure 59 – Job 1. 1) Lowest VED (4), 2) Medium VED (9), 3) Highest VED (7). a) magnification at 1x, b) magnification at 2x, c) magnification at 4x

## JOB 2 – Cu- 2wt.%C

In order to solve the issue presented by the high reflectivity of copper, the material solution proposed is adopted in the second job. The idea is to try to enhance as much as possible the laser absorptivity of copper with a major addition of graphite. For this reason, as a first test, the powder used to run this job is the mixture of Cu – 2 wt.% C (

Figure 60).

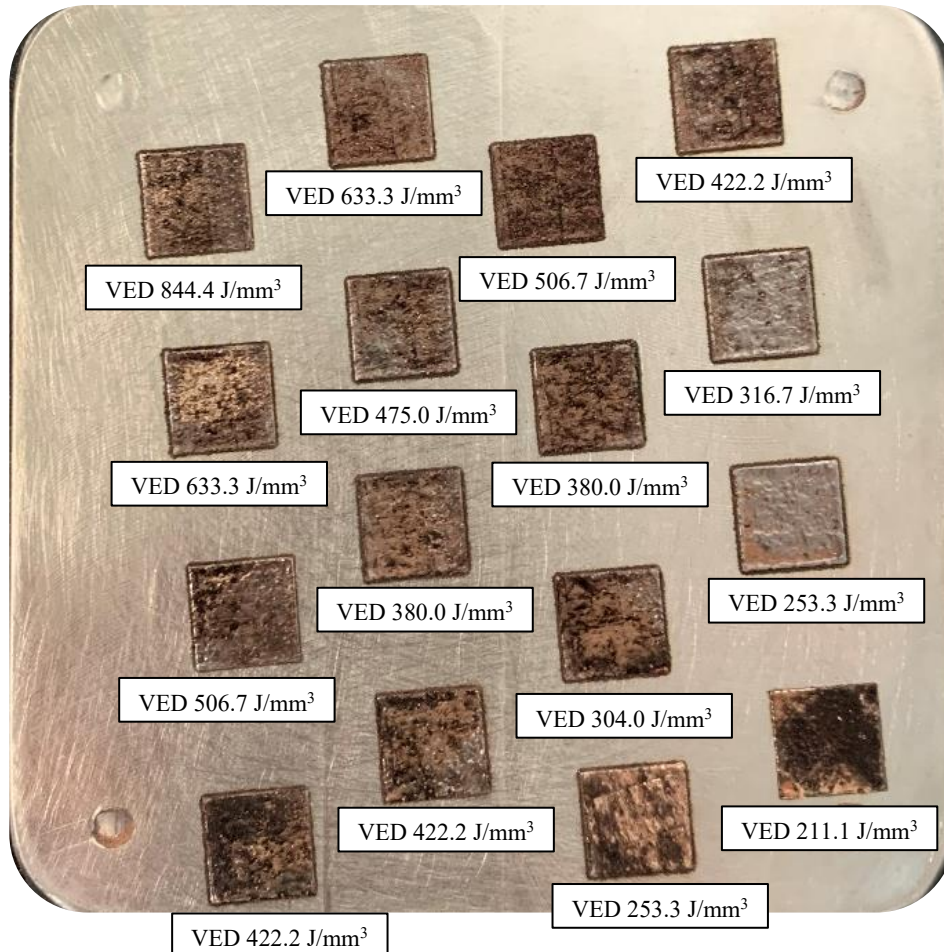


Figure 60 – Job 2. Cu – 2 wt. % C

The parameters used in the job are those reported in Table 3. The laser power output is set at the maximum available in Concept Mlab cusing (95 W). Another parameter that is kept constant for all the specimens is the layer thickness, which is set at 0.025 mm. The scanning speed ranges from 150 to 300 mm/s. The hatching distance ranges from 0.03 to 0.06 mm. The volumetric energy density ranges from a maximum value of  $844.4 \frac{J}{mm^3}$  to a minimum of  $211.1 \frac{J}{mm^3}$ .

Table 3 – Process parameters used in Job 2.

Sample	$P$ [W]	$SS$ [mm/s]	$Hd$ [mm]	$Lt$ [mm]	$VED$ [J/mm <sup>3</sup> ]
1	95	150	0.03	0.025	844.4
2	95	150	0.04	0.025	633.3
3	95	150	0.05	0.025	506.7
4	95	150	0.06	0.025	422.2
5	95	200	0.03	0.025	633.3
6	95	200	0.04	0.025	475.0
7	95	200	0.05	0.025	380.0
8	95	200	0.06	0.025	316.7
9	95	250	0.03	0.025	506.7
10	95	250	0.04	0.025	380.0
11	95	250	0.05	0.025	304.0
12	95	250	0.06	0.025	253.3
13	95	300	0.03	0.025	422.2
14	95	300	0.04	0.025	316.7
15	95	300	0.05	0.025	253.3
16	95	300	0.06	0.025	211.1

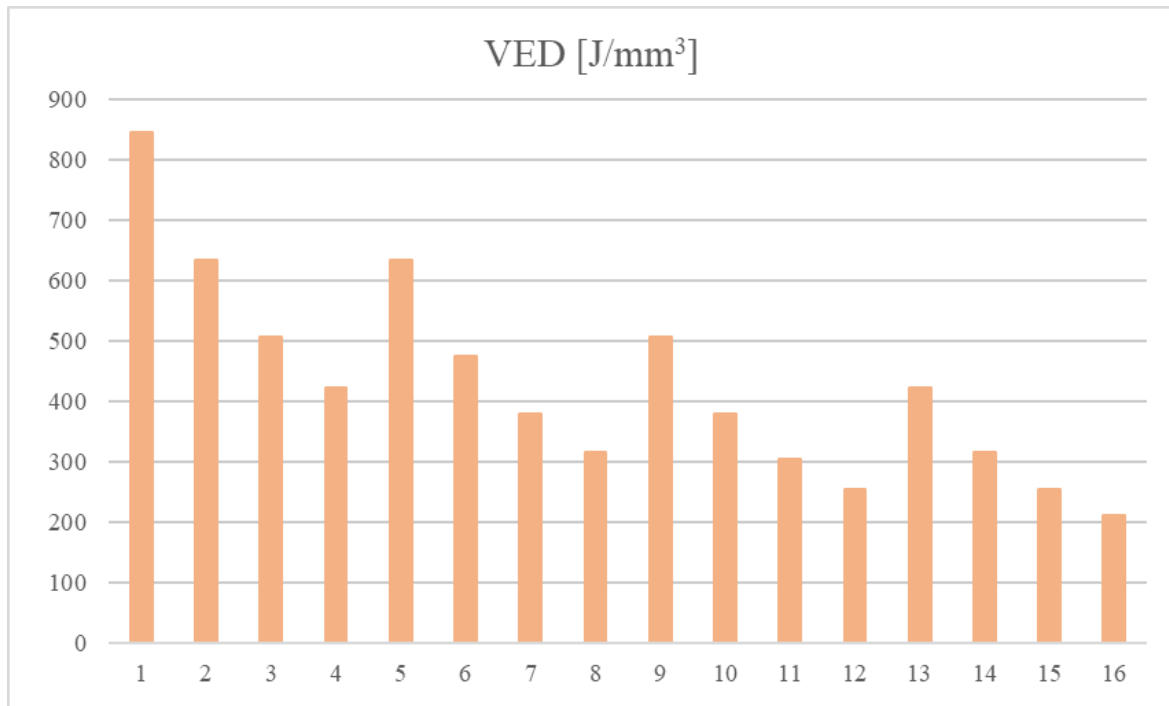


Figure 61 – VED of the samples for the second job

Even in this case, the job was not completed and was interrupted after only 10 layers, due to the presence of smoke produced by the agglomerations of graphite during the process. From the characterization previously conducted, in fact, it was clear that graphite was not uniformly distributed among the powder. The agglomerations are evident in the surface of the specimens.

Certainly, anyway, the addition of graphite has ensured the possibility of achieving a higher level of melting of copper, suggesting that the proposed material solution can be successful. Also, for this job the samples produced with the lowest, medium and highest VED are reported below in Figure 62, while the entire set of specimens is presented in the Appendix.

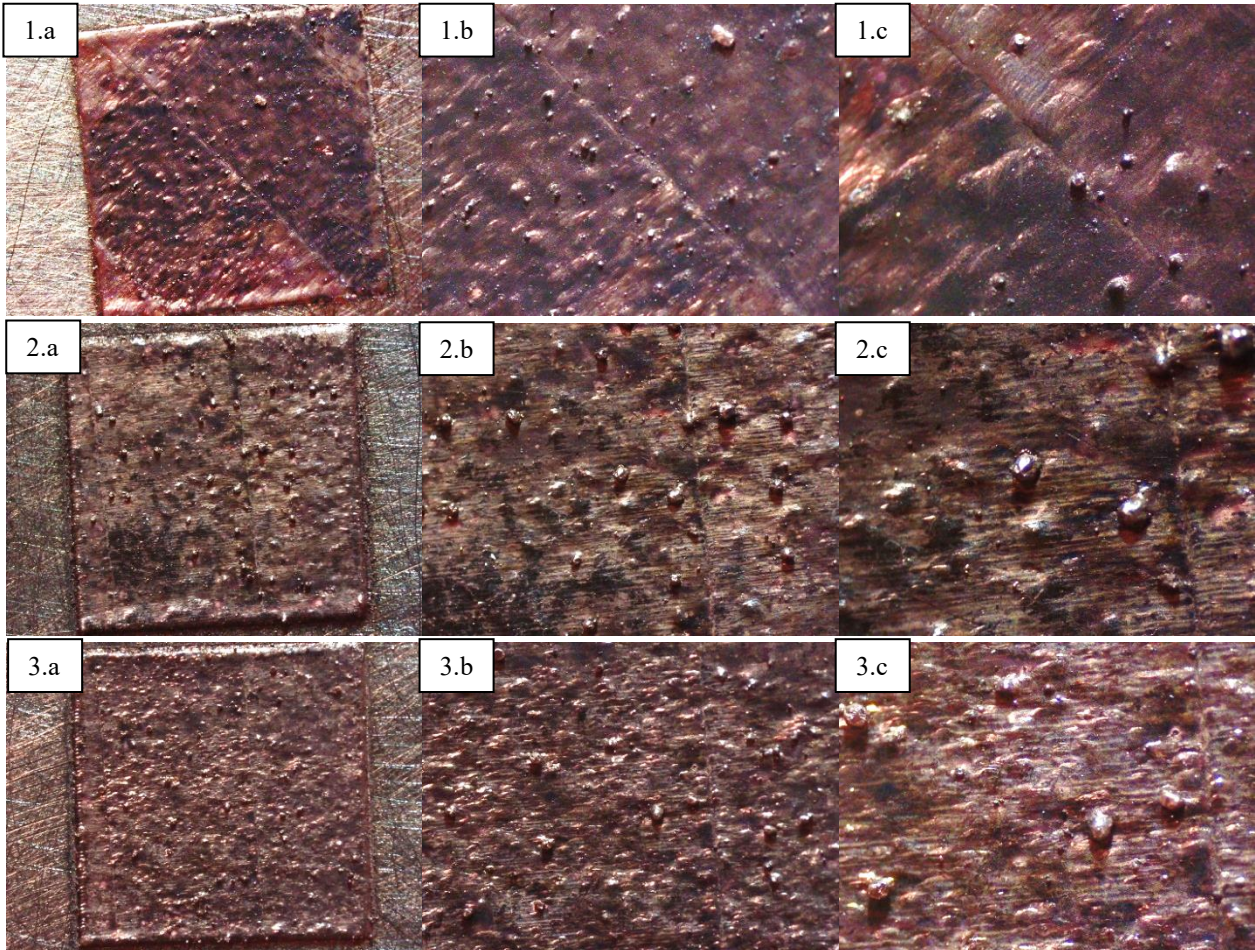


Figure 62 – Job 2. 1) Lowest VED (16), 2) Medium VED (6), 3) Highest VED (1). a) magnification at 1x, b) magnification at 2x, c) magnification at 4x

### JOB 3- Cu-1 wt.%C

As a consequence of the result of the second job, it was decided to print copper with a reduced amount of graphite: eight samples of Cu – 1 wt.% C have been printed.



Figure 63 – Job 3. Cu – 1 wt.% C.

The process parameters adopted for this job are reported in Table 4. The laser power is kept constant at the maximum value, while the layer thickness is slightly reduced with respect to the previous job from 0.025 mm to 0.02 mm. This modification aims at guaranteeing the correct adhesion between the printed layer and the previous one. The scanning speed and the hatching distance vary in order to reach higher levels of VED, with respect to the previous job, considering that a value lower than  $500 \frac{J}{mm^3}$  couldn't ensure the complete melting of the powder.

Table 4 – Process parameters used in Job 3

Sample	$P$ [W]	$SS$ [mm/s]	$Hd$ [mm]	$Lt$ [mm]	$VED$ [J/mm <sup>3</sup> ]
1	95	200	0.04	0.02	593.8
2	95	167	0.03	0.02	948.1
3	95	200	0.03	0.02	791.7
4	95	167	0.05	0.02	568.9
5	95	134	0.05	0.02	709.0
6	95	167	0.04	0.02	711.1
7	95	134	0.03	0.02	1181.6
8	95	134	0.04	0.02	886.2

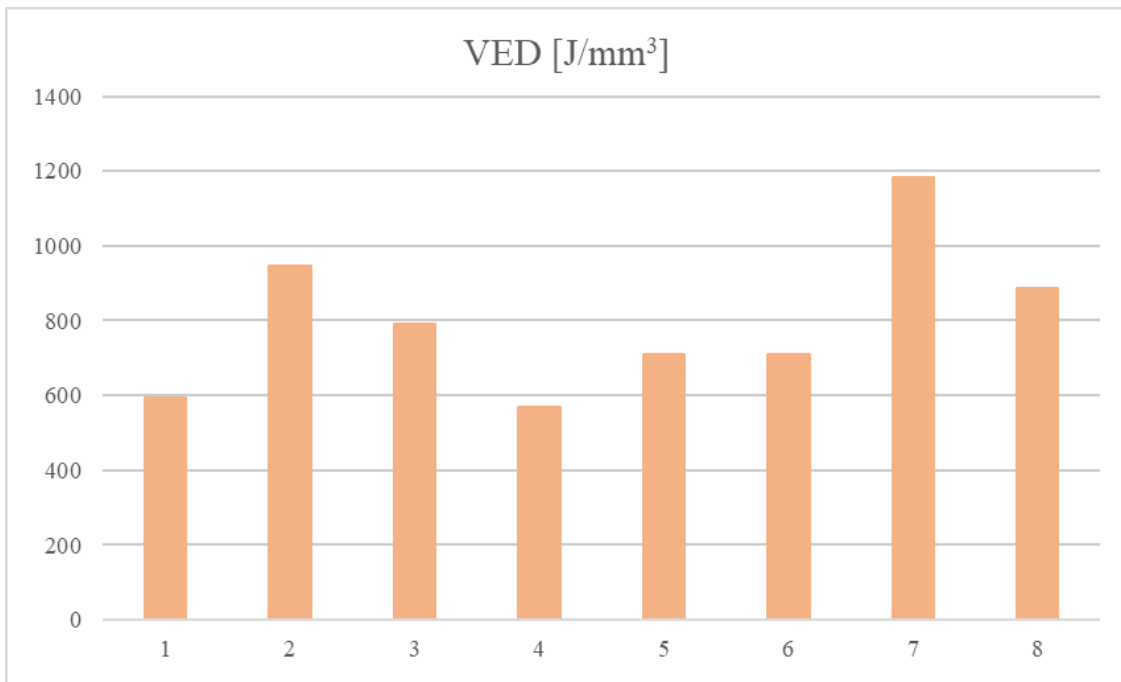


Figure 64 - VED of the samples for the third job

An improvement in flowability is evident from this job. Anyway, in this case, it was not possible to have a full component, and the job was interrupted after ten layers due to the high presence of smoke generated by the graphite. This suggests that reducing the quantity of graphite flakes was insufficient, leading to a further reduction in the next experiment.

In Figure 65, the most interesting results are reported: the samples printed with the lowest, medium, and highest VED.

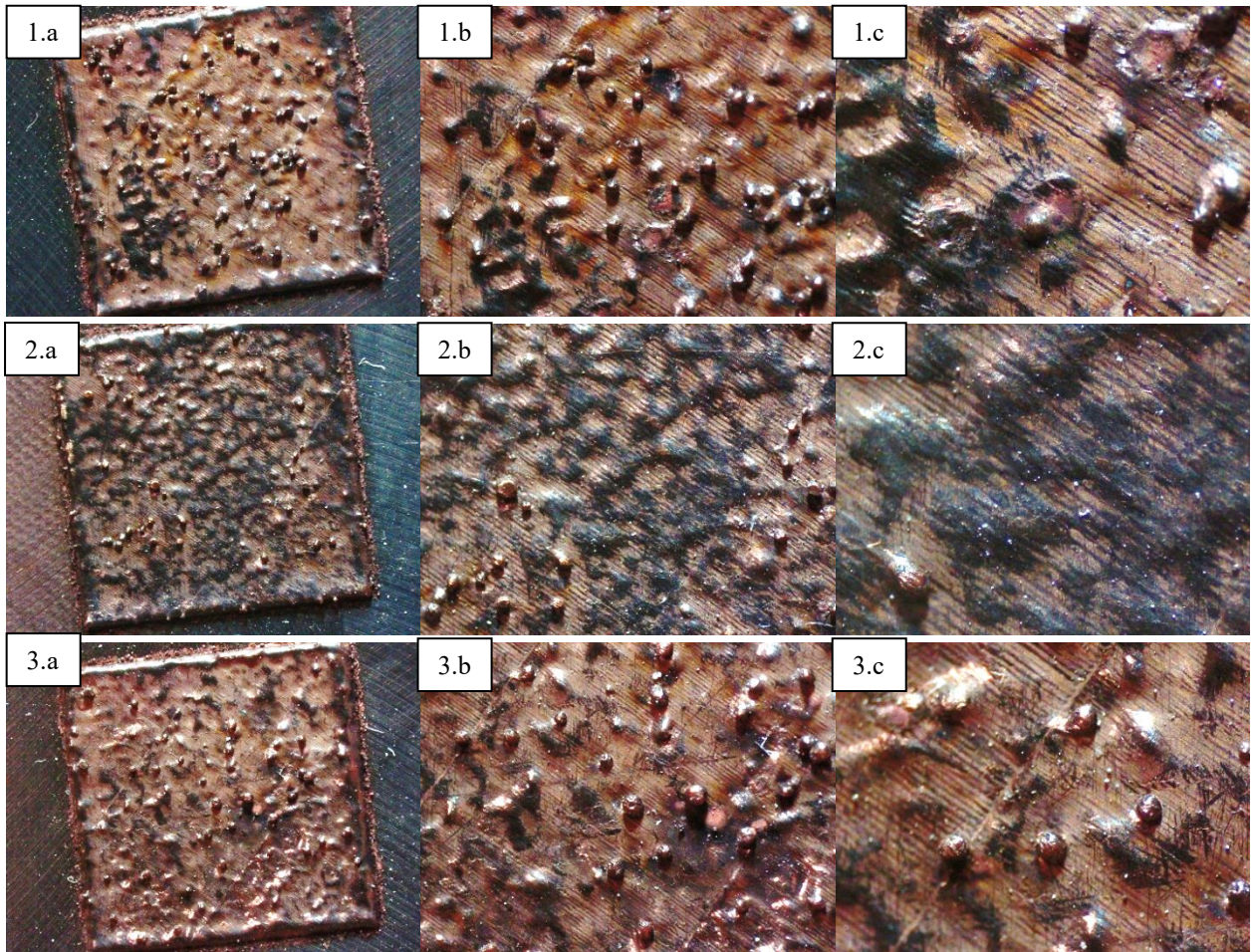


Figure 65 – Job 3. 1) Lowest VED (4), 2) Medium VED (3), 3) Highest VED (7). a) magnification at 1x, b) magnification at 2x, c) magnification at 4x

## JOB 4

As the last attempt to print the cubic specimens of copper through the LPBF process, the mixture of Cu – 0.5 wt.% milled C was used. As already explained in the description of the characterization of materials, the goal of using milled graphite is to enable a better coverage of copper particles. In this way, it should be possible to improve the laser absorptivity of the powder significantly. Moreover, with the use of milled graphite in place of graphite flakes, we would reduce the size of the mixture's particles to obtain the thinner layer of the component with better packing density. Of course, we have also reduced the graphite content aiming to improve the overall flowability of the mixture.



Figure 66 – Job 4. Cu – 0.5 wt.% milled C

The set of process parameters adopted for this job is the same in printing pure copper (Job 1). In total nine samples have been prepared, but the number 9 was aborted after a few layers due to excessive production of smoke. The printing of the remaining eight samples was stopped after the realization of 2.28 mm owing to the formation of several balls over the surface.

Despite the interruption of the manufacturing, it was possible to see a significant improvement in the flowability of the powder, thanks to the reduction in size and content of graphite. This suggests that this final mixture is the most interesting so far.

However, the laser power of the Concept Laser MLabR is not high enough to melt the powder completely and so produce a dense layer: a power of 95 W can just sinter the particles.

As for the previous jobs, the most interesting images are shown in Figure 67, while the whole set of images collected at the stereomicroscope are reported in the Appendix.

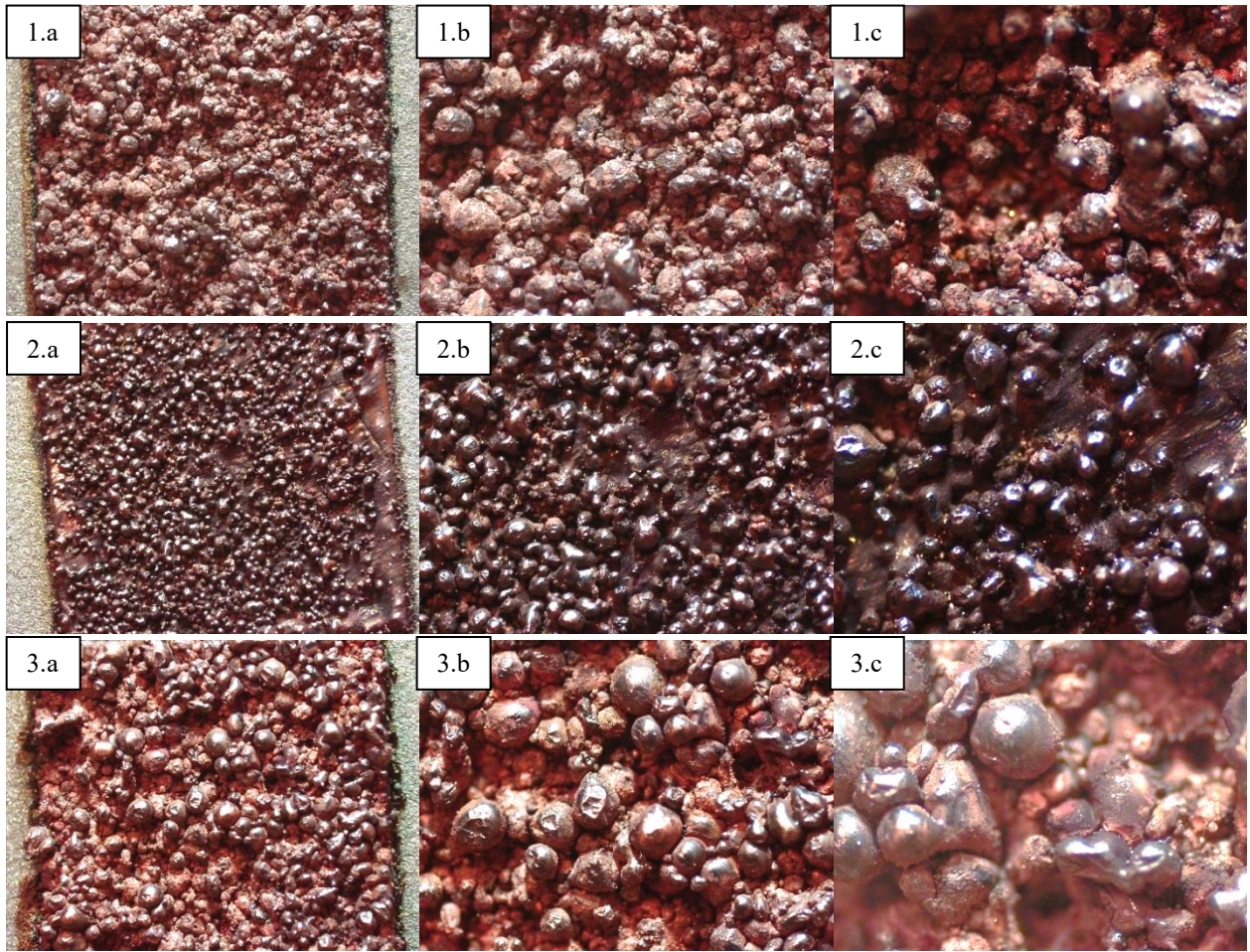


Figure 67 – Job 4. 1) Lowest VED (4), 2) Medium VED (9), 3) Highest VED (7). a) magnification at 1x, b) magnification at 2x, c) magnification at 4x

## SSTs

The results collected from the SSTs analysis are reported in the present chapter.

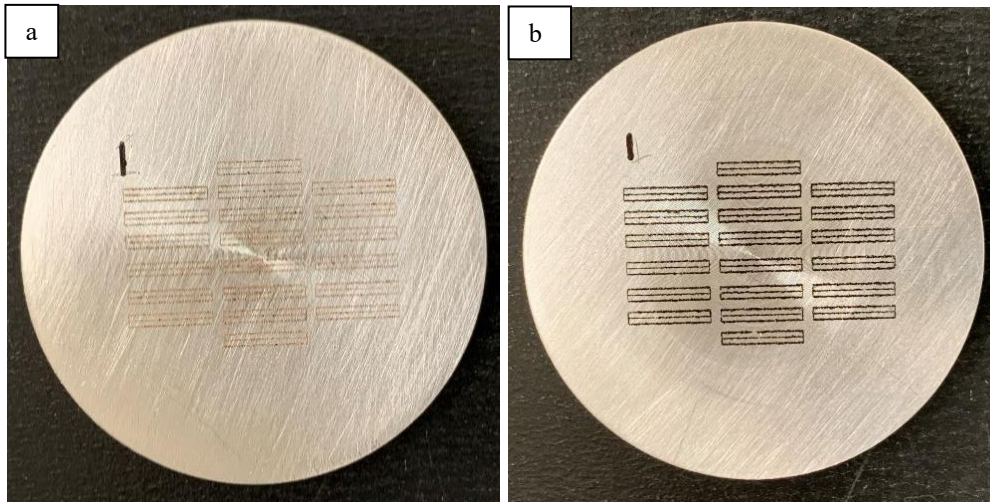


Figure 68 – SSTs printed over Al discs. a) Pure copper. b) Cu – 0.5% milled C.

The SSTs building parameters used for both powders are reported in Table 5. Laser power ranges from 85 to 90 W, scanning speed from 100 to 250 mm/s, while the layer thickness is fixed at 0.02 mm. For each sample, the value of LED was calculated using Equation (3) and used in Figure 69 to compare them.

Table 5 – Process parameters used for the SSTs of pure Cu and Cu – 0.5% milled C

Sample	$P$ [W]	$SS$ [mm/s]	$Lt$ [mm]	$LED$ [J/mm]
1	95	100	0.02	0.950
2	95	125	0.02	0.760
3	95	150	0.02	0.633
4	95	175	0.02	0.543
5	95	200	0.02	0.475
6	95	225	0.02	0.422
7	95	250	0.02	0.380
8	90	100	0.02	0.900
9	90	125	0.02	0.720
10	90	150	0.02	0.600
11	90	175	0.02	0.514
12	90	200	0.02	0.450
13	90	225	0.02	0.400
14	90	250	0.02	0.360
15	85	100	0.02	0.850
16	85	125	0.02	0.680
17	85	150	0.02	0.567
18	85	175	0.02	0.486
19	85	200	0.02	0.425
20	85	225	0.02	0.378

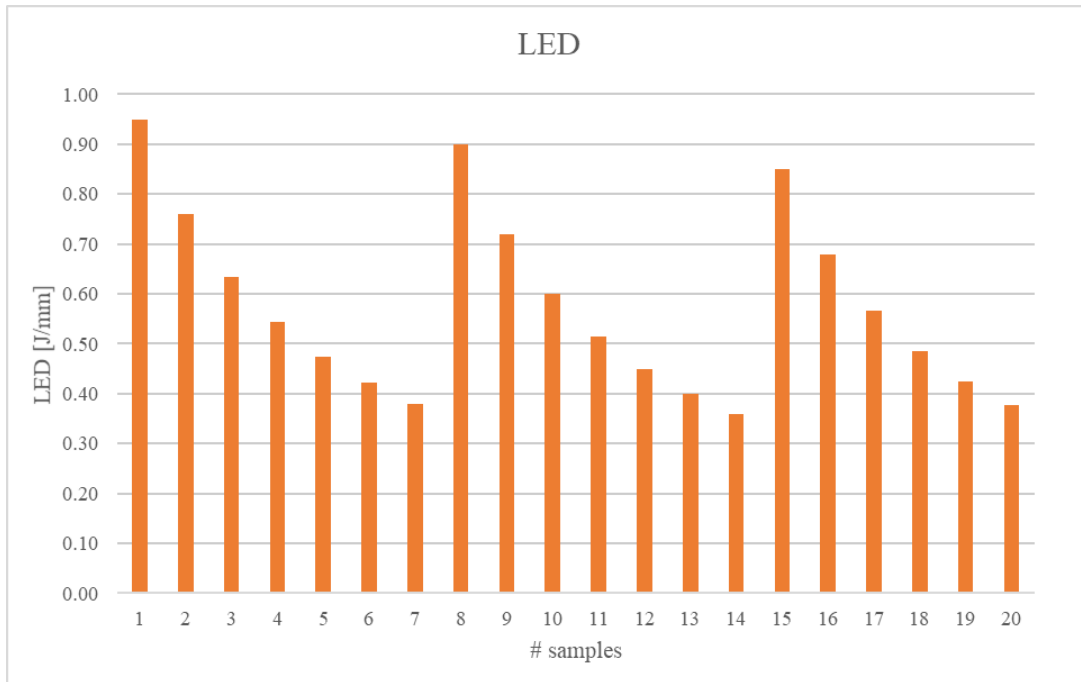


Figure 69 – LED of the SSTs

After testing all the SSTs, as described in the chapter on Materials and methods, it was possible to group them into four different categories: samples with not enough LED, melt pools with evident balling, thin and stable or irregular SSTs. In order to simplify understanding, a specific colour has been associated with each category. Representative examples are shown in Table 6. As Aversa et al. [74] explained, these geometries are usually related to the quantity of LED given. In the “Not enough LED” case, it was impossible to detect any scan track since the LED used was not sufficient to melt the powder. In the second case, balling behaviour prevails: the scan track is discontinuous, and the melt pool is characterized by poor wetting. The “Thin and stable” category is individuated in a narrow range of LEDs, where the SSTs resulted in a uniform melt pool. Finally, with higher LED values, the melt pools are strongly asymmetrical: these latter are defined as “Irregular”.

As a matter of fact, the categorization was not trivial since some samples presented an intermediate behaviour between two regions. Moreover, the melt pools did not always show a precise trend following the increase in LED; this is particularly true for the first set of SSTs where pure copper was processed.

In the next paragraphs, the results obtained for both sets of SSTs are reported, and the geometrical features of the melt pools are discussed.

Increasing LED

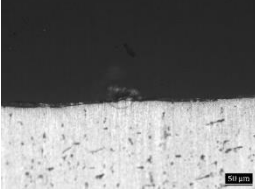
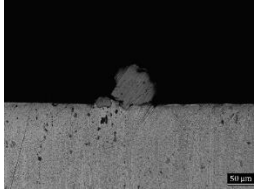
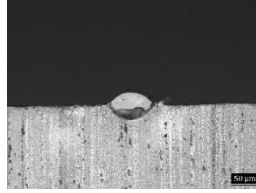
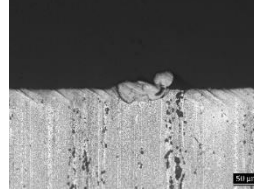
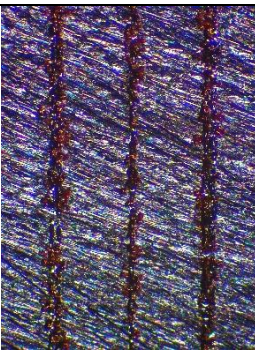
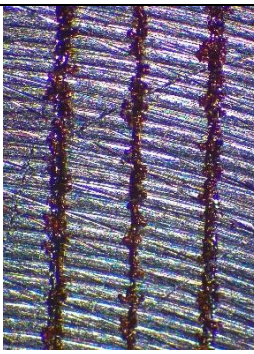
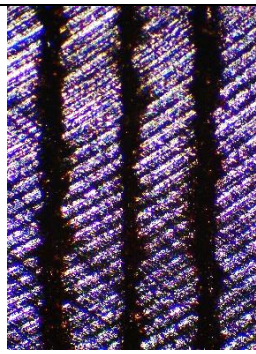
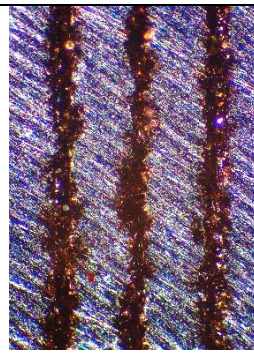
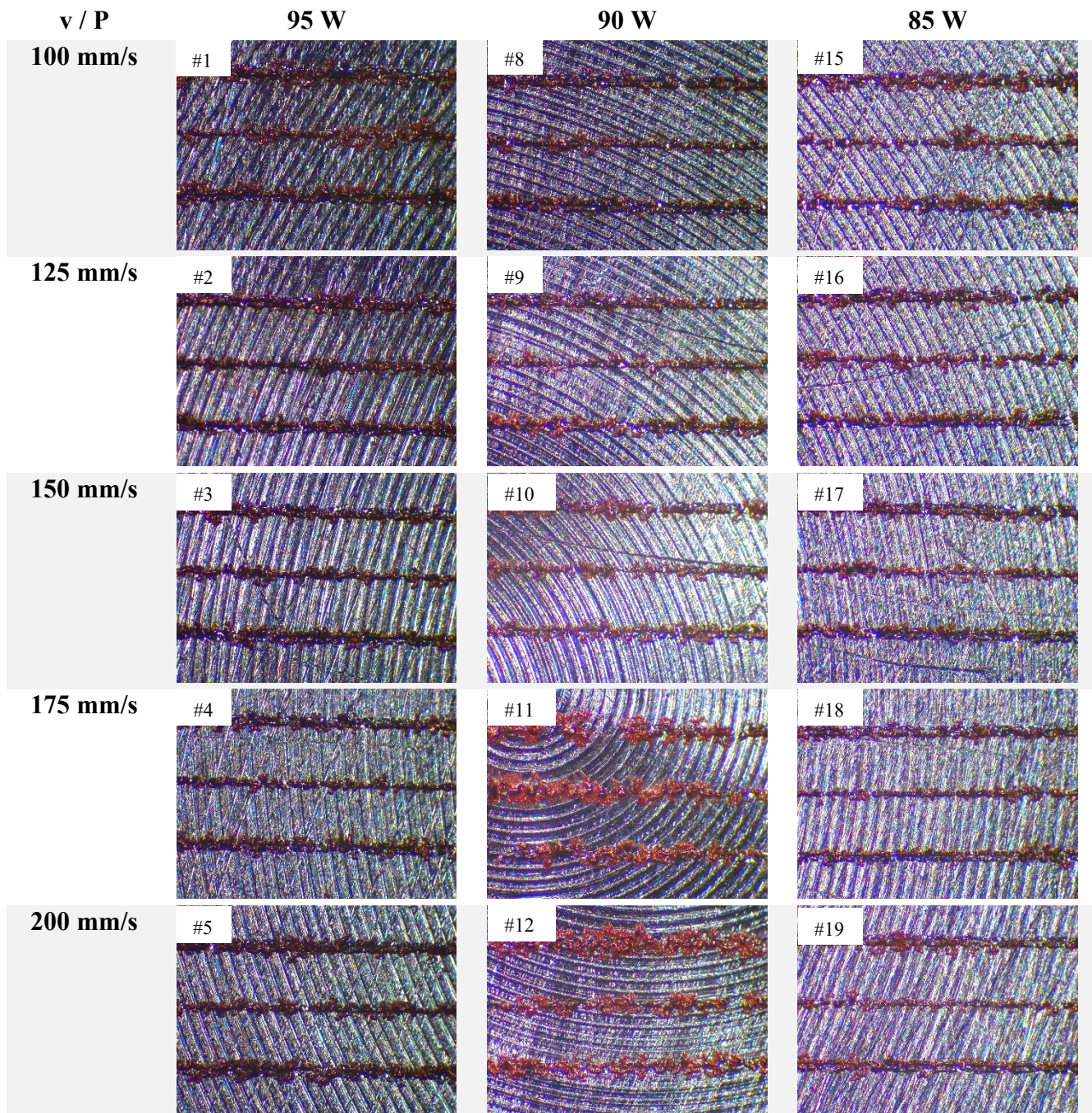
Cross section				
On top				
	Not enough LED 	Balling 	Thin and stable 	Irregular 

Table 6 – Examples of different melt pools: not enough LED, balling effect, thin and stable, irregular.

## Pure copper SSTs

The first SSTs tested were the ones made of pure Cu. The images collected for each scan track by the on top observation through stereomicroscope are reported in Table 7.



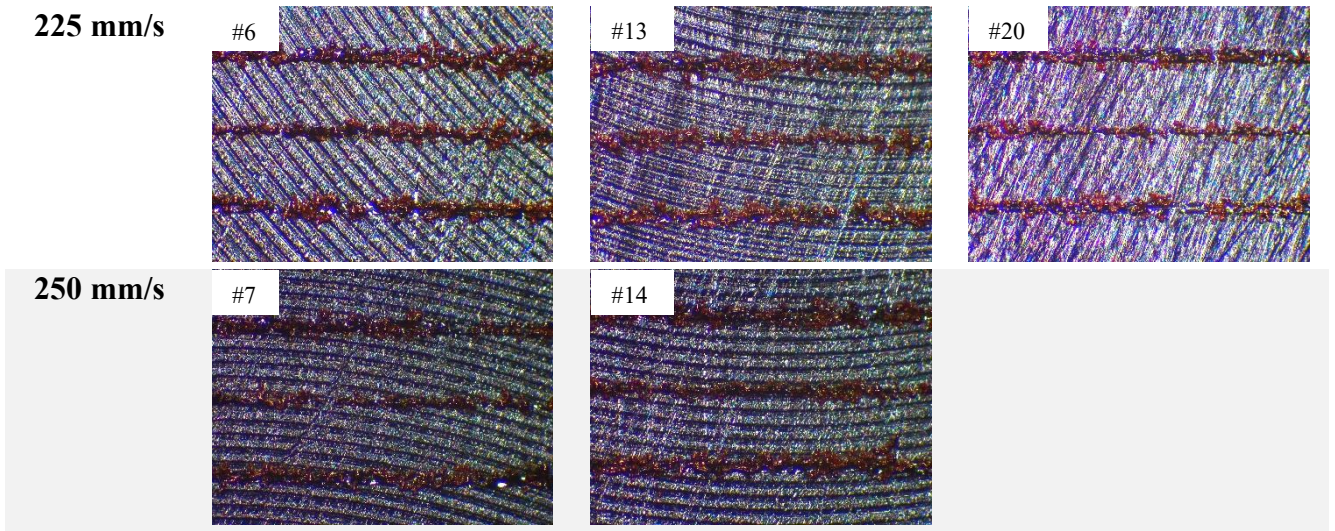
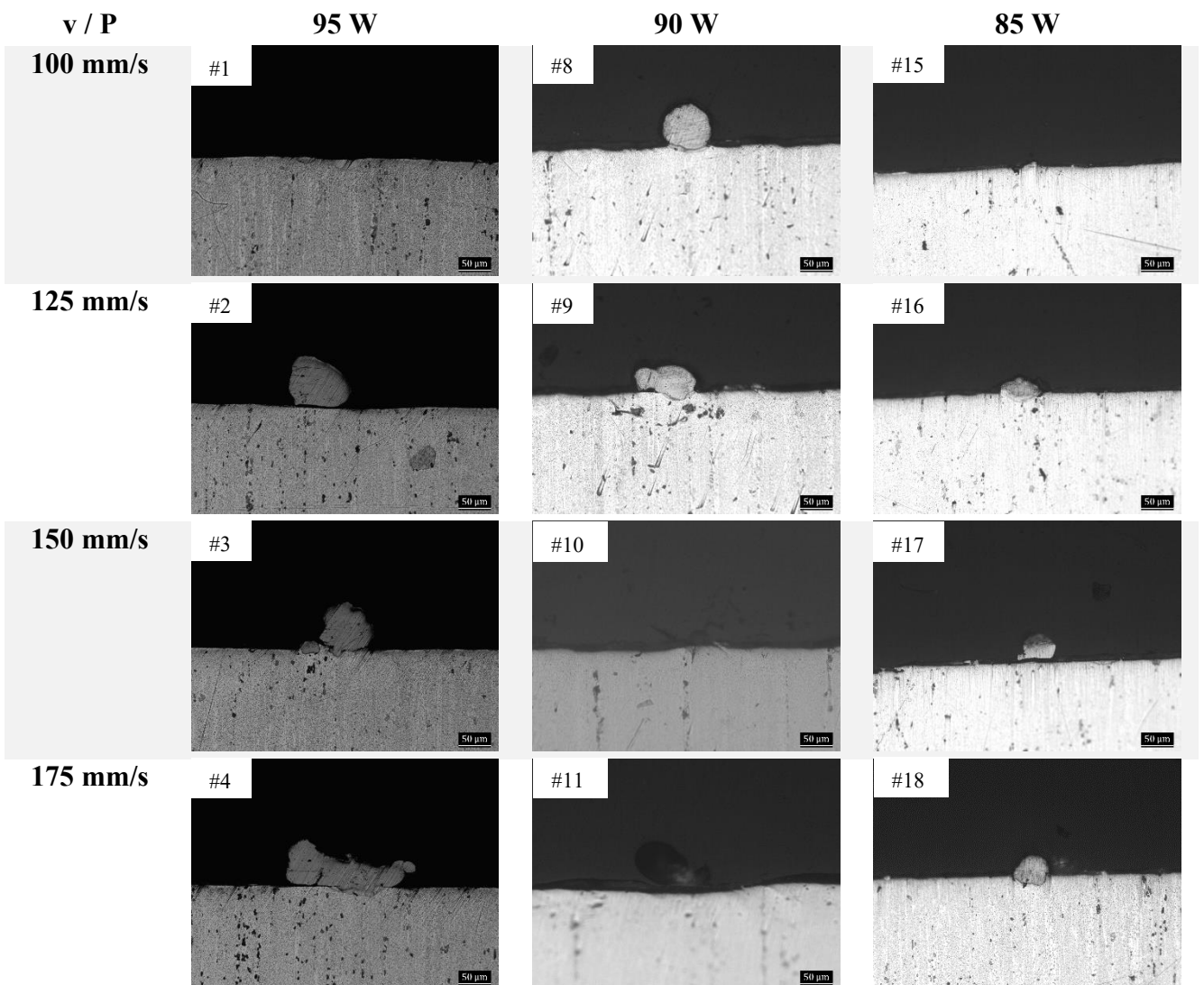


Table 7 – On top observation of pure Cu SSTs

Cross-sections observed at the optical microscope are presented in Table 8. In some cases, the melt pool is not detectable, suggesting that the LED was not sufficient to create a stable scan track.



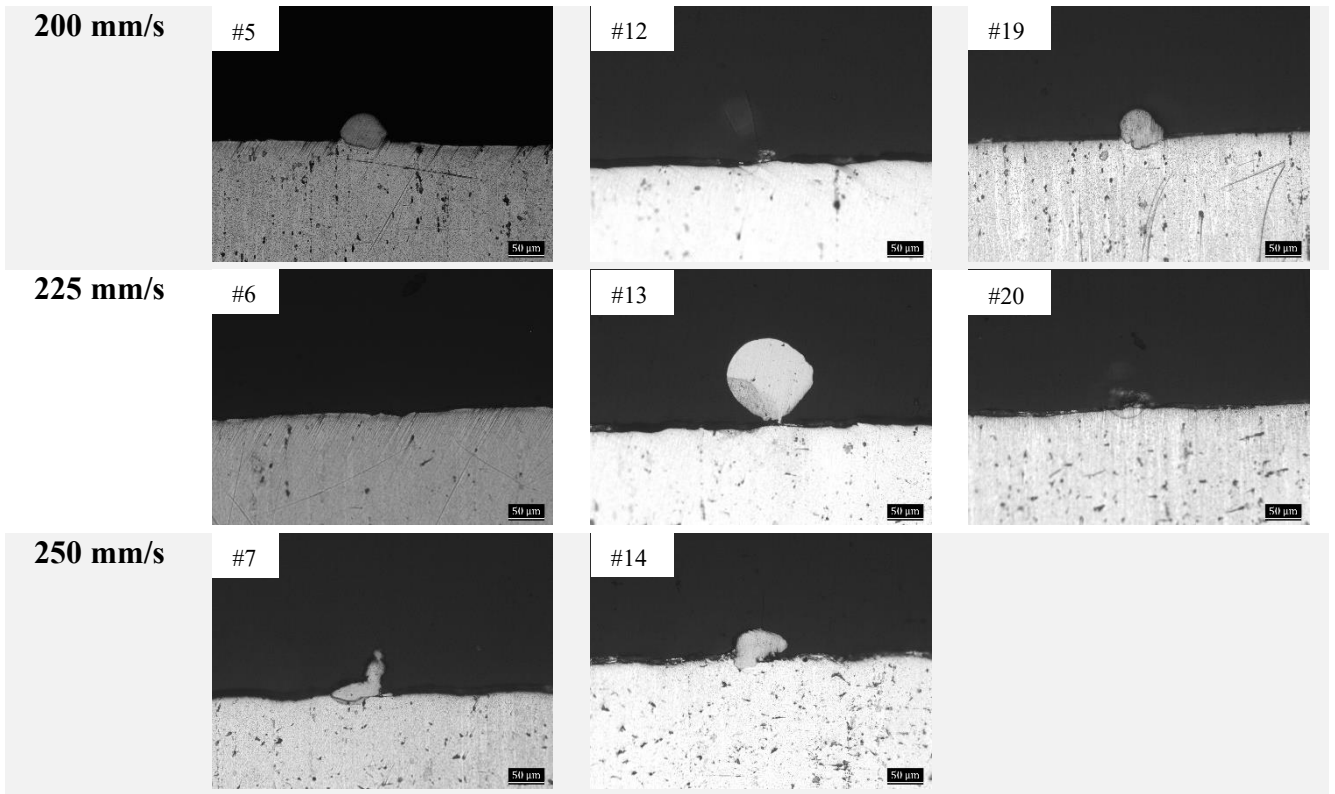


Table 8 – Cross section observation of pure Cu SSTs

From the stereo and optical images were taken it was possible to distinguish the four different morphologies of the melt pools, as described in Figure 70.

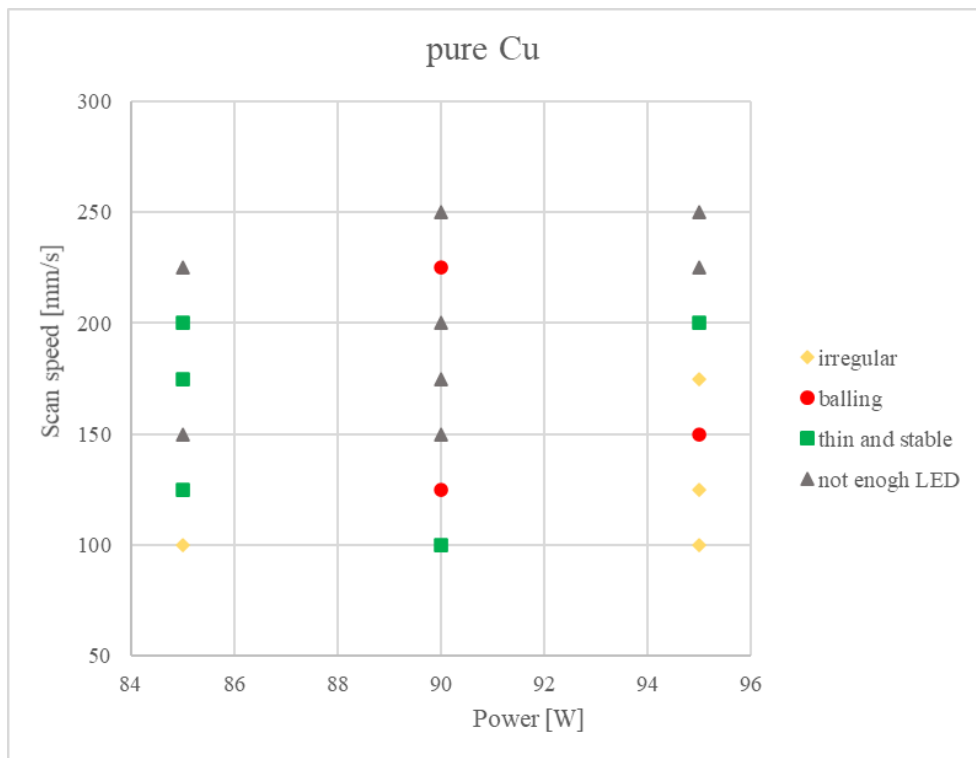


Figure 70 – Scan speed versus Power of the SSTs of pure Cu

The most interesting results have been obtained with a LED ranging between 0.4 and 0.5 J/mm, even though the melt pools are quite small, and the scan tracks just fairly continuous. The increment in LED starts to be detrimental when it exceeds the value of 0.7 J/mm. Anyway, the sample #8 presents an exception: the scan track is stable, and the melt pool is quite regular despite the LED of 0.9 J/mm.

The values of the geometrical features measured through ImageJ are plotted in the following diagrams in a logarithmic scale as a function of LED. First, the height of the melt pools is reported, subdivided in  $h_{up}$ ,  $h_{down}$  and  $H$ , indicating the height of the scan respectively over the base plate, its depth, and the sum of the two contributes, i.e. the total height. Secondly, the width,  $W$ , and the surface,  $A$ , of the melt pools are plotted. Finally, the values of the angles  $\alpha$  at the right and the left of the scans.

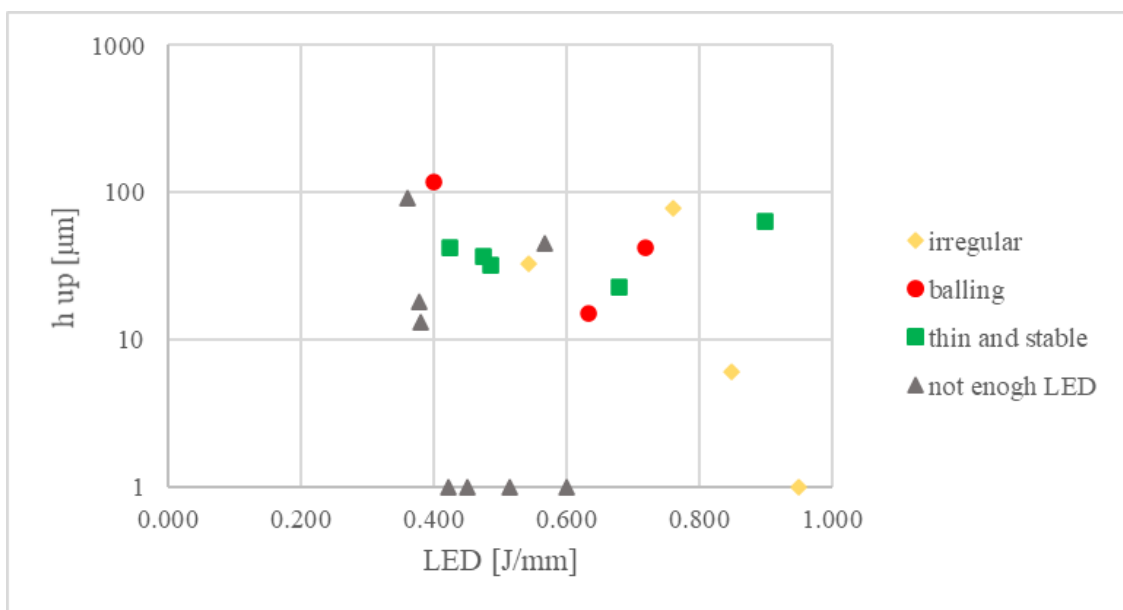


Figure 71 –  $h_{up}$  versus LED of the SSTs of pure Cu in logarithmic scale

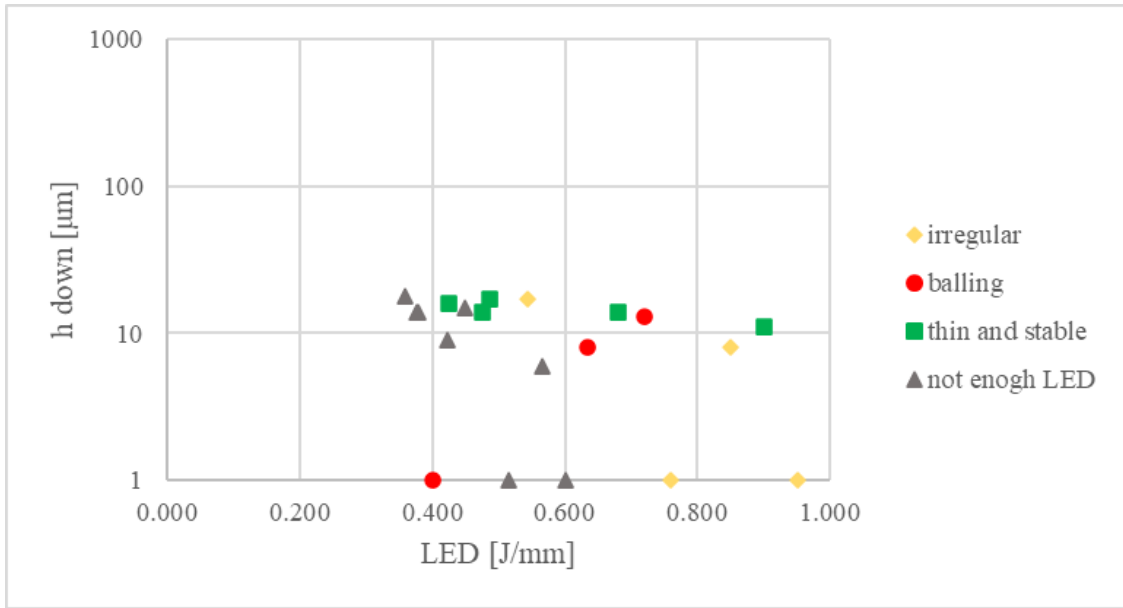


Figure 72 –  $h_{\text{down}}$  versus LED of the SSTs of pure Cu in logarithmic scale

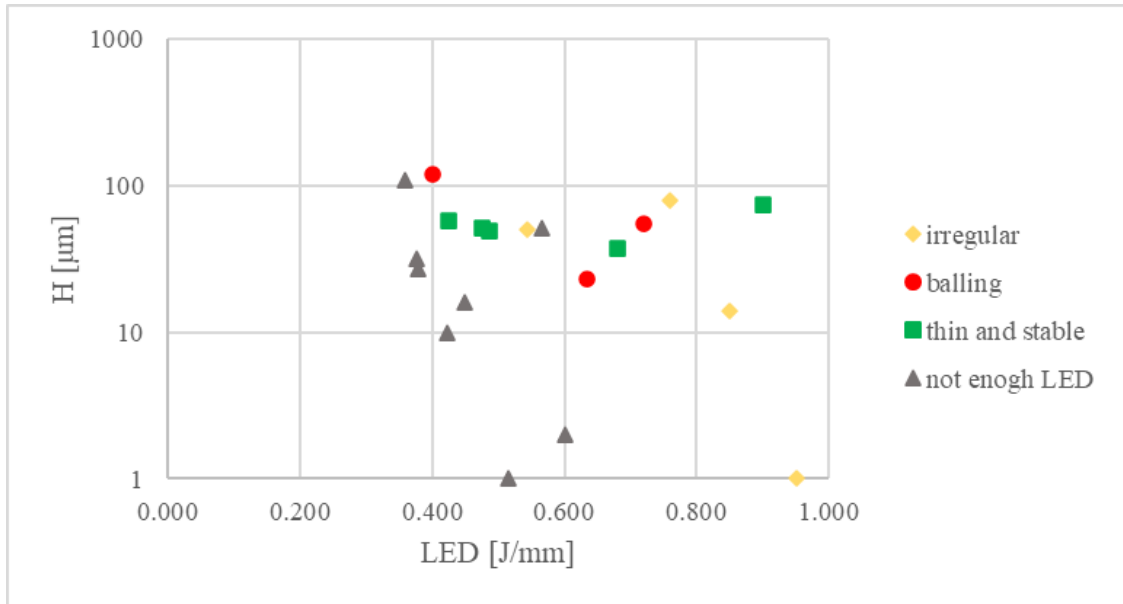


Figure 73 –  $H$  versus LED of the SSTs of pure Cu in logarithmic scale

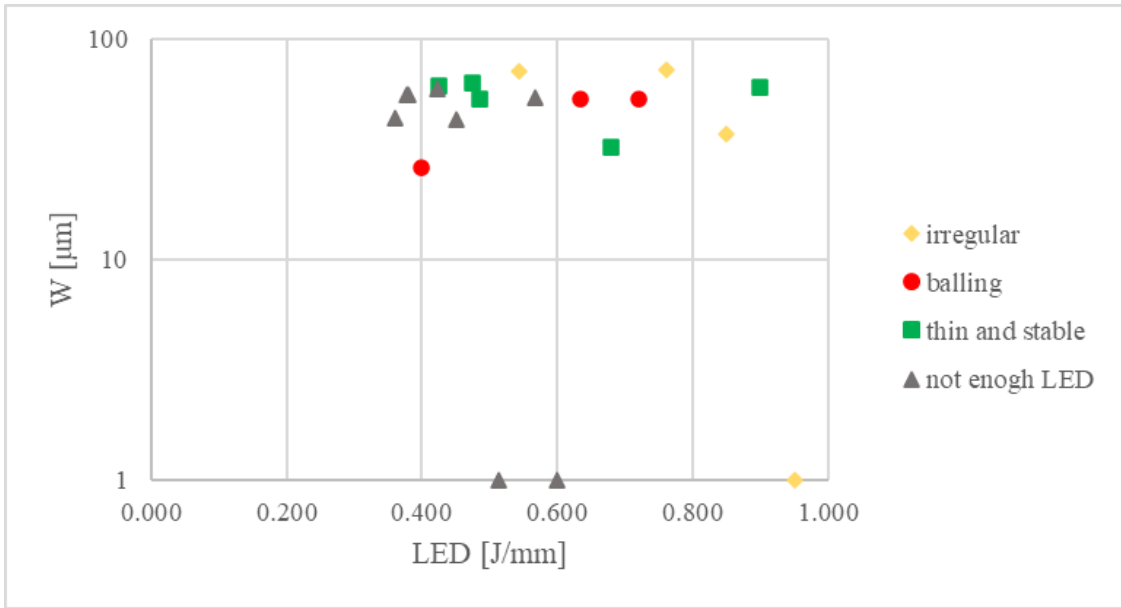


Figure 74 –  $W$  versus LED of the SSTs of pure Cu in logarithmic scale

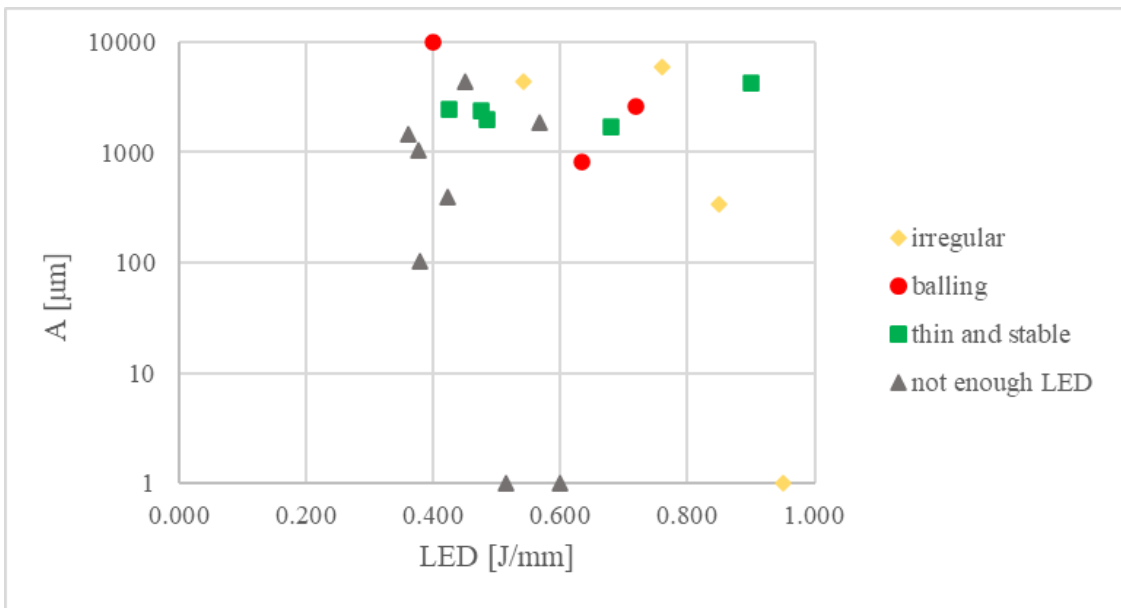


Figure 75 –  $A$  versus LED of the SSTs of pure Cu in logarithmic scale

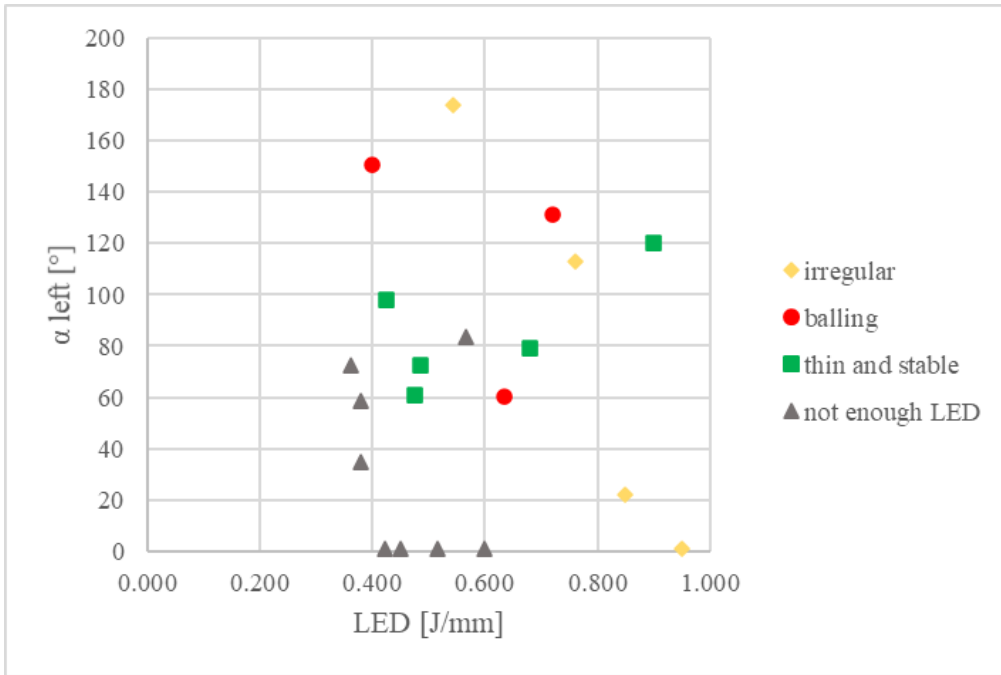


Figure 76 –  $\alpha_{left}$  versus LED of the SSTs of pure Cu in logarithmic scale

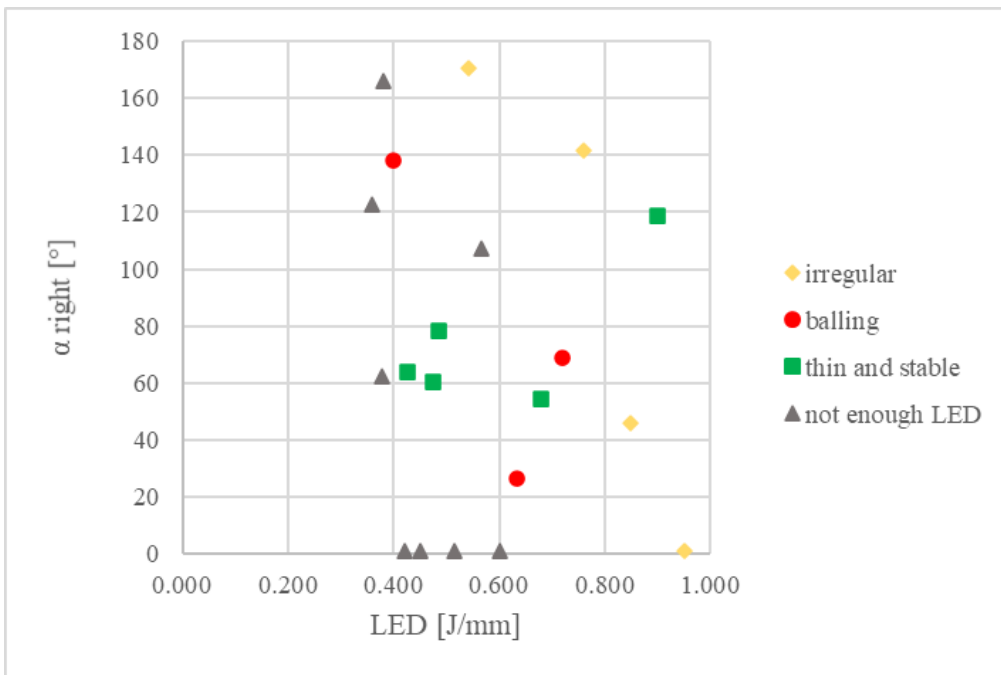
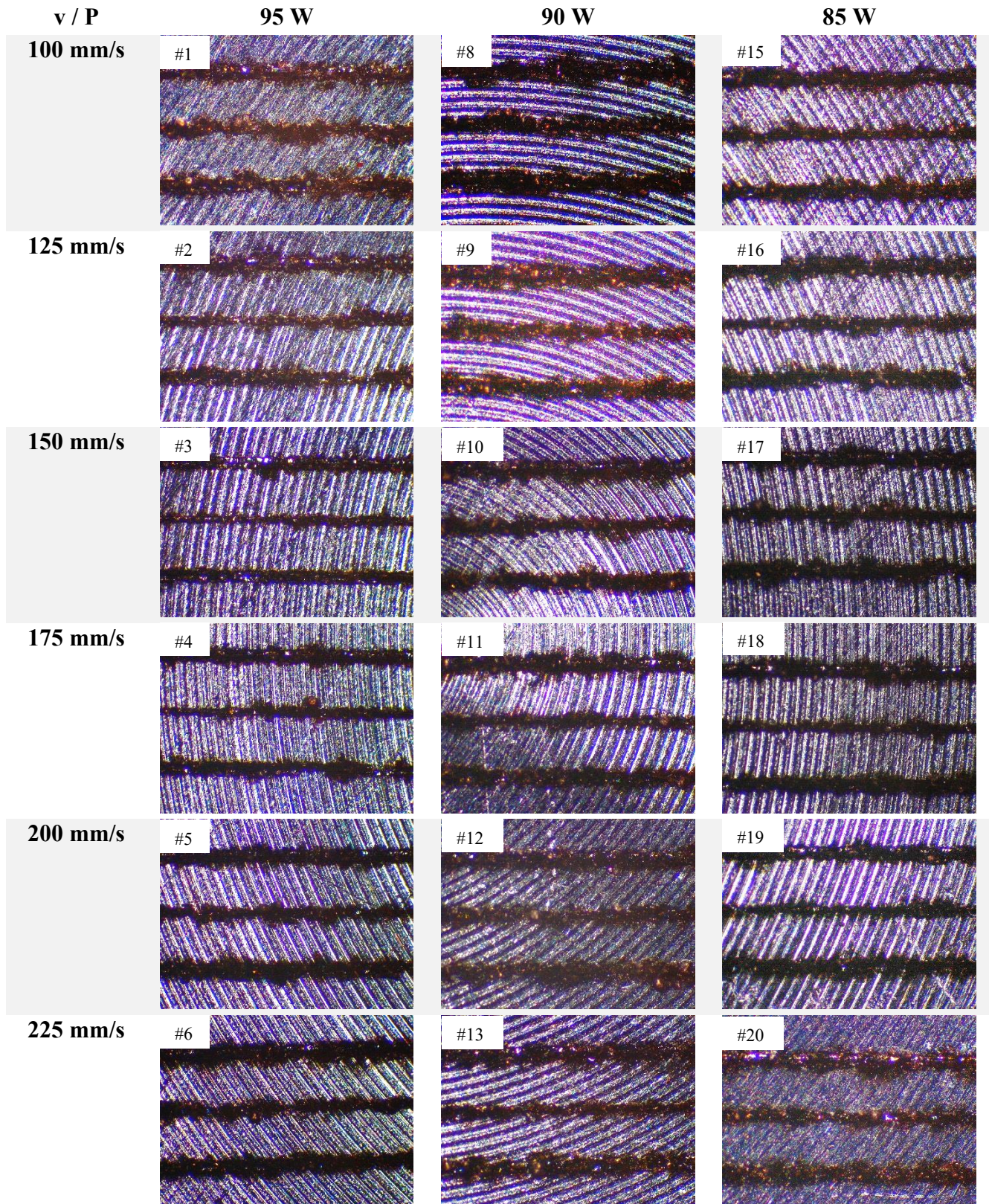


Figure 77 –  $\alpha_{right}$  versus LED of the SSTs of pure Cu in logarithmic scale

From the graphs, it can be seen that, as it was predictable, all the geometrical features measured show the lowest values in the “not enough LED” category, where the melt pools are rather visible. Another aspect that can be highlighted from the diagrams is that the depth of the melt pools is always lower than the height, indicating a lack of wettability. Above all of them, the depth is generally negligible for the scan tracks affected by balling. Moreover, these melt pools are also characterized by a quite large scattering of values of angles. Finally, what stands out from the plots above is that no clear trend of the melt pools' dimensions can be defined according to the increment in LED given.

# Cu – 0.5% wt. milled C SSTs

On top observation through stereomicroscope are reported below.



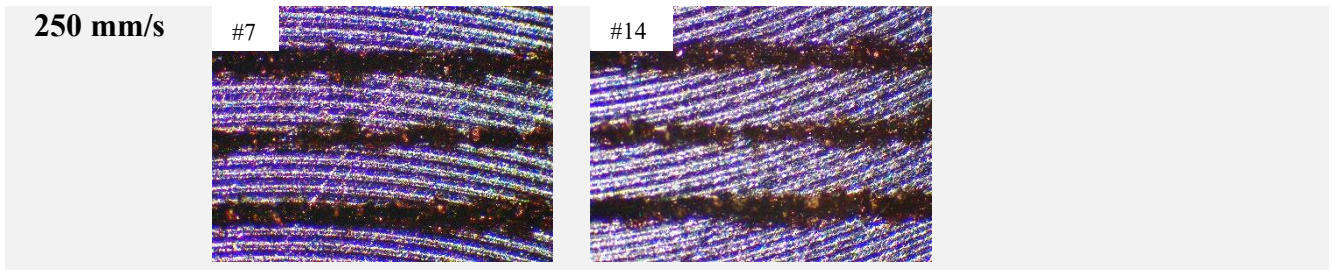
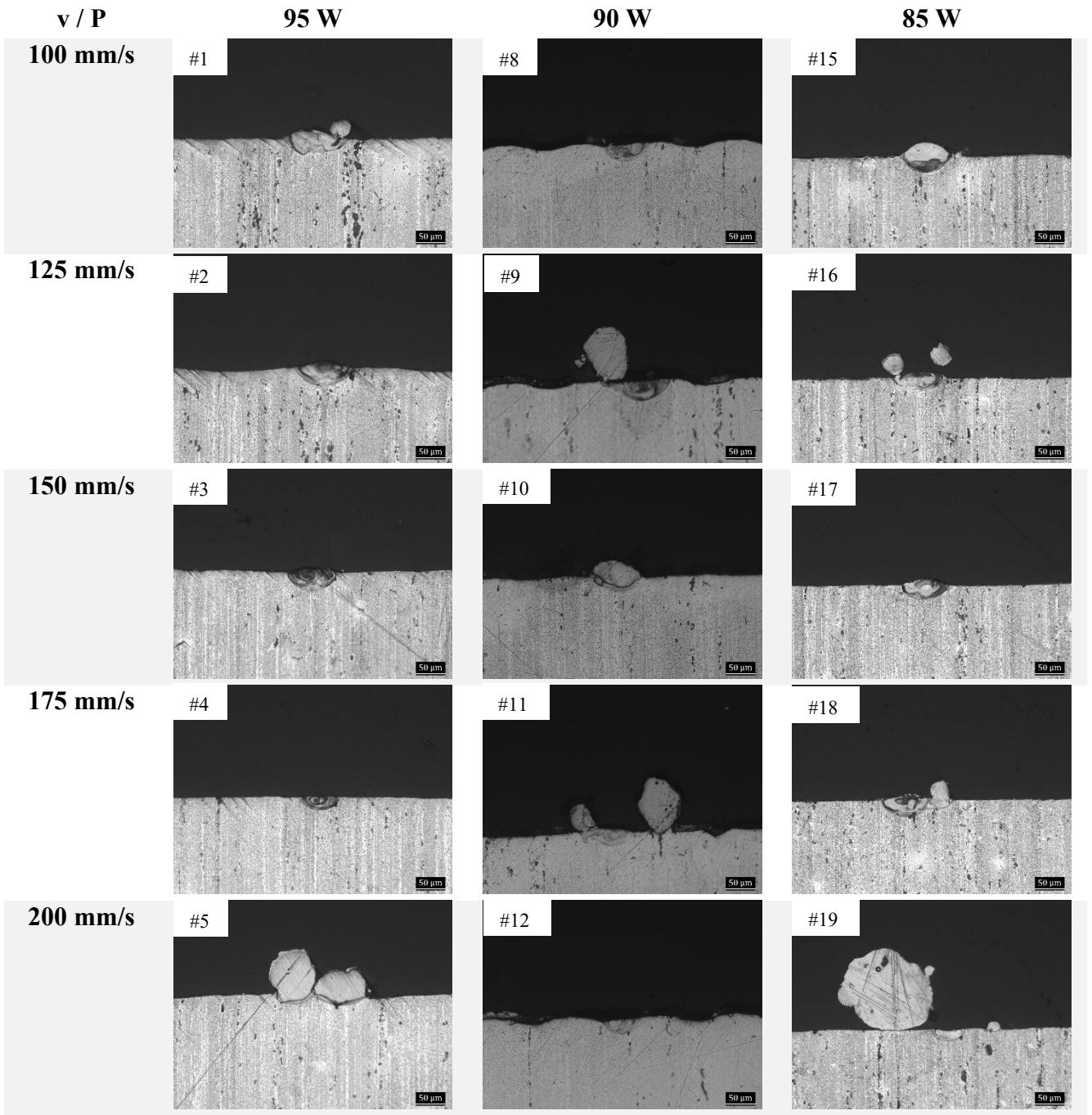


Table 9 – On top observation of Cu – 0.5% milled C SSTs

Table 10 shows the images collected at the optical microscope of the cross-section of the melt pools.



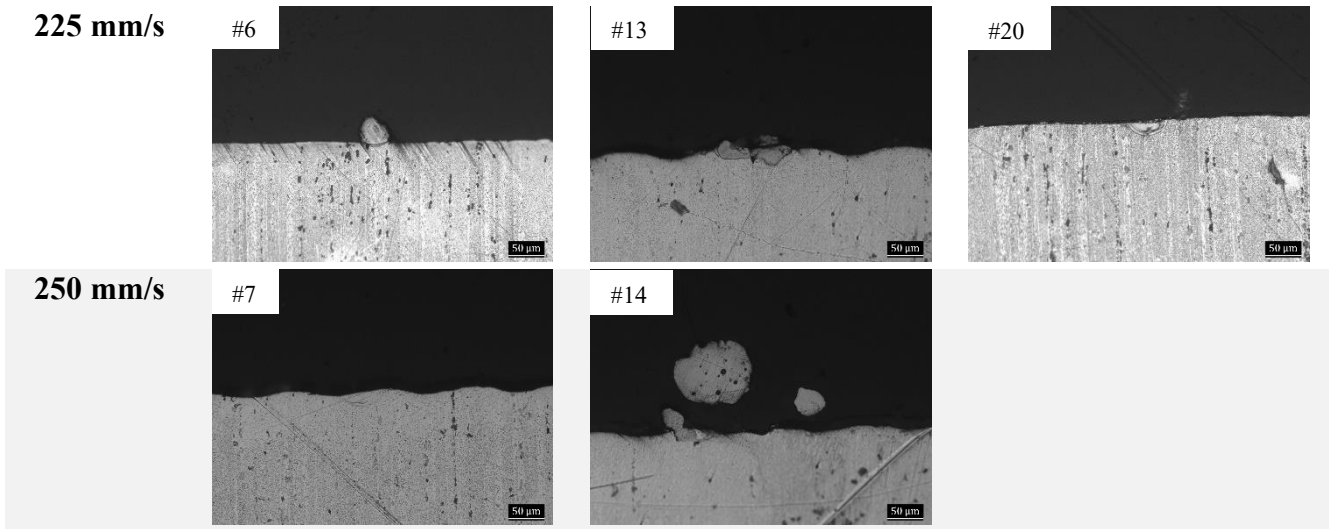


Table 10 – Cross-section observation of Cu – 0.5% milled C SSTs

Also, for this second set of SSTs, it was possible to categorize the melt pools according to the images collected at the microscopes. This distinction is presented in Figure 78.

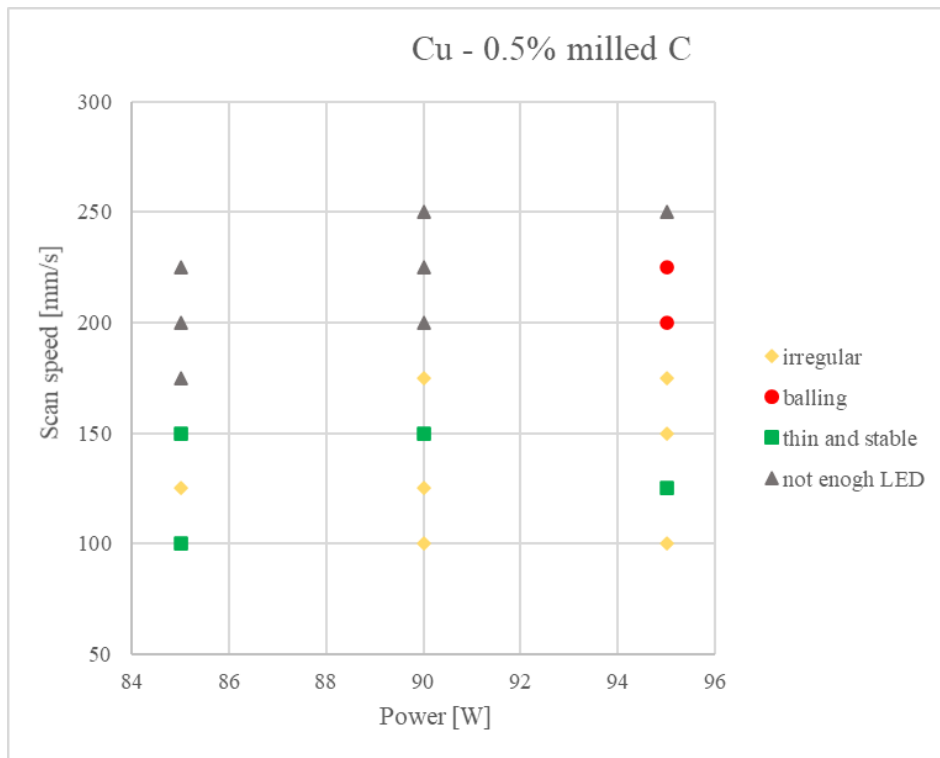


Figure 78 - Scan speed versus Power of the SSTs of Cu – 0.5% milled C

As it is possible to see, the behaviour of the SSTs built with the second mixture results more predictable, as it follows more the increment in LED. In general, the melt pools look more stable, and a less balling effect is detected. Still, the processing window remains quite narrow.

The best results for this second mixture are samples #10 and #15, which are processed respectively with a laser power of 95 and 85W and a scan speed of 225 and 100mm/s, for a resulting LED of 0.6 and 0.85J/mm. It is interesting to highlight that processing pure copper at the same parameters;



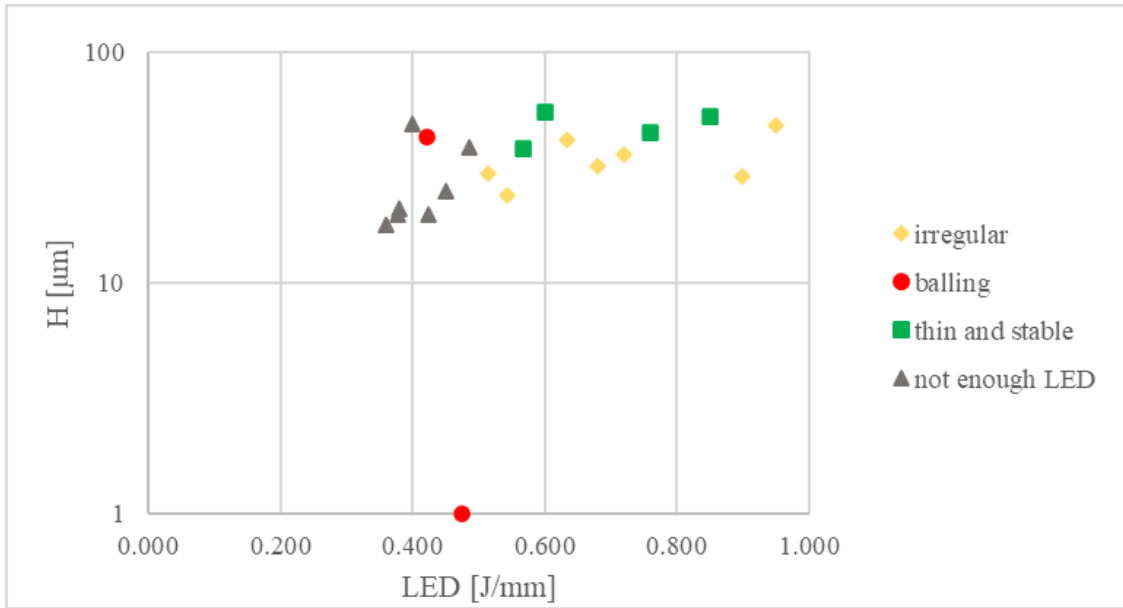


Figure 81 –  $H$  versus LED of the SSTs of Cu – 0.5% milled C in logarithmic scale

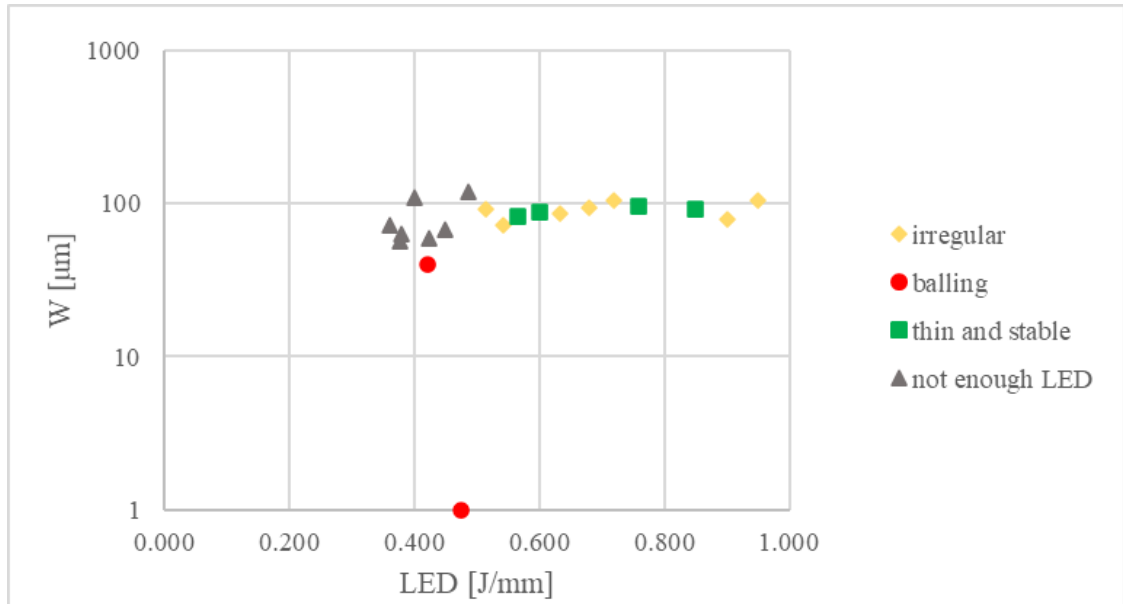


Figure 82 –  $W$  versus LED of the SSTs of Cu – 0.5% milled C in logarithmic scale

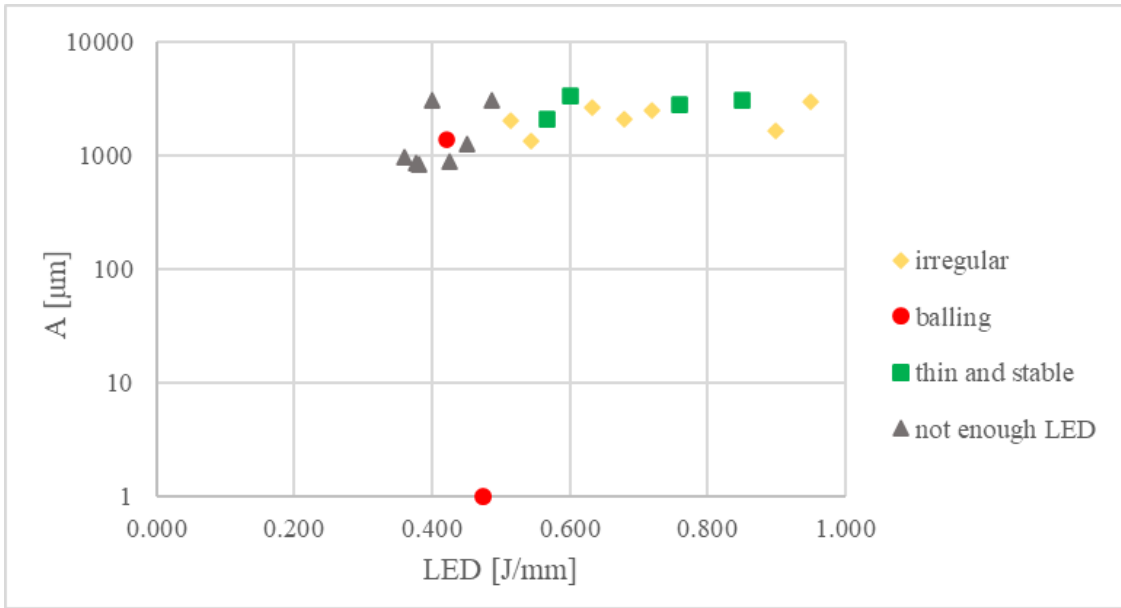


Figure 83 –  $A$  versus LED of the SSTs of Cu – 0.5% milled C in logarithmic scale

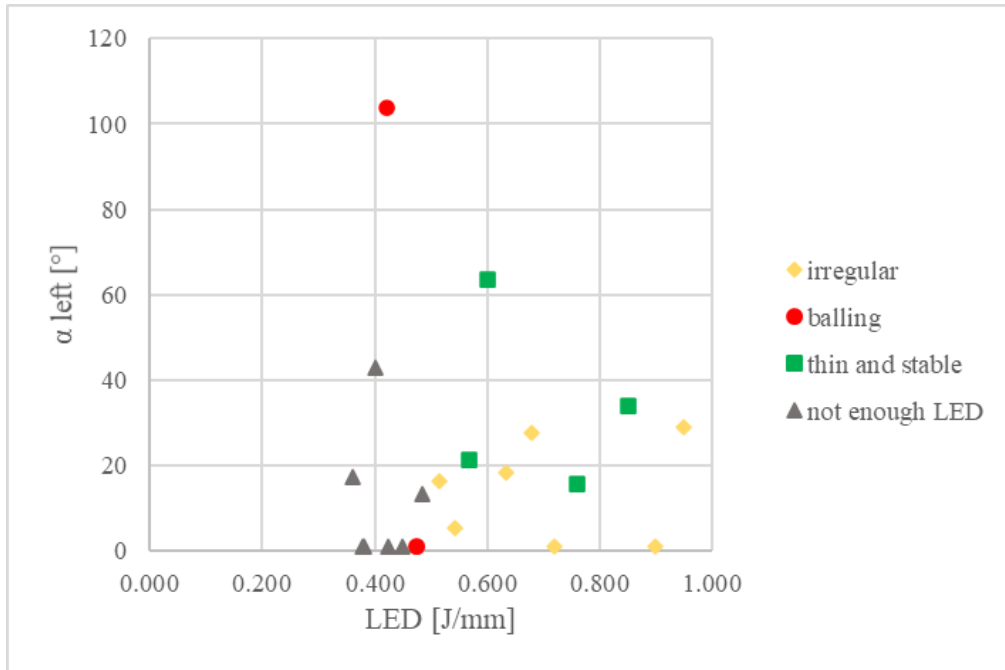


Figure 84 –  $\alpha_{\text{left}}$  versus LED of the SSTs of Cu – 0.5% milled C in logarithmic scale

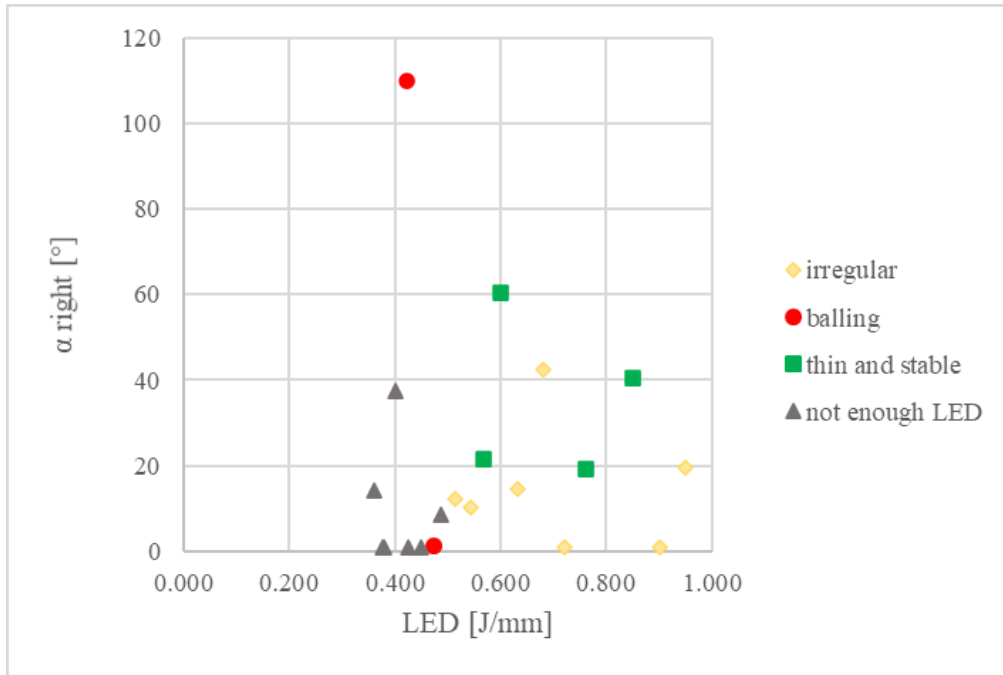


Figure 85 –  $\alpha_{right}$  versus LED of the SSTs of Cu – 0.5% milled C in logarithmic scale

Generally, as the melt pools result more stable with respect to the former ones, the dimensions are bigger, in particular the values of width. As a matter of fact, the higher the LED absorbed, the larger the melt pools. This is also true for the “not enough LED” category: even if the LED given is low, the mixture of copper and graphite can melt and form a small melt pool.

Closer inspection of the plots shows that in general, over 0.5 J/mm, the width seems not to be affected by the increase in LED and remains quite stable around a value of 100  $\mu\text{m}$ .

For what concerns the irregular melt pools, they are strongly asymmetrical and present a large scattering of values among the angles  $\alpha_{right}$  and  $\alpha_{left}$  and the heights  $h_{up}$  and  $h_{down}$ , with very limited depths. On the opposite, thin and stable cross-sections are characterized by similar and stable values of angles and a depth comparable with the height.

In conclusion, from the optical analysis of the cross-sections it can be stated that the addition of this second element can be crucial in the processability of copper through LPBF.

## Chapter 4

### Conclusions

As previously explained, the present research aimed to examine the state of art of copper through AM technologies and suggest a new solution to face the challenges presented to the fabrication through LPBF, one of the most used in metal applications.

The literature review has shown that the main issue related to the processability of copper through LPBF is its low laser absorptivity. Above all the solutions to overcome this obstacle, the most important one is the addition to pure copper of a second element with a higher laser absorption rate. Still, this is not a trivial operation since the addition of other elements can be detrimental to the electrical conductivity and the mechanical properties of the final component.

In this study, the effects of the addition of different amounts of graphite to copper powder have been analyzed. Graphite, with its higher laser absorption rate, helps to improve the manufacturing of copper through LAM. In contrast, the quantity and the dimensions of graphite's flakes need to be carefully selected in order not to destroy the spreadability of the mixture. For this reason, the first characterization of different powders has been carried out. The analysis results have shown that the best quantity of graphite to be added ranges between 0.5% and 1% in weight. With these values, a good level of density, flowability and spreadability is obtained. Moreover, high coverage of copper particles is ensured, and no graphite's agglomerations are detected. Finally, to obtain a more uniform distribution of the second element, it is possible to mill graphite and reduce its average dimensions: the smaller the flakes, the higher the ability to stick around copper particles and cover them.

Subsequently, four jobs have been processed with Concept Laser MLabR, aiming at testing the mixtures and defining an optimum set of process parameters. All these experiments failed after printing about ten layers. In particular, the first job, which employed pure copper sieved below 40  $\mu\text{m}$ , has shown that this metal cannot be sintered using a VED lower than  $1000 \text{ J/mm}^3$ . The next jobs were concerned with the effect of the addition of different quantities of graphite. The results of this activity suggest that thanks to the addition of graphite, copper is able to reach a higher level of melting, but at the same time, an inhomogeneous distribution of graphite leads to the release of smoke during the printing phase, which interferes with the correct development of the process. Further, after this study, it is possible to assess that the flowability of the mixture improves with a

reduction in size and content of graphite, indicating that the powder which is the most favourable to be processed through LPBF is the Cu – 0.5% milled graphite.

However, as already stated, all these jobs were not completed. The main source of weakness of this activity was a too low laser power: it is not possible to completely melt copper with an input power of 95W. For this reason, it was decided to conduct an SSTs analysis to study the effects of different LED absorbed on the geometry of melt pools.

Two sets of SSTs were printed: pure copper and a mixture of Cu - 0.5% milled C were employed. The samples have been observed both on-top and at the cross-section, and the most relevant dimensions of the melt pools have been measured. The images collected allow a comparison between the two sets of scan tracks. In the case of pure copper, it was harder to define a clear trend of the morphology of the melt pools related to the increment of given LED. The mixture of copper and graphite, instead, seems to undergo a more definite pattern.

Moreover, with the addition of graphite, the melt pools generally look more stable and wider with respect to the former ones. This suggests that the mixture is able to absorb a larger amount of LED, increasing the dimensions of the melt pools. As a matter of fact, in the case of very low LED, it was possible to detect the melting of the material, while for pure copper, this was rather visible.

Finally, from the observation of the SSTs, it was found out that the processing window remains still quite narrow. In fact, it is clear that for both powders, a LED lower than 0.38 J/mm is not sufficient to ensure the material's melting, while a value of energy higher than 0.95 J/mm generates irregular scan tracks.

In conclusion, from the optical analysis of the cross-sections it can be stated that the addition of this second element can be crucial in the processability of copper through LPBF, as the scan track result stable and continuous and the melt pools more regular.

This study lays the groundwork for future research into the successful fabrication through LPBF of copper components thanks to the addition of a small percentage of graphite. Hopefully, it will be possible to produce parts with complex design and excellent thermal and electrical conductivity in the future.

## Bibliography

- [1] M. Colopi, A. G. Demir, L. Caprio, and B. Previtali, “Limits and solutions in processing pure Cu via selective laser melting using a high-power single-mode fiber laser,” *Int. J. Adv. Manuf. Technol.*, vol. 104, no. 5, pp. 2473–2486, 2019, doi: 10.1007/s00170-019-04015-3.
- [2] “ASTM F2792-10, Standard Terminology for Additive Manufacturing Technologies, ASTM International, West Conshohocken, PA, 2010, [www.astm.org](http://www.astm.org).”
- [3] D. Herzog, V. Seyda, E. Wycisk, and C. Emmelmann, “Additive manufacturing of metals,” *Acta Mater.*, vol. 117, pp. 371–392, 2016, doi: <https://doi.org/10.1016/j.actamat.2016.07.019>.
- [4] E. Atzeni and A. Salmi, “Economics of additive manufacturing for end-usable metal parts,” *Int. J. Adv. Manuf. Technol.*, vol. 62, no. 9–12, pp. 1147–1155, 2012, doi: 10.1007/s00170-011-3878-1.
- [5] N. Haghdadi, M. Laleh, M. Moyle, and S. Primig, “Additive manufacturing of steels: a review of achievements and challenges,” *J. Mater. Sci.*, vol. 56, no. 1, pp. 64–107, 2021, doi: 10.1007/s10853-020-05109-0.
- [6] U. M. Dilberoglu, B. Gharehpapagh, U. Yaman, and M. Dolen, “The Role of Additive Manufacturing in the Era of Industry 4.0,” *Procedia Manuf.*, vol. 11, pp. 545–554, 2017, doi: <https://doi.org/10.1016/j.promfg.2017.07.148>.
- [7] A. A. Mousa and M. O. Bashir, “Additive Manufacturing: A New Industrial Revolution- A review,” *J. Sci. Achiev.*, vol. 2, no. 3, pp. 19–31, 2017, [Online]. Available: [http://jsciachv.sinaweb.net/article\\_80742.html](http://jsciachv.sinaweb.net/article_80742.html).
- [8] K. Rajaguru, T. Karthikeyan, and V. Vijayan, “Additive manufacturing – State of art,” *Mater. Today Proc.*, vol. 21, pp. 628–633, 2020, doi: <https://doi.org/10.1016/j.matpr.2019.06.728>.
- [9] P. M. A. Saboori, A. Salmi, “Notes of the course: Additive Manufacturing Systems and materials.” Politecnico di Torino, 2020.
- [10] F. M. Li Yang, Keng Hsu, Brian Baughman, Donald Godfrey and S. W. Mamballykalathil Menon, *Additive manufacturing of metals: the technology, materials, design and production*. 2017.
- [11] M. Attaran, “The rise of 3-D printing: The advantages of additive manufacturing over traditional manufacturing,” *Bus. Horiz.*, vol. 60, no. 5, pp. 677–688, 2017, doi: <https://doi.org/10.1016/j.bushor.2017.05.011>.
- [12] W. E. Frazier, “Metal additive manufacturing: A review,” *J. Mater. Eng. Perform.*, vol. 23, no. 6, pp. 1917–1928, 2014, doi: 10.1007/s11665-014-0958-z.
- [13] N. Guo and M. C. Leu, “Additive manufacturing: Technology, applications and research needs,” *Front. Mech. Eng.*, vol. 8, no. 3, pp. 215–243, 2013, doi: 10.1007/s11465-013-0248-8.
- [14] V. Petrovic, J. Vicente Haro Gonzalez, O. Jordá Ferrando, J. Delgado Gordillo, J. Ramon Blasco Puchades, and L. Portoles Grinan, “Additive layered manufacturing: Sectors of industrial application shown through case studies,” *Int. J. Prod. Res.*, vol. 49, no. 4, pp. 1061–1079, 2011, doi: 10.1080/00207540903479786.
- [15] P. Szymczyk-Ziółkowska, M. B. Łabowska, J. Detyna, I. Michalak, and P. Gruber, “A review of fabrication polymer scaffolds for biomedical applications using additive manufacturing techniques,” *Biocybern. Biomed. Eng.*, vol. 40, no. 2, pp. 624–638, 2020, doi: <https://doi.org/10.1016/j.bbe.2020.01.015>.
- [16] F. Calignano *et al.*, “Overview on Additive Manufacturing Technologies,” *Proc. IEEE*, vol. 105, no. 4, pp. 593–612, 2017.

- [17] E. S. Gamov, S. B. Tonkovid, V. A. Kukushkina, and N. A. Nikulcheva, "A 3D design based on jewelry production technology with special features," *Int. J. Eng. Technol.*, vol. 7, no. 3, pp. 10–12, 2018, doi: 10.14419/ijet.v7i3.5.15190.
- [18] Z. Lu, C. K. Chua, and E. C. H. Choo, "Application of polyjet technology in additive manufacturing of personalised nail art," in *Proceedings of the International Conference on Progress in Additive Manufacturing*, 2016, vol. Part F1290, pp. 55–60, [Online]. Available: <https://www.scopus.com/inward/record.uri?eid=2-s2.0-85027553878&partnerID=40&md5=806cddb648c14e3018cfbf4afd79515>.
- [19] N. I. Jaksic and P. D. Desai, "Characterization of resistors created by fused filament fabrication using electrically-conductive filament," in *Procedia Manufacturing*, 2018, vol. 17, pp. 37–44, doi: 10.1016/j.promfg.2018.10.010.
- [20] Y. Song, R. A. Boekraad, L. Roussos, A. Kooijman, C. C. L. Wang, and J. M. P. Geraedts, "3D Printed electronics: Opportunities and challenges from case studies," in *Proceedings of the ASME Design Engineering Technical Conference*, 2017, vol. 1, doi: 10.1115/DETC2017-67503.
- [21] S. E. Brika, M. Letenneur, C. A. Dion, and V. Brailovski, "Influence of particle morphology and size distribution on the powder flowability and laser powder bed fusion manufacturability of Ti-6Al-4V alloy," *Addit. Manuf.*, vol. 31, 2020, doi: 10.1016/j.addma.2019.100929.
- [22] G. Jacob, G. Jacob, C. U. Brown, and A. Donmez, *The influence of spreading metal powders with different particle size distributions on the powder bed density in laser-based powder bed fusion processes*. US Department of Commerce, National Institute of Standards and Technology, 2018.
- [23] J.-P. Kruth, J. Deckers, E. Yasa, and R. Wauthlé, "Assessing and comparing influencing factors of residual stresses in selective laser melting using a novel analysis method," *Proc. Inst. Mech. Eng. Part B J. Eng. Manuf.*, vol. 226, no. 6, pp. 980–991, 2012, doi: 10.1177/0954405412437085.
- [24] K. Riener *et al.*, "Influence of particle size distribution and morphology on the properties of the powder feedstock as well as of AlSi10Mg parts produced by laser powder bed fusion (LPBF)," *Addit. Manuf.*, vol. 34, 2020, doi: 10.1016/j.addma.2020.101286.
- [25] "Copper as Electrical Conductive Material with Above-Standard Performance Properties," vol. 1–38, 2015.
- [26] L. Kaden *et al.*, "Selective laser melting of copper using ultrashort laser pulses," *Appl. Phys. A*, vol. 123, no. 9, p. 596, 2017, doi: 10.1007/s00339-017-1189-6.
- [27] S. D. Jadhav *et al.*, "Influence of Carbon Nanoparticle Addition (and Impurities) on Selective Laser Melting of Pure Copper," *Materials (Basel)*, vol. 12, no. 15, p. 2469, Aug. 2019, doi: 10.3390/ma12152469.
- [28] R. Guschlbauer, S. Momeni, F. Osmanlic, and C. Körner, "Process development of 99.95% pure copper processed via selective electron beam melting and its mechanical and physical properties," *Mater. Charact.*, vol. 143, pp. 163–170, 2018, doi: <https://doi.org/10.1016/j.matchar.2018.04.009>.
- [29] V. Sufiiarov, E. Borisov, and I. Polozov, "SELECTIVE LASER MELTING OF COPPER ALLOY," *Mater. Phys. Mech.*, vol. 43, pp. 65–71, Jan. 2020, doi: 10.18720/MPM.4312020\_8.
- [30] F. Trevisan, F. Calignano, M. Lorusso, M. Lombardi, D. Manfredi, and P. Fino, "Selective laser melting of chemical pure copper," 2017.
- [31] R. Neugebauer, B. Mueller, M. Gebauer, and T. Töppel, "Additive manufacturing boosts efficiency of heat transfer components," *Assem. Autom.*, vol. 31, pp. 344–347, Sep. 2011, doi: 10.1108/01445151111172925.
- [32] L. Benedetti, C. Comelli, and C. Ahrens, *Study on Selective Laser Melting of Copper*. 2017.
- [33] J. P. Kruth, L. Froyen, J. Van Vaerenbergh, P. Mercelis, M. Rombouts, and B. Lauwers, "Selective

- laser melting of iron-based powder,” *J. Mater. Process. Technol.*, vol. 149, no. 1, pp. 616–622, 2004, doi: <https://doi.org/10.1016/j.jmatprotec.2003.11.051>.
- [34] M. Leary, “Chapter 11 - Powder bed fusion,” in *Additive Manufacturing Materials and Technologies*, M. B. T.-D. for A. M. Leary, Ed. Elsevier, 2020, pp. 295–319.
- [35] R. Goodridge and S. Ziegelmeier, “7 - Powder bed fusion of polymers,” in *Woodhead Publishing Series in Electronic and Optical Materials*, M. B. T.-L. A. M. Brandt, Ed. Woodhead Publishing, 2017, pp. 181–204.
- [36] Y. Bai and C. B. Williams, “An exploration of binder jetting of copper,” *Rapid Prototyp. J.*, vol. 21, no. 2, pp. 177–185, 2015, doi: 10.1108/RPJ-12-2014-0180.
- [37] J. D. Martin, “Exploring Additive Manufacturing Processes for Direct 3D Printing of Copper Induction Coils,” vol. 2, 2017, [Online]. Available: <https://doi-org.ezproxy.biblio.polito.it/10.1115/IMECE2017-71685>.
- [38] T. I. El-Wardany, Y. She, V. N. Jagdale, J. K. Garofano, J. J. Liou, and W. R. Schmidt, “Challenges in Three-Dimensional Printing of High-Conductivity Copper,” *J. Electron. Packag.*, vol. 140, no. 2, May 2018, doi: 10.1115/1.4039974.
- [39] F. Singer, D. C. Deisenroth, D. M. Hymas, and M. M. Ohadi, “Additively manufactured copper components and composite structures for thermal management applications,” in *2017 16th IEEE Intersociety Conference on Thermal and Thermomechanical Phenomena in Electronic Systems (ITherm)*, 2017, pp. 174–183, doi: 10.1109/ITHERM.2017.7992469.
- [40] T. Q. Tran *et al.*, “3D printing of highly pure copper,” *Metals (Basel)*, vol. 9, no. 7, 2019, doi: 10.3390/met9070756.
- [41] Z. Ma, K. Zhang, Z. Ren, D. Z. Zhang, G. Tao, and H. Xu, “Selective laser melting of Cu–Cr–Zr copper alloy: Parameter optimization, microstructure and mechanical properties,” *J. Alloys Compd.*, vol. 828, p. 154350, 2020, doi: <https://doi.org/10.1016/j.jallcom.2020.154350>.
- [42] K. IMAI, T.-T. Ikeshoji, Y. SUGITANI, and H. KYOGOKU, “Densification of pure copper by selective laser melting process,” *Mech. Eng. J.*, Mar. 2020, doi: 10.1299/mej.19-00272.
- [43] J. Huang *et al.*, “Pure copper components fabricated by cold spray (CS) and selective laser melting (SLM) technology,” *Surf. Coatings Technol.*, vol. 395, p. 125936, 2020, doi: <https://doi.org/10.1016/j.surfcoat.2020.125936>.
- [44] F. Sciammarella, M. Gonser, and M. Styrcula, *Laser Additive Manufacturing of Pure Copper*. 2013.
- [45] L. Sobotova and M. Badida, “Laser marking as environment technology,” *Open Eng.*, vol. 7, no. 1, pp. 303–316, doi: <https://doi.org/10.1515/eng-2017-0030>.
- [46] V. Lindström *et al.*, “Laser Powder Bed Fusion of Metal Coated Copper Powders,” *Materials (Basel)*, vol. 13, p. 3493, Aug. 2020, doi: 10.3390/ma13163493.
- [47] S. D. Jadhav, S. Dadbakhsh, L. Goossens, J.-P. Kruth, J. Van Humbeeck, and K. Vanmeensel, “Influence of selective laser melting process parameters on texture evolution in pure copper,” *J. Mater. Process. Technol.*, vol. 270, pp. 47–58, 2019, doi: <https://doi.org/10.1016/j.jmatprotec.2019.02.022>.
- [48] T. Stoll, P. Trautnitz, S. Schmiedeke, J. Franke, and N. Travitzky, “Process development for laser powder bed fusion of pure copper,” in *Proc.SPIE*, Mar. 2020, vol. 11271, doi: 10.1117/12.2563870.
- [49] X. Yan *et al.*, “Microstructure and mechanical properties of pure copper manufactured by selective laser melting,” *Mater. Sci. Eng. A*, vol. 789, p. 139615, 2020, doi: <https://doi.org/10.1016/j.msea.2020.139615>.
- [50] P. Lykov, E. V Safonov, and A. Akhmedianov, “Selective Laser Melting of Copper,” *Mater. Sci. Forum*, vol. 843, pp. 284–288, Feb. 2016, doi: 10.4028/www.scientific.net/MSF.843.284.

- [51] G. Jieren, Z. Xiaowei, J. Yehua, and Y. Yongnian, "Insights into fabrication mechanism of pure copper thin wall components by selective infrared laser melting," *Rapid Prototyp. J.*, vol. 25, no. 8, pp. 1388–1397, Jan. 2019, doi: 10.1108/RPJ-06-2018-0143.
- [52] C. Silbernagel, L. Gargalis, I. Ashcroft, R. Hague, M. Galea, and P. Dickens, "Electrical resistivity of pure copper processed by medium-powered laser powder bed fusion additive manufacturing for use in electromagnetic applications," *Addit. Manuf.*, vol. 29, Oct. 2019, doi: 10.1016/j.addma.2019.100831.
- [53] S. D. Jadhav, P. P. Dhekne, S. Dadbakhsh, J.-P. Kruth, J. Van Humbeeck, and K. Vanmeensel, "Surface Modified Copper Alloy Powder for Reliable Laser-based Additive Manufacturing," *Addit. Manuf.*, vol. 35, 2020, doi: 10.1016/j.addma.2020.101418.
- [54] K. Imai and T. Ikeshoji, "Advance Publication by J-STAGE Mechanical Engineering Journal Densification of pure copper by selective laser melting process," 2020, doi: 10.1299/mej.19-00272.
- [55] T.-T. Ikeshoji, K. Nakamura, M. Yonehara, K. Imai, and H. Kyogoku, "Selective Laser Melting of Pure Copper," *JOM*, Dec. 2017, doi: 10.1007/s11837-017-2695-x.
- [56] T. Shibata, M. Tsukamoto, Y. Sato, and S. Masuno, "Effect of input energy on densification for pure copper fabricated by SLM with blue diode laser," in *Proceedings of SPIE - The International Society for Optical Engineering*, 2019, vol. 10909, doi: 10.1117/12.2509459.
- [57] C. Wallis and B. Buchmayr, "Effect of heat treatments on microstructure and properties of CuCrZr produced by laser-powder bed fusion," *Mater. Sci. Eng. A*, vol. 744, pp. 215–223, 2019, doi: <https://doi.org/10.1016/j.msea.2018.12.017>.
- [58] A. Popovich, V. Sufiiarov, I. Polozov, E. Borisov, D. Masaylo, and A. Orlov, "Microstructure and mechanical properties of additive manufactured copper alloy," *Mater. Lett.*, vol. 179, pp. 38–41, 2016, doi: <https://doi.org/10.1016/j.matlet.2016.05.064>.
- [59] S. Zhang, H. Zhu, L. Zhang, W. Zhang, H. Yang, and X. Zeng, "Microstructure and properties of high strength and high conductivity Cu-Cr alloy components fabricated by high power selective laser melting," *Mater. Lett.*, vol. 237, pp. 306–309, 2019, doi: <https://doi.org/10.1016/j.matlet.2018.11.118>.
- [60] S. Scudino *et al.*, "Additive manufacturing of Cu–10Sn bronze," *Mater. Lett.*, vol. 156, pp. 202–204, 2015, doi: <https://doi.org/10.1016/j.matlet.2015.05.076>.
- [61] Z. Mao, D. Z. Zhang, J. Jiang, G. Fu, and P. Zhang, "Processing optimisation, mechanical properties and microstructural evolution during selective laser melting of Cu-15Sn high-tin bronze," *Mater. Sci. Eng. A*, vol. 721, pp. 125–134, 2018, doi: <https://doi.org/10.1016/j.msea.2018.02.051>.
- [62] G. Zhang *et al.*, "Additive manufacturing of fine-structured copper alloy by selective laser melting of pre-alloyed Cu-15Ni-8Sn powder," *Int. J. Adv. Manuf. Technol.*, vol. 96, no. 9, pp. 4223–4230, 2018, doi: 10.1007/s00170-018-1891-3.
- [63] M. A. Lodes, R. Guschlbauer, and C. Körner, "Process development for the manufacturing of 99.94% pure copper via selective electron beam melting," *Mater. Lett.*, vol. 143, pp. 298–301, 2015, doi: <https://doi.org/10.1016/j.matlet.2014.12.105>.
- [64] L. E. Murr *et al.*, "Characterization of titanium aluminide alloy components fabricated by additive manufacturing using electron beam melting," *Acta Mater.*, vol. 58, no. 5, pp. 1887–1894, 2010, doi: <https://doi.org/10.1016/j.actamat.2009.11.032>.
- [65] S. J. Raab, R. Guschlbauer, M. A. Lodes, and C. Körner, "Thermal and Electrical Conductivity of 99.9% Pure Copper Processed via Selective Electron Beam Melting," *Adv. Eng. Mater.*, vol. 18, no. 9, pp. 1661–1666, Sep. 2016, doi: <https://doi.org/10.1002/adem.201600078>.
- [66] S. Yadav, C. P. Paul, A. N. Jinoop, S. K. Nayak, A. K. Rai, and K. S. Bindra, "Effect of Process Parameters on Laser Directed Energy Deposition of Copper." Dec. 05, 2019, doi:

10.1115/GTINDIA2019-2453.

- [67] W. Li, L. Yan, X. Chen, J. Zhang, X. Zhang, and F. Liou, "Directed energy depositing a new Fe-Cr-Ni alloy with gradually changing composition with elemental powder mixes and particle size' effect in fabrication process," *J. Mater. Process. Technol.*, vol. 255, pp. 96–104, 2018, doi: <https://doi.org/10.1016/j.jmatprotec.2017.12.010>.
- [68] H. Siva Prasad, F. Brueckner, J. Volpp, and A. F. H. Kaplan, "Laser metal deposition of copper on diverse metals using green laser sources," *Int. J. Adv. Manuf. Technol.*, vol. 107, no. 3–4, pp. 1559–1568, 2020, doi: [10.1007/s00170-020-05117-z](https://doi.org/10.1007/s00170-020-05117-z).
- [69] P. K. Gokuldoss, S. Kolla, and J. Eckert, "Additive manufacturing processes: Selective laser melting, electron beam melting and binder jetting-selection guidelines," *Materials (Basel)*, vol. 10, no. 6, 2017, doi: [10.3390/ma10060672](https://doi.org/10.3390/ma10060672).
- [70] A. Yegyan Kumar, Y. Bai, A. Eklund, and C. B. Williams, "The effects of Hot Isostatic Pressing on parts fabricated by binder jetting additive manufacturing," *Addit. Manuf.*, vol. 24, pp. 115–124, 2018, doi: <https://doi.org/10.1016/j.addma.2018.09.021>.
- [71] M. Galati and P. Minetola, "Analysis of Density, Roughness, and Accuracy of the Atomic Diffusion Additive Manufacturing (ADAM) Process for Metal Parts," *Mater. (Basel, Switzerland)*, vol. 12, no. 24, p. 4122, Dec. 2019, doi: [10.3390/ma12244122](https://doi.org/10.3390/ma12244122).
- [72] "Copper material datasheet," 2020. <https://markforged.com/materials/metals/copper>.
- [73] H. H. Hausner, "FRICTION CONDITIONS IN A MASS OF METAL POWDER.," 1967, [Online]. Available: <https://www.osti.gov/biblio/4566075>.
- [74] A. Aversa *et al.*, "Single scan track analyses on aluminium based powders," *J. Mater. Process. Technol.*, vol. 255, pp. 17–25, 2018, doi: [10.1016/j.jmatprotec.2017.11.055](https://doi.org/10.1016/j.jmatprotec.2017.11.055).

# Appendix

## SEM images

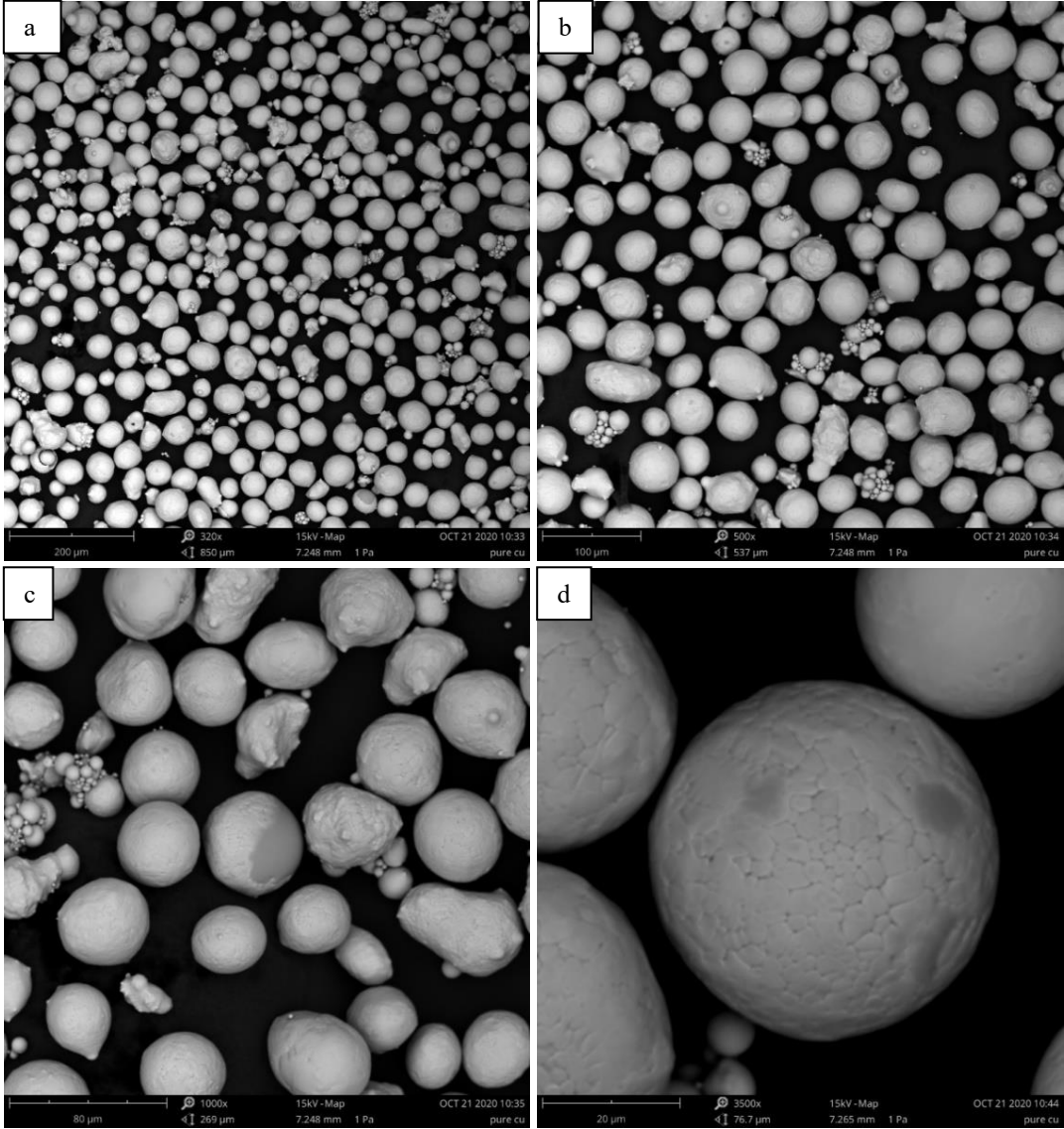


Figure A. 1 – SEM images of pure Cu. a) 320x. b) 500x. c) 1000x. d) 3500x.

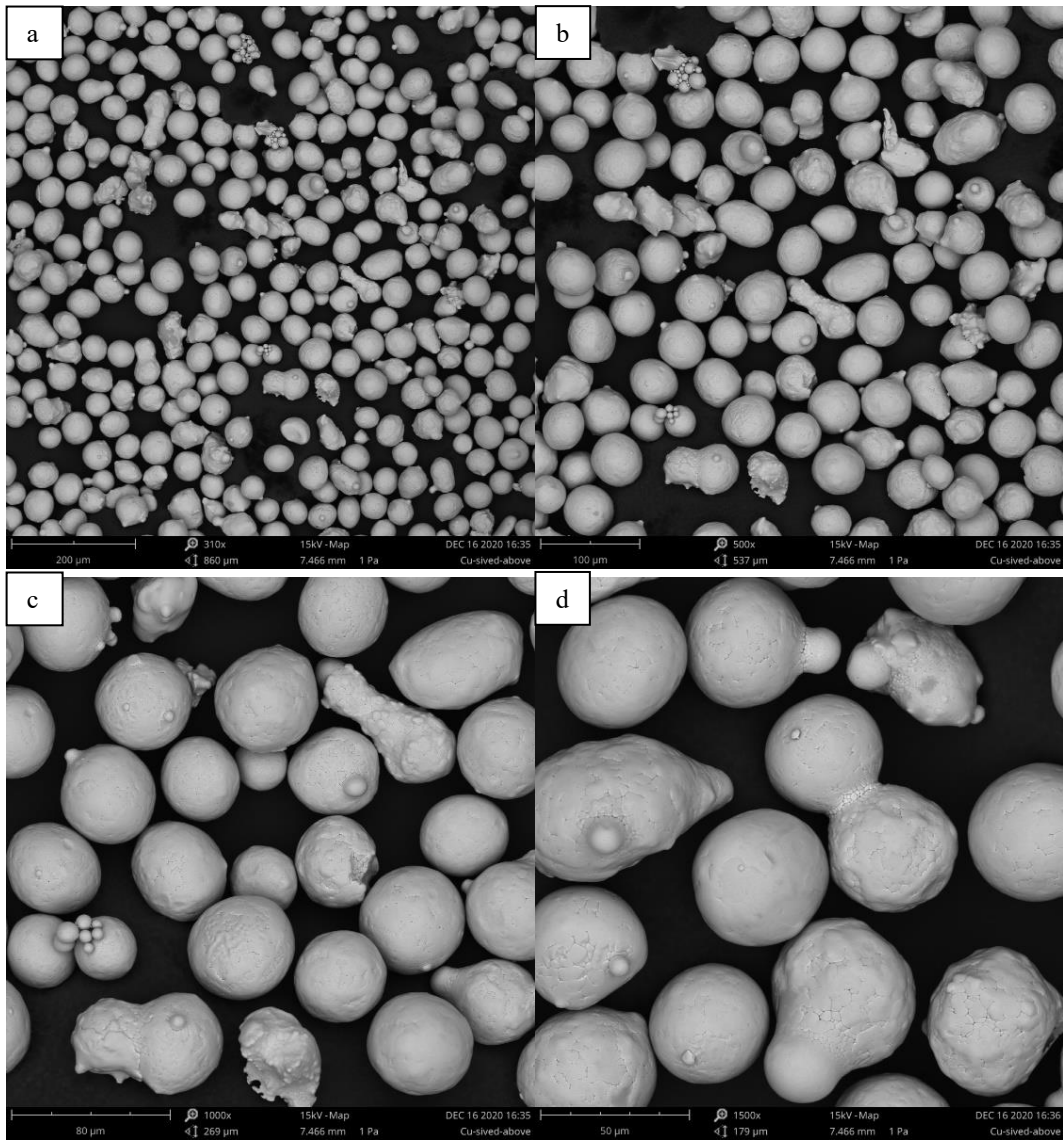


Figure A. 2 – SEM images of pure Cu sieved above 40 μm. a) 310x. b) 500x. c) 1000x. d) 1500x.

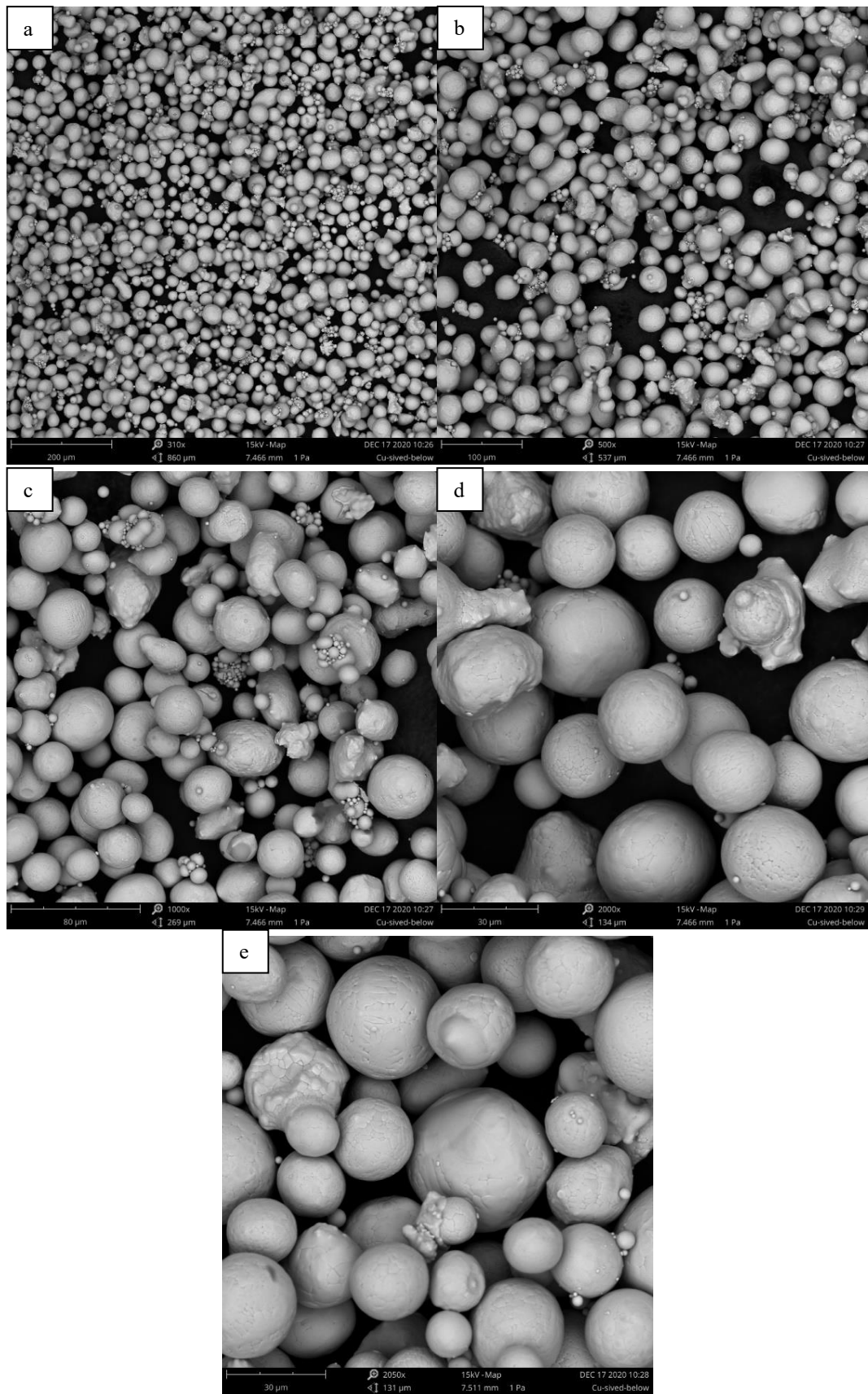


Figure A. 3 – SEM images of pure Cu sieved below 40  $\mu\text{m}$ . a) 310x. b) 500x. c) 1000x. d) 2000x. e) 2050x.

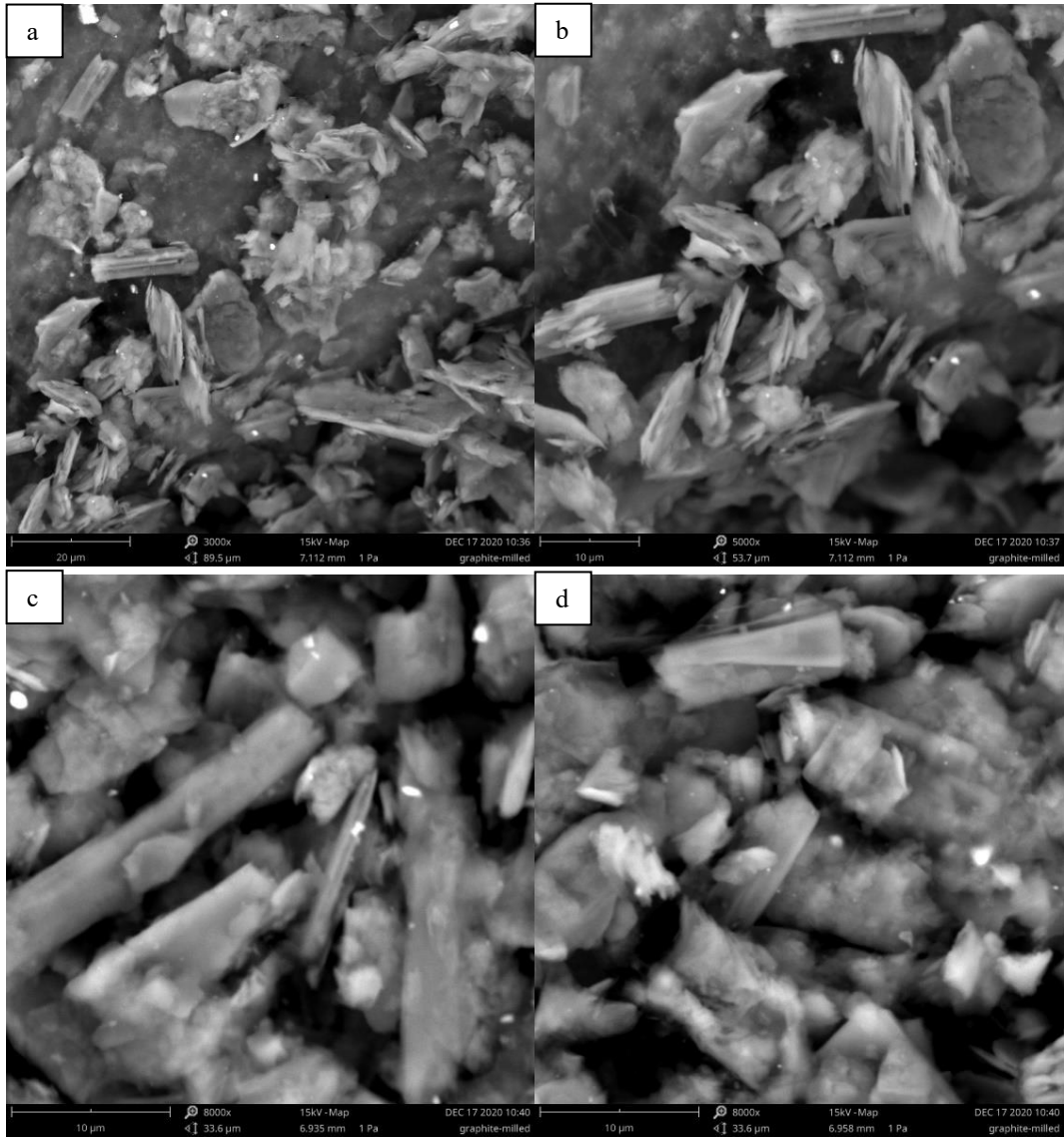


Figure A. 4 – SEM images of milled graphite. a) 3000x. b) 5000x. c) 8000x. d) 8000x.

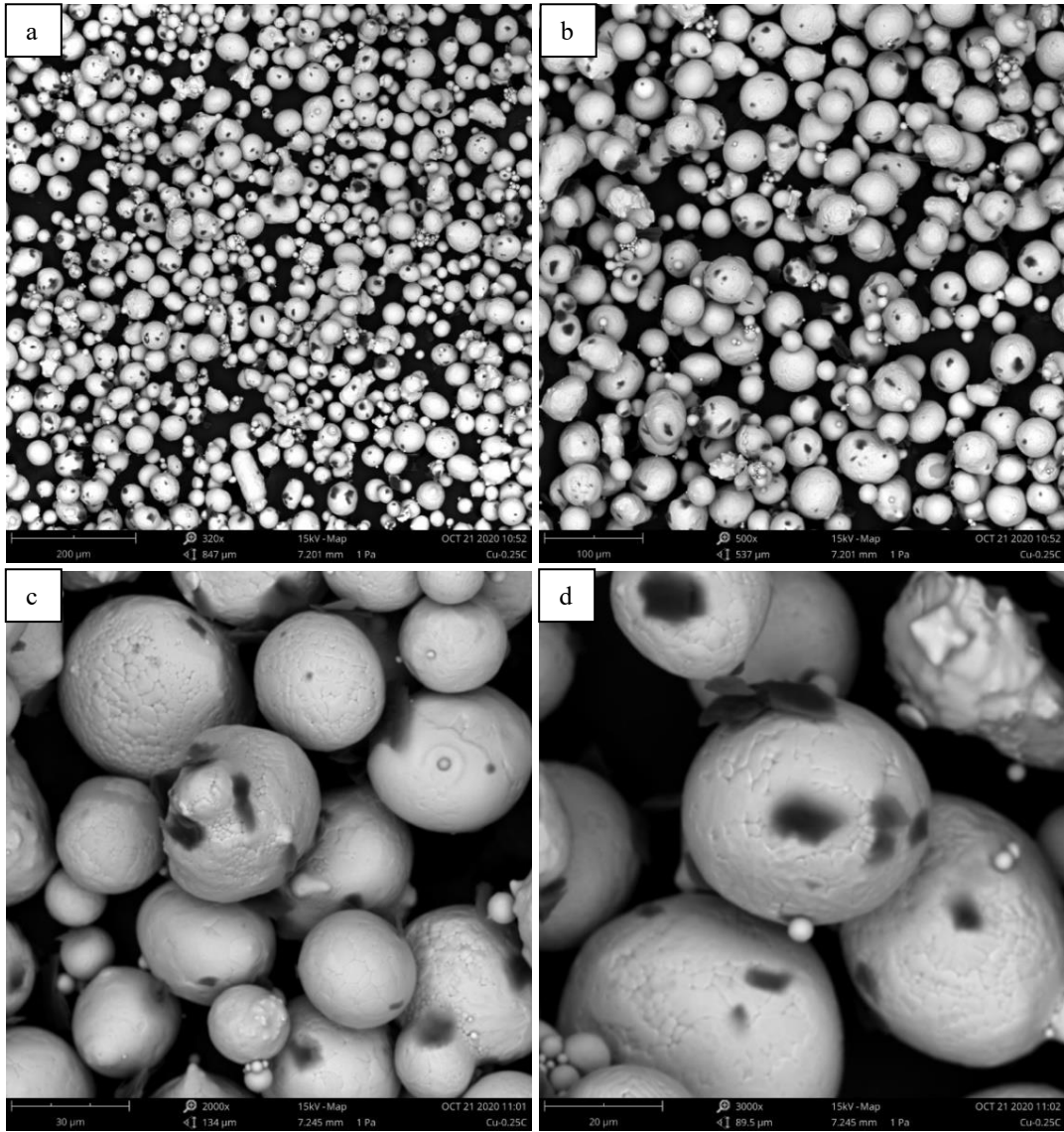


Figure A. 5 - SEM images of Cu – 0.25% C. a) 320x. b) 500x. c) 2000x. d) 3000x.

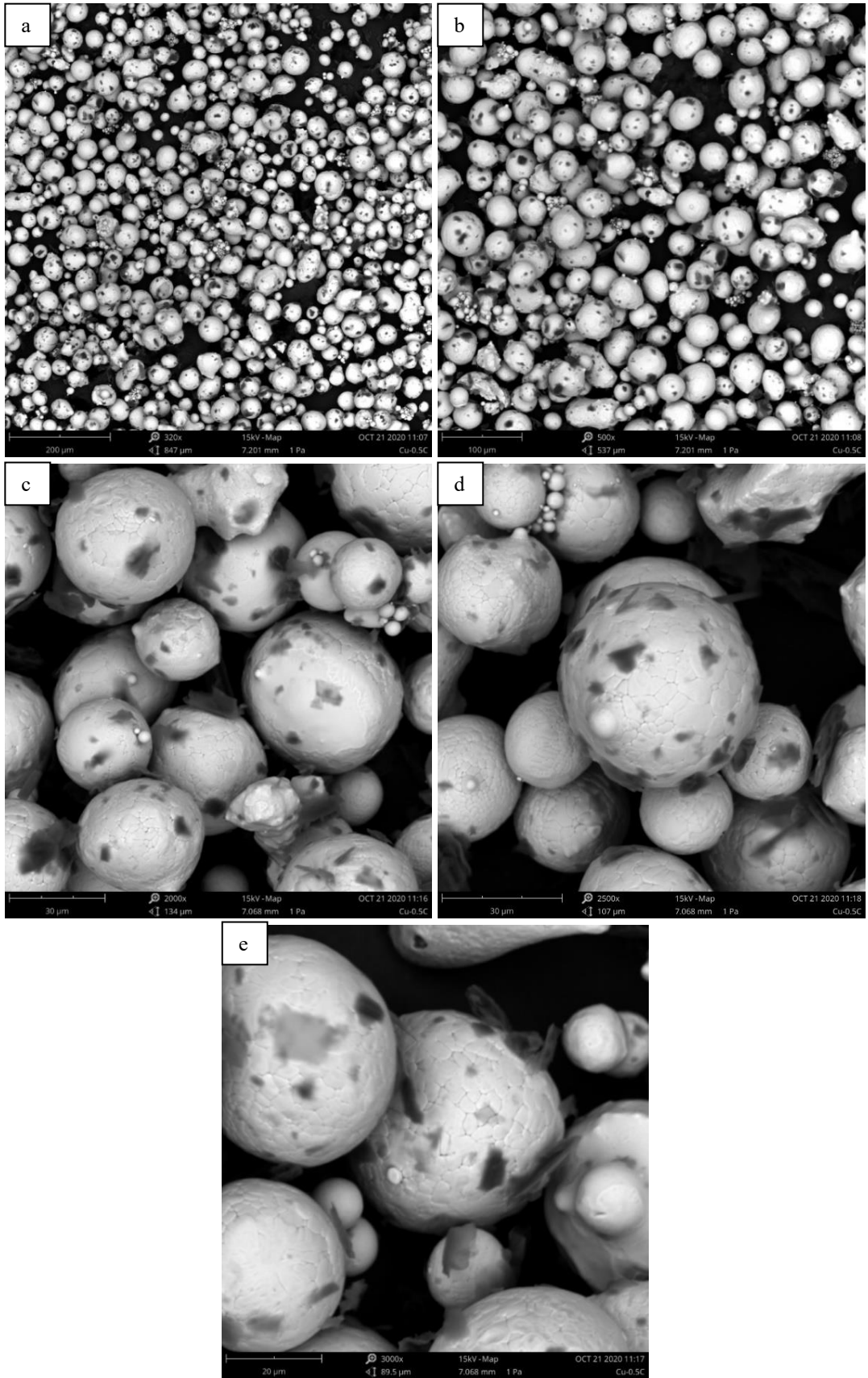


Figure A. 6 - SEM images of Cu – 0.5% C. a) 320x. b) 500x. c) 2000x. d) 2500x. e) 3000x.

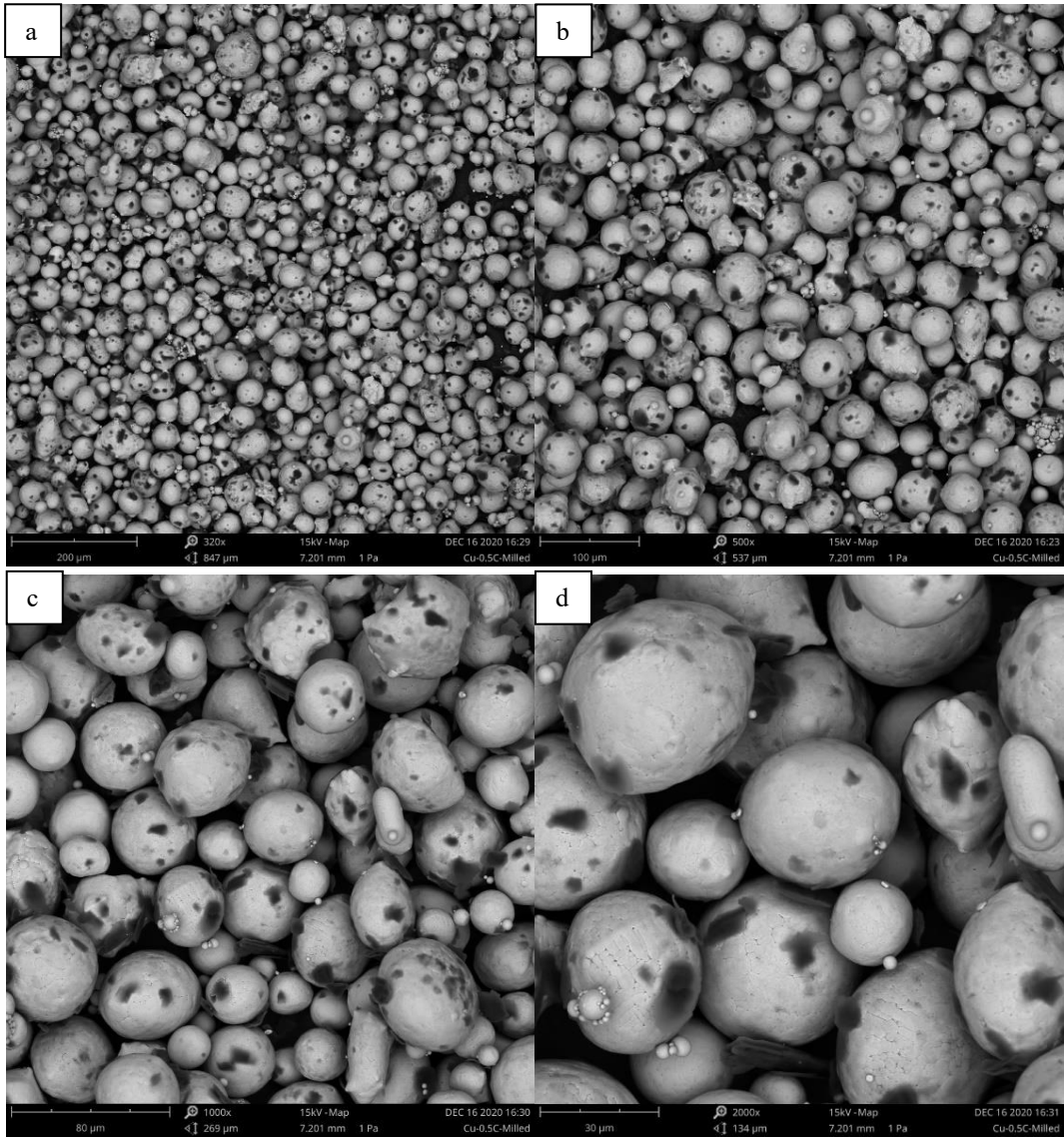


Figure A. 7 - SEM images of Cu – 0.5% milled C. a) 320x. b) 500x. c) 1000x. d) 2000x.

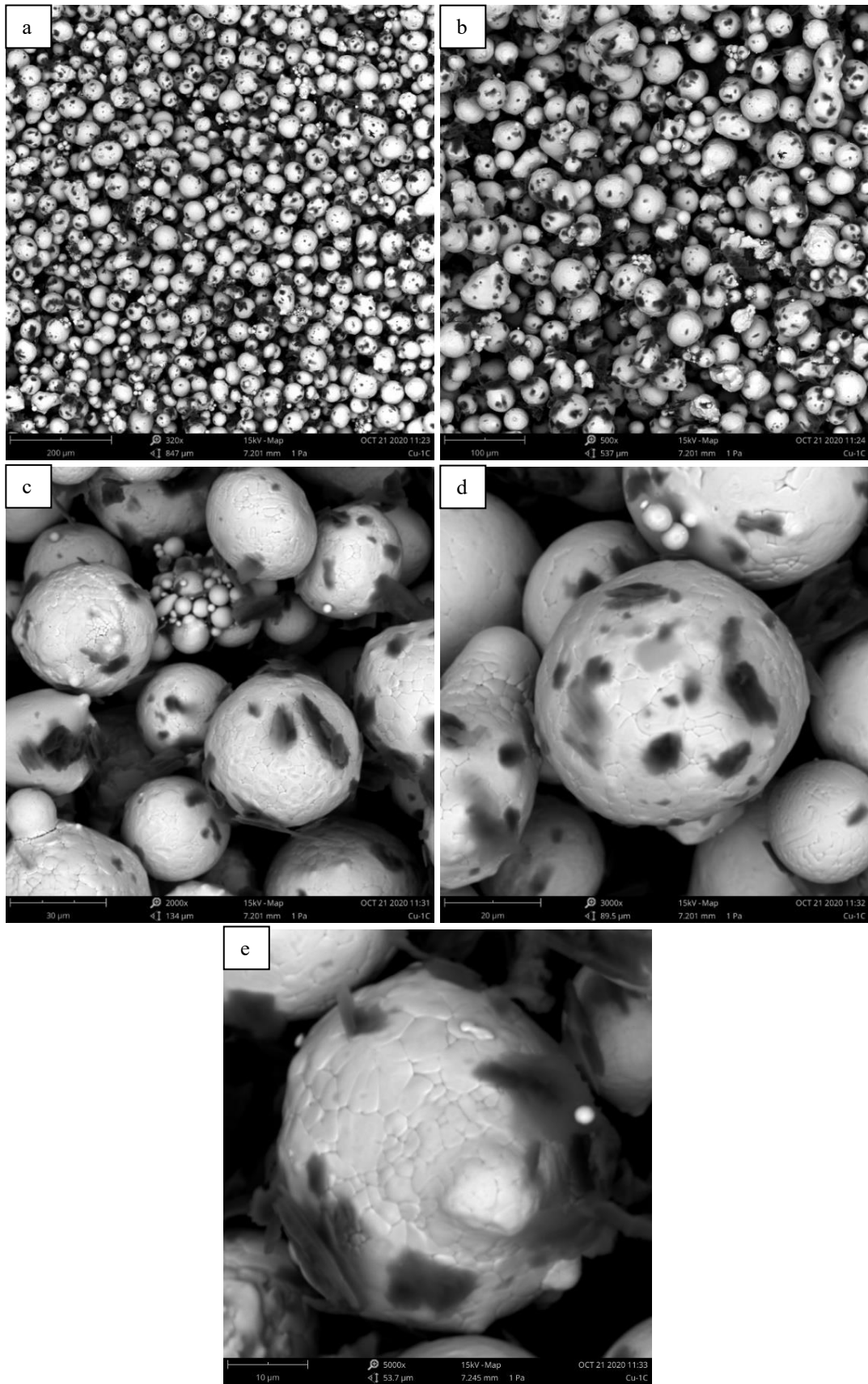


Figure A. 8 - SEM images of Cu – 1.0% C. a) 320x. b) 500x. c) 2000x. d) 3000x. e) 5000x.

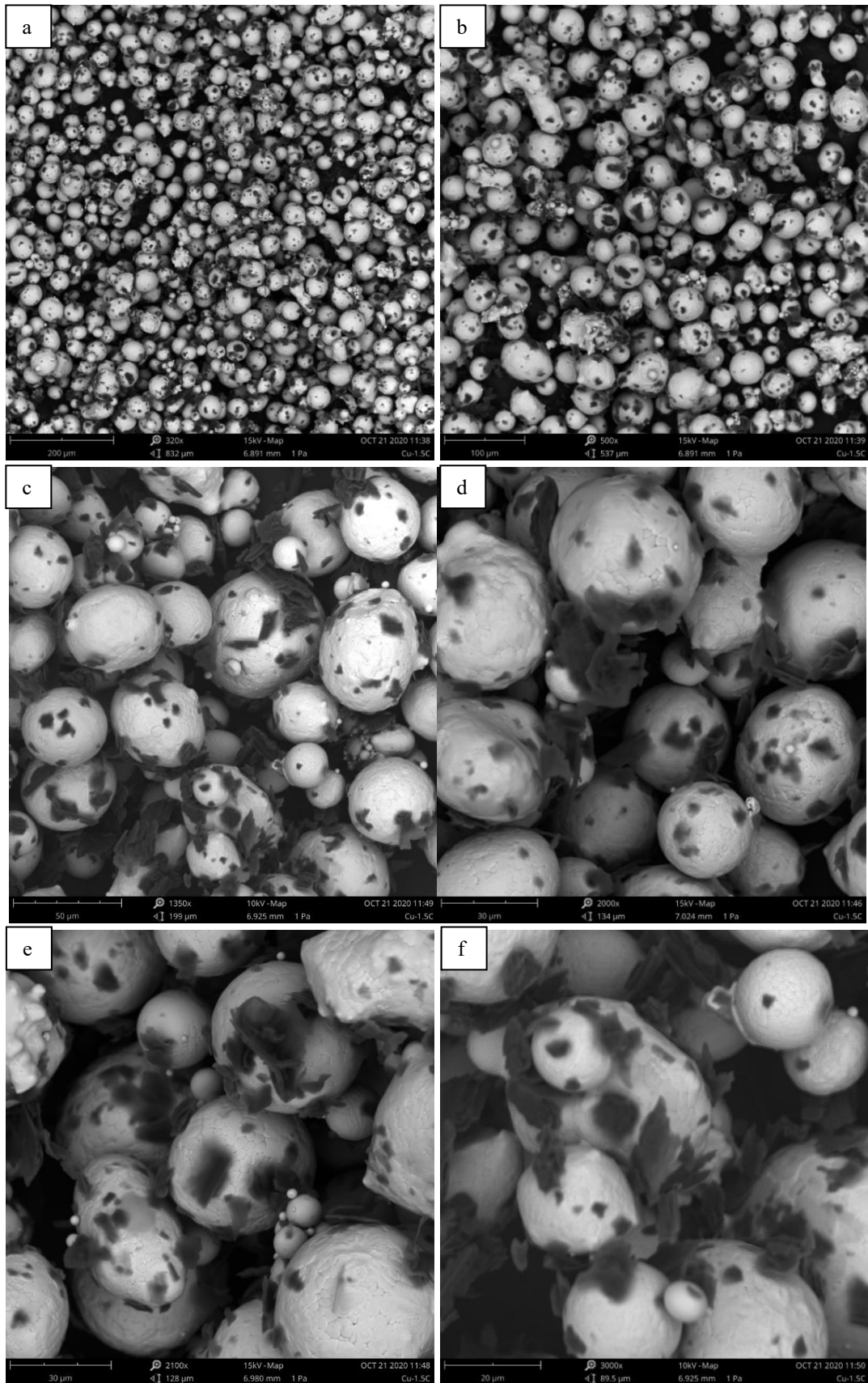


Figure A. 9 - SEM images of Cu – 1.5% C. a) 320x. b) 500x. c) 1350x. d) 2000x. e) 2100x. e) 3000x.

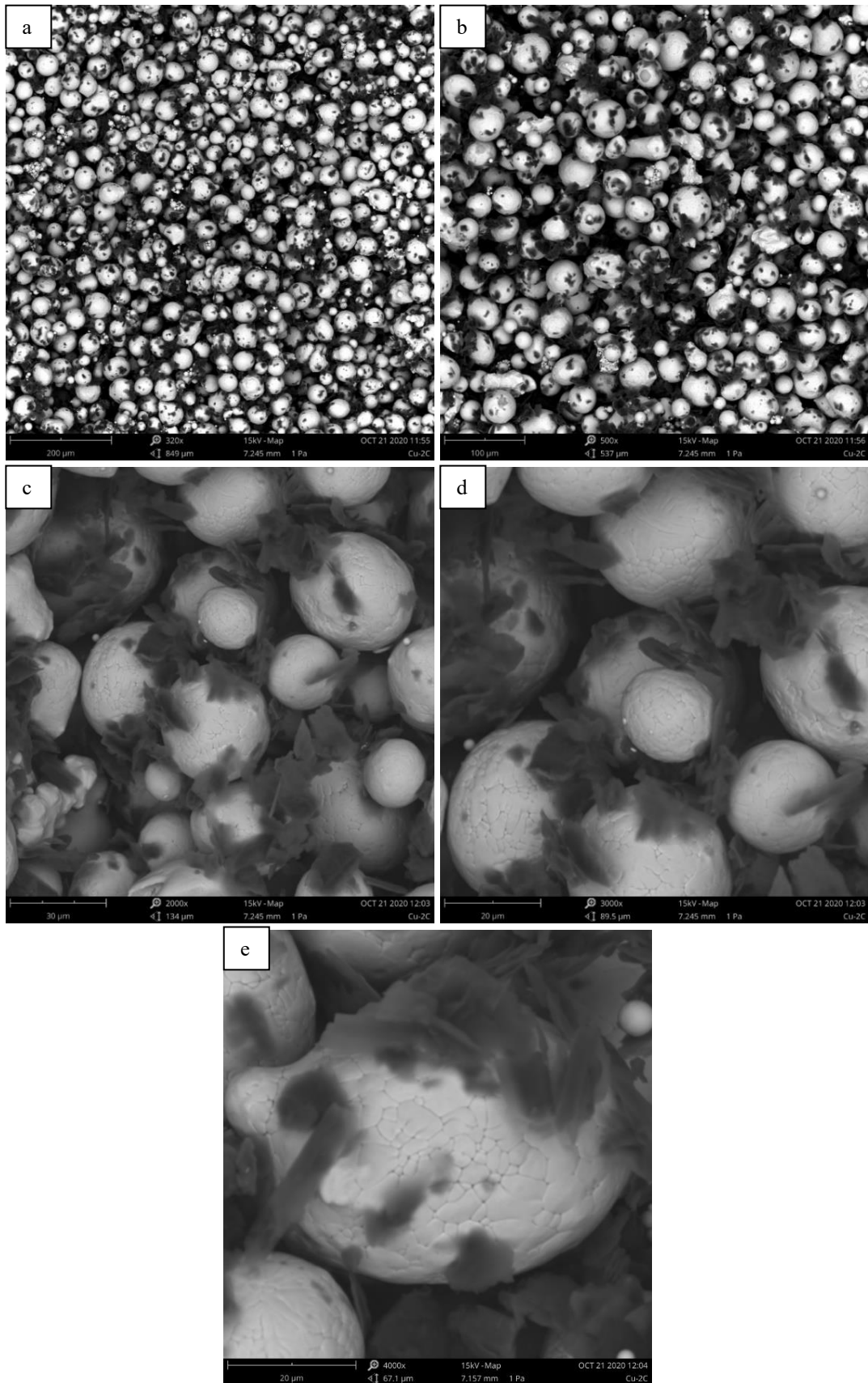


Figure A. 10 - SEM images of Cu – 2.0% C. a) 320x. b) 500x. c) 2000x. d) 3000x. e) 4000x.

# SEM chemical analysis

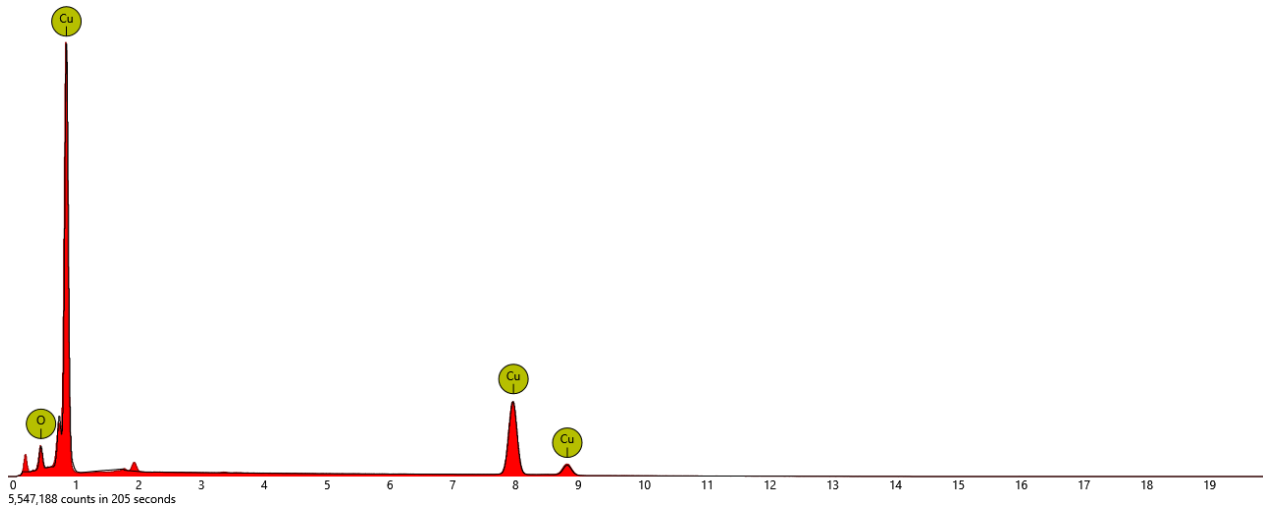


Figure A. 11 - SEM chemical analysis of pure Cu

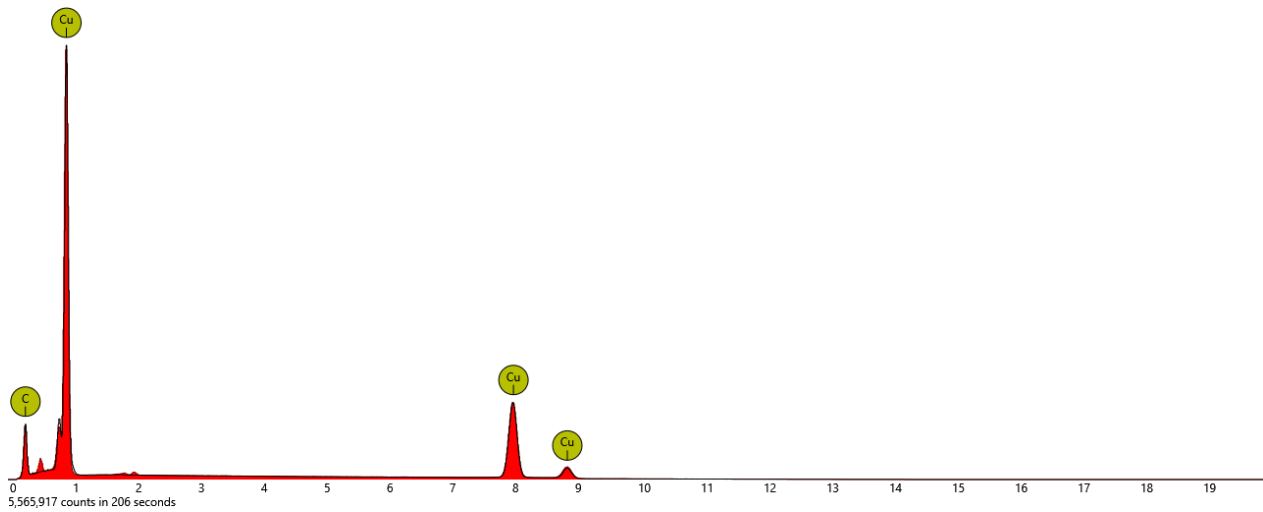


Figure A. 12 - SEM chemical analysis of Cu - 0.25% C.

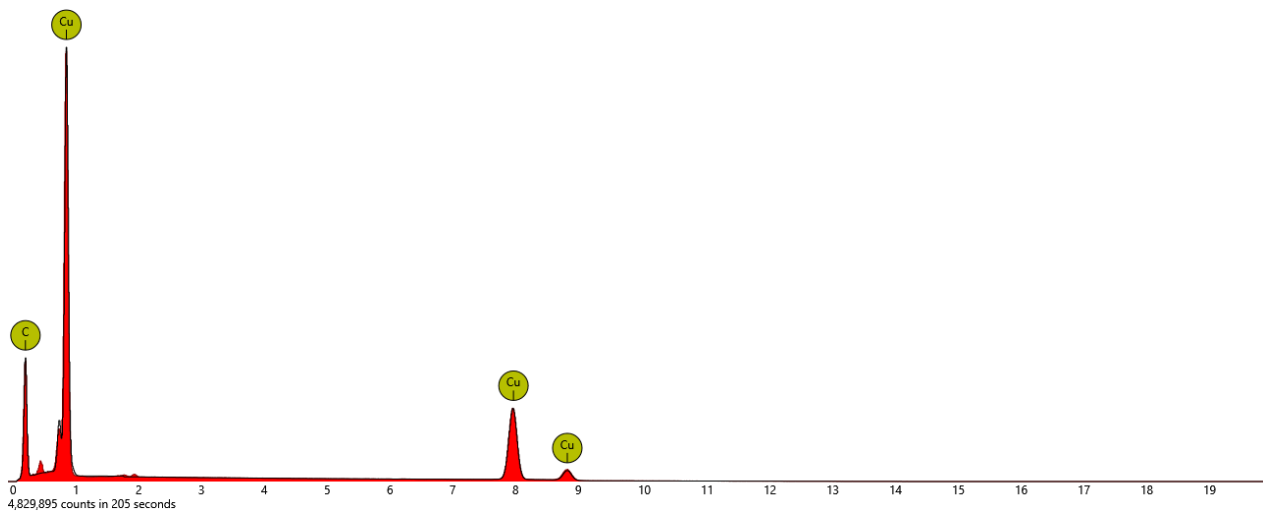


Figure A. 13 - SEM chemical analysis of Cu - 0.5% C.

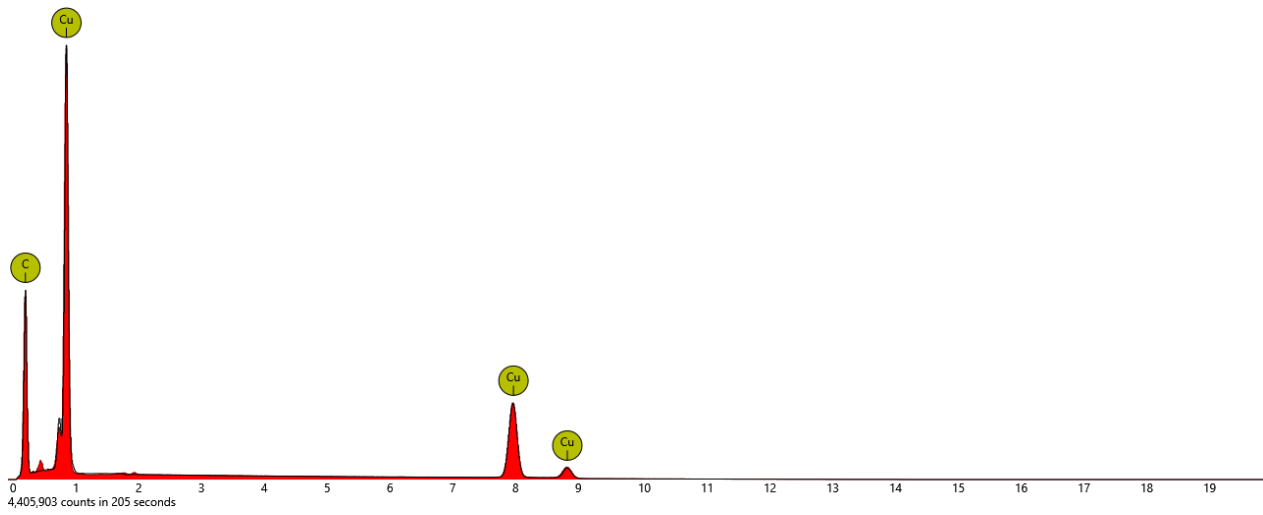


Figure A. 14 - SEM chemical analysis of Cu – 1.0% C.

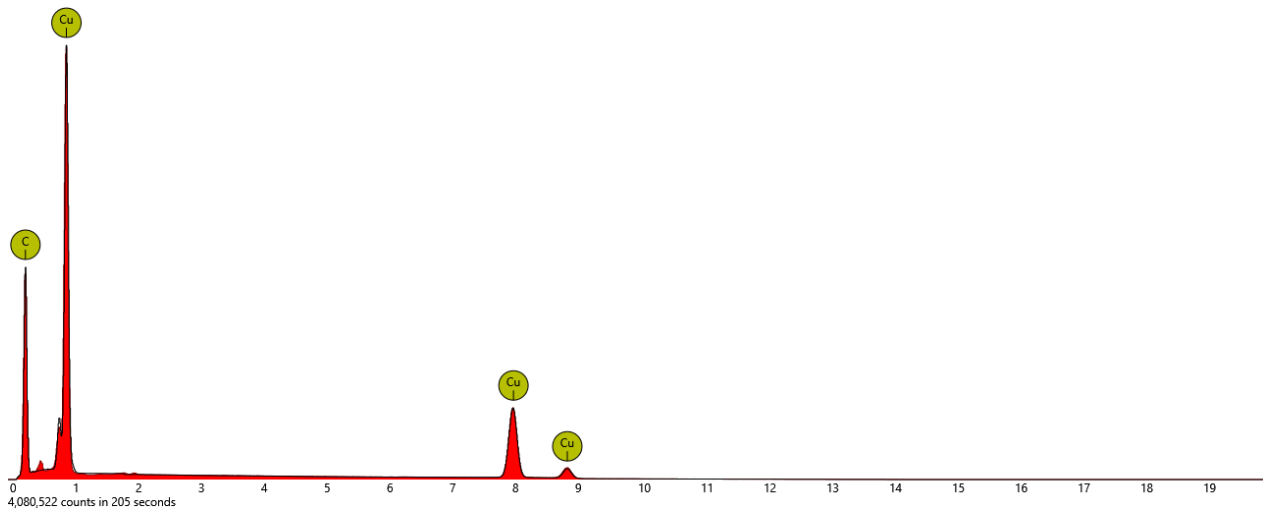


Figure A. 15 - SEM chemical analysis of Cu – 1.5% C.

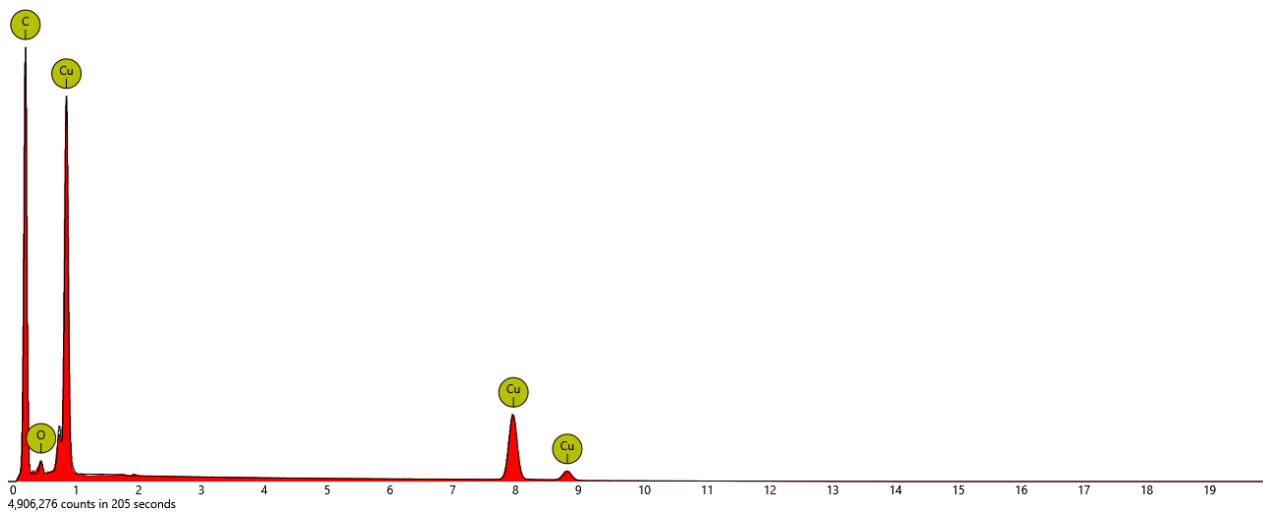
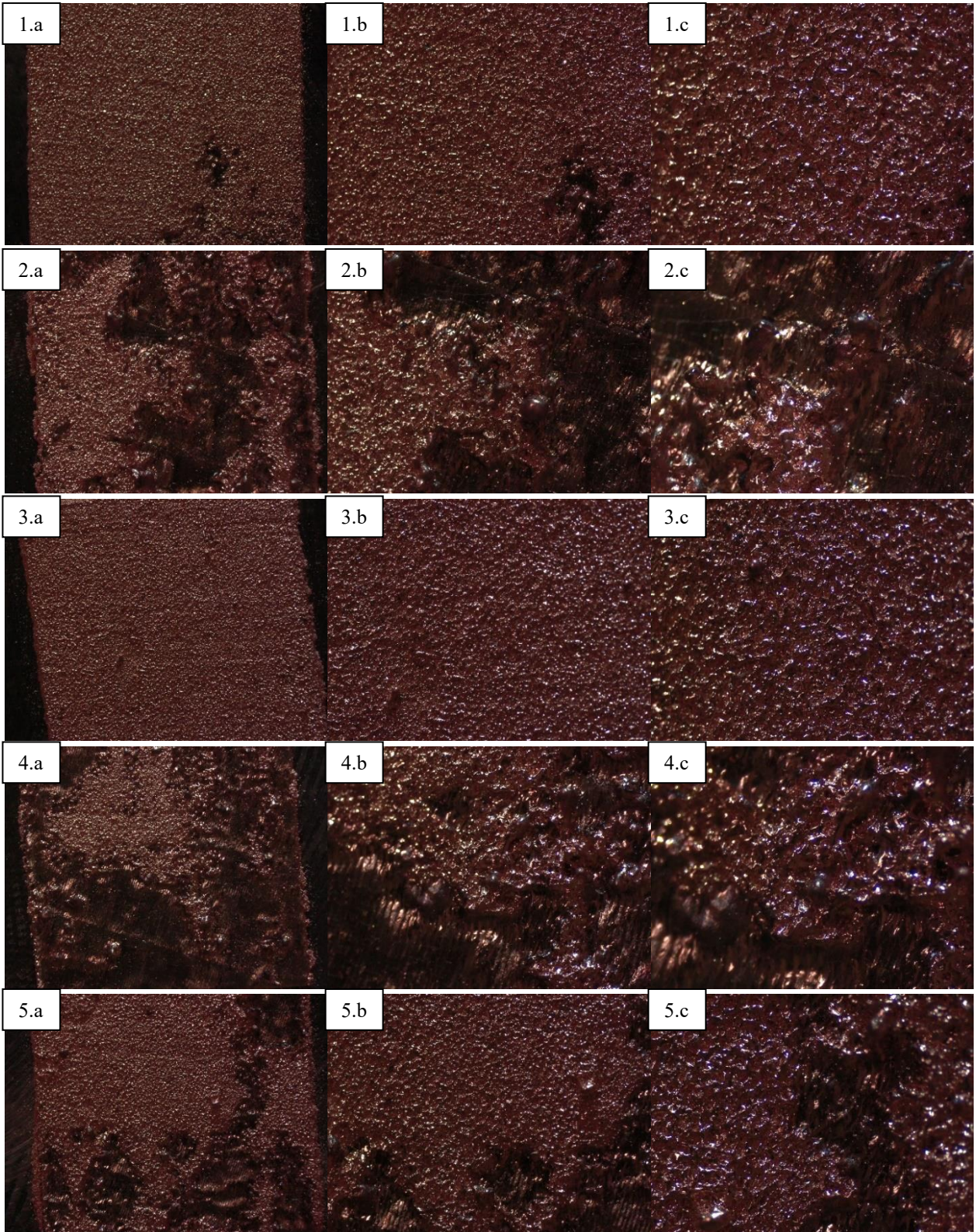


Figure A. 16 - SEM chemical analysis of Cu – 2.0% C.

# JOB 1



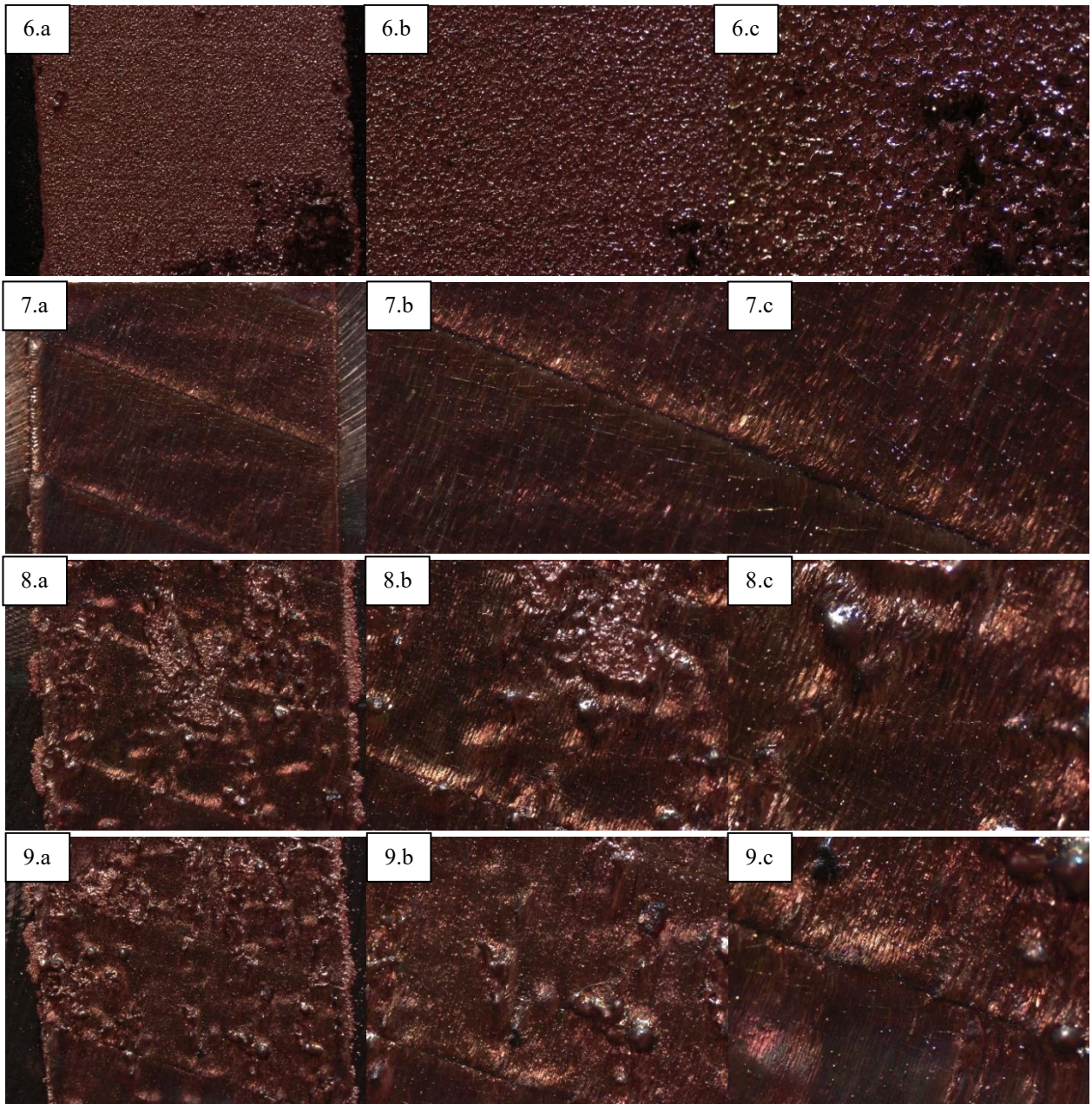
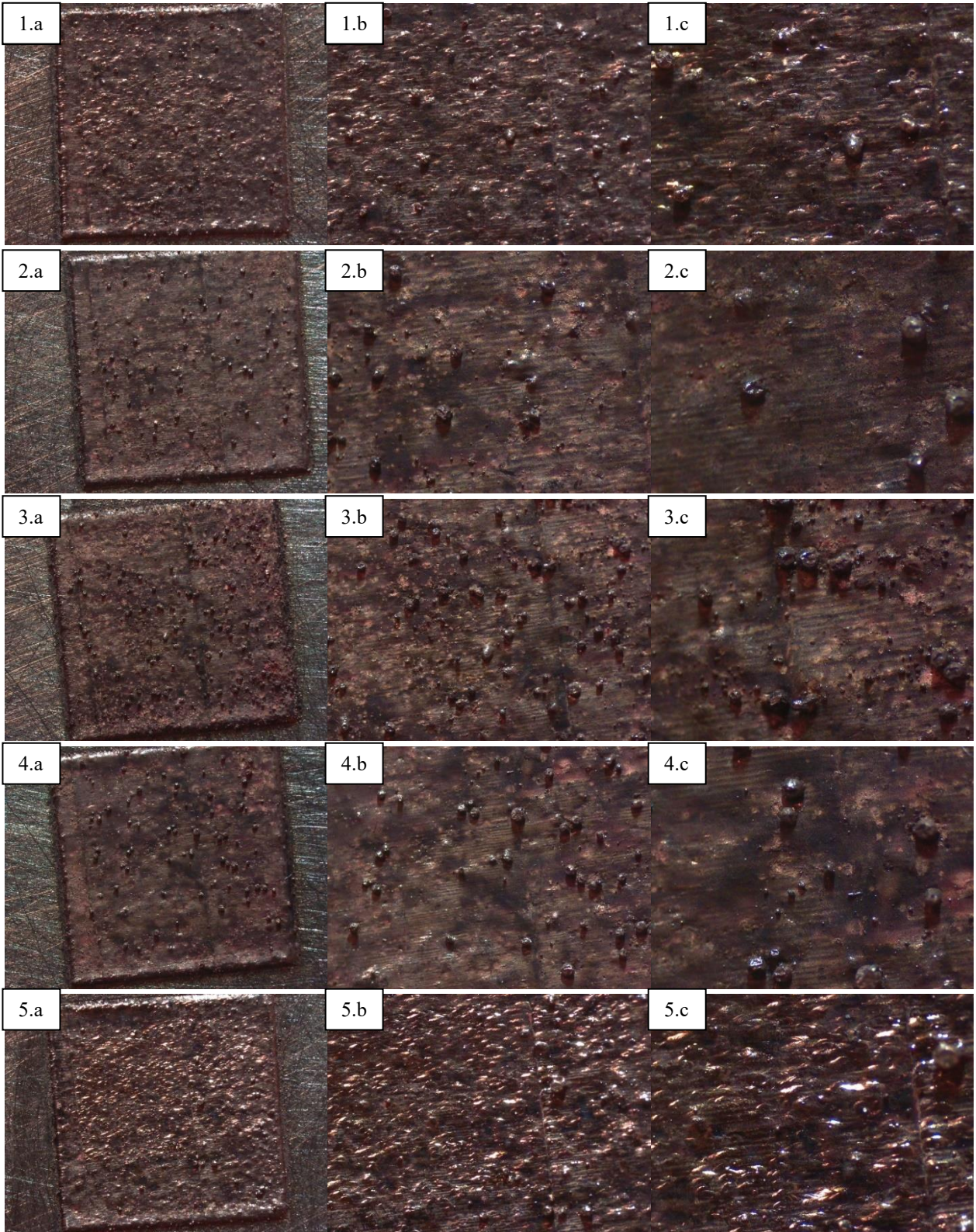
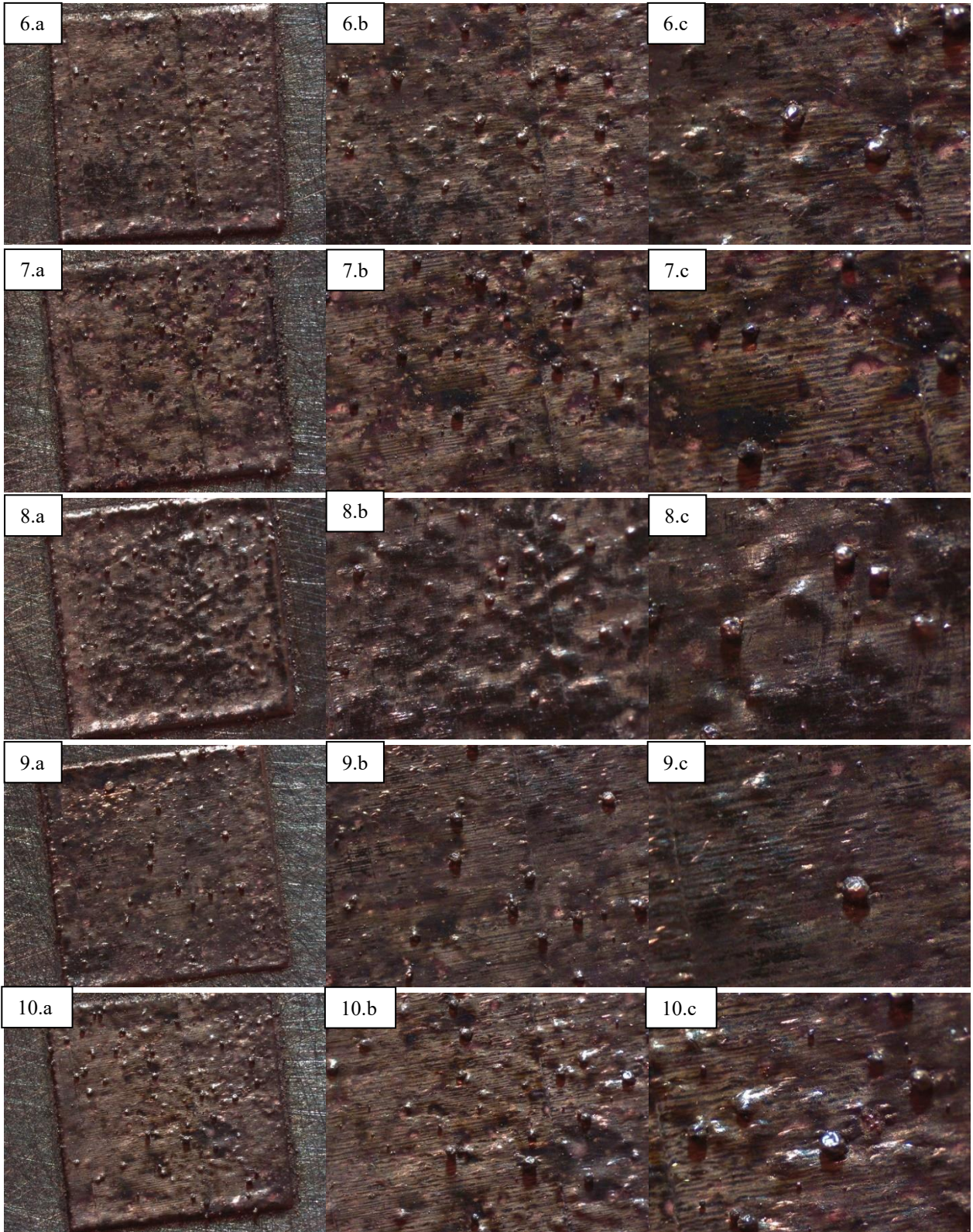
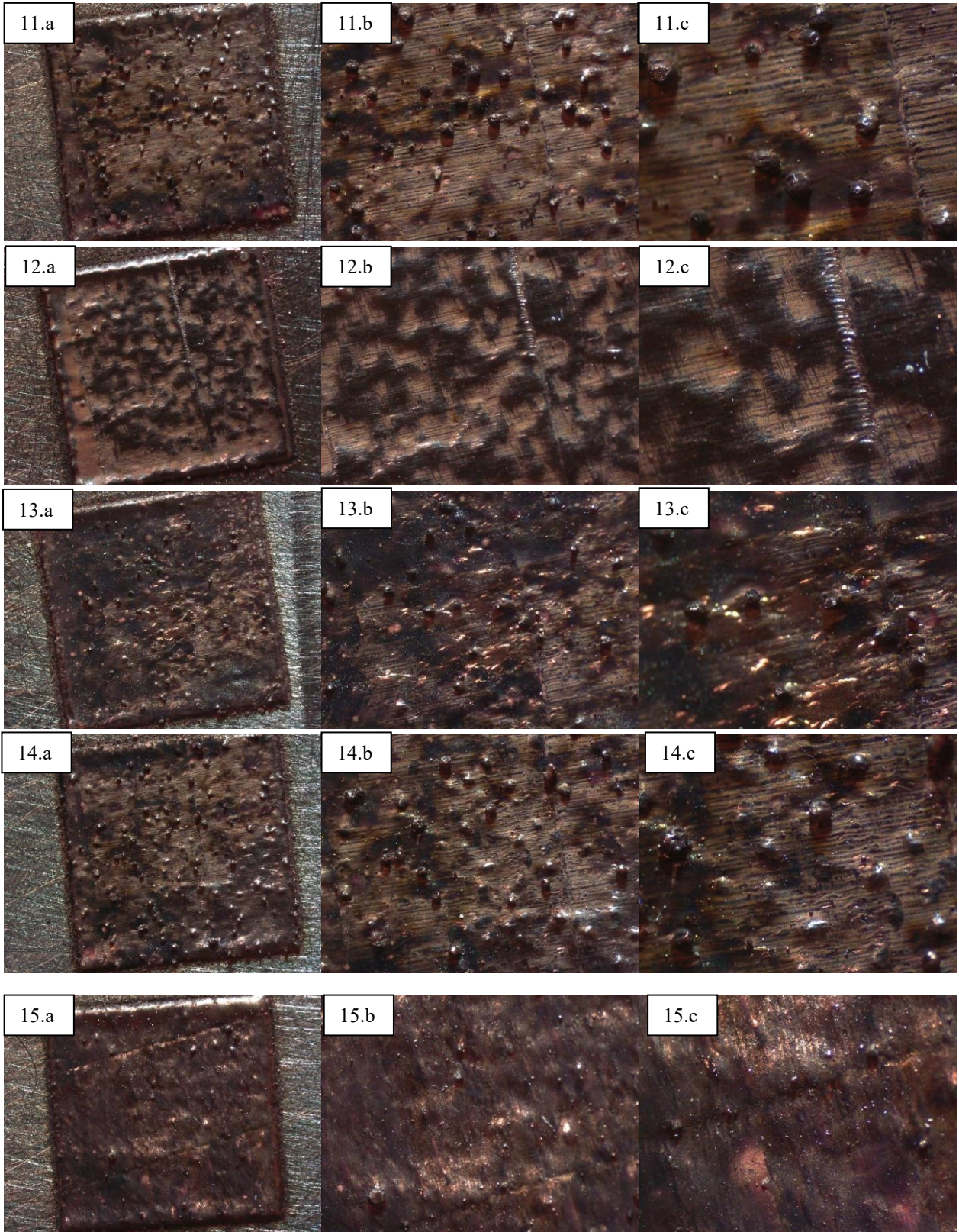


Figure A. 17 – Job 1. Samples numbered from 1 to 9. a) magnification at 1x, b) magnification at 2x, c) magnification at 4x

# JOB 2







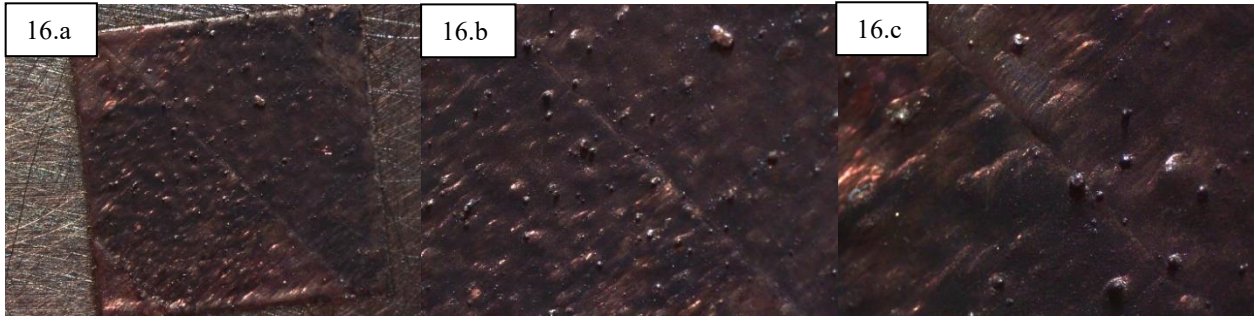
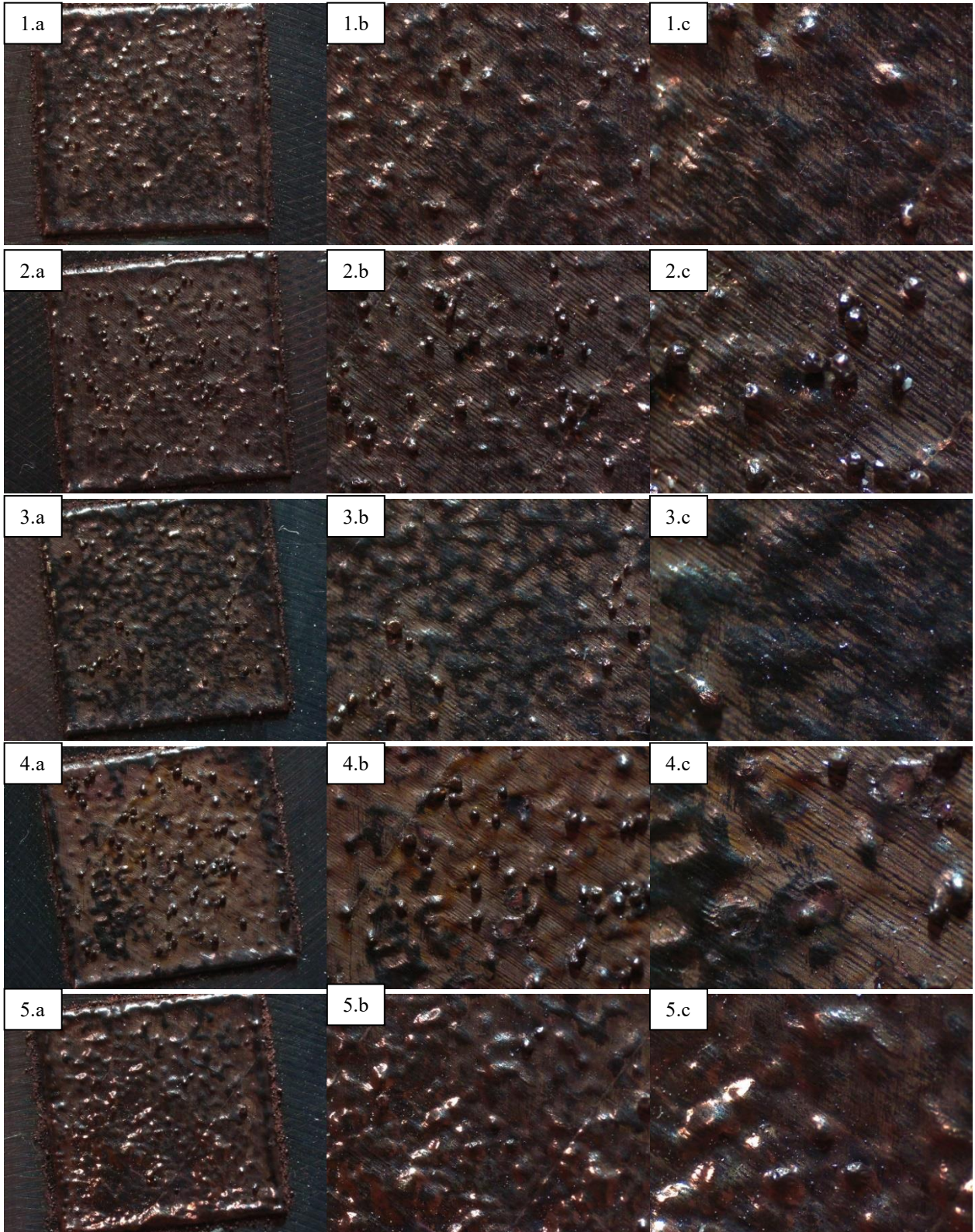


Figure A. 18 – Job 2. Samples numbered from 1 to 16. a) magnification at 1x, b) magnification at 2x, c) magnification at 4x

# JOB 3



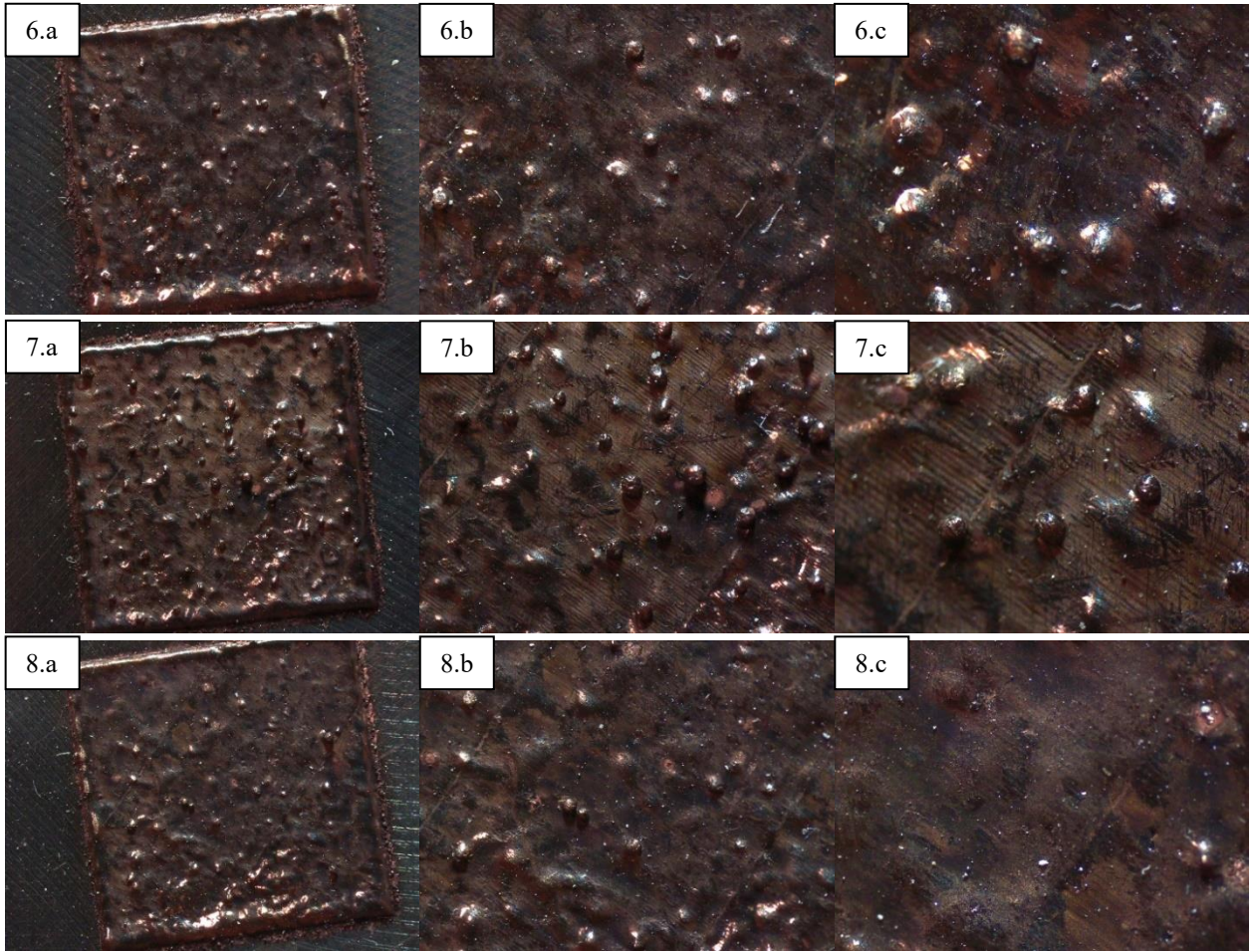
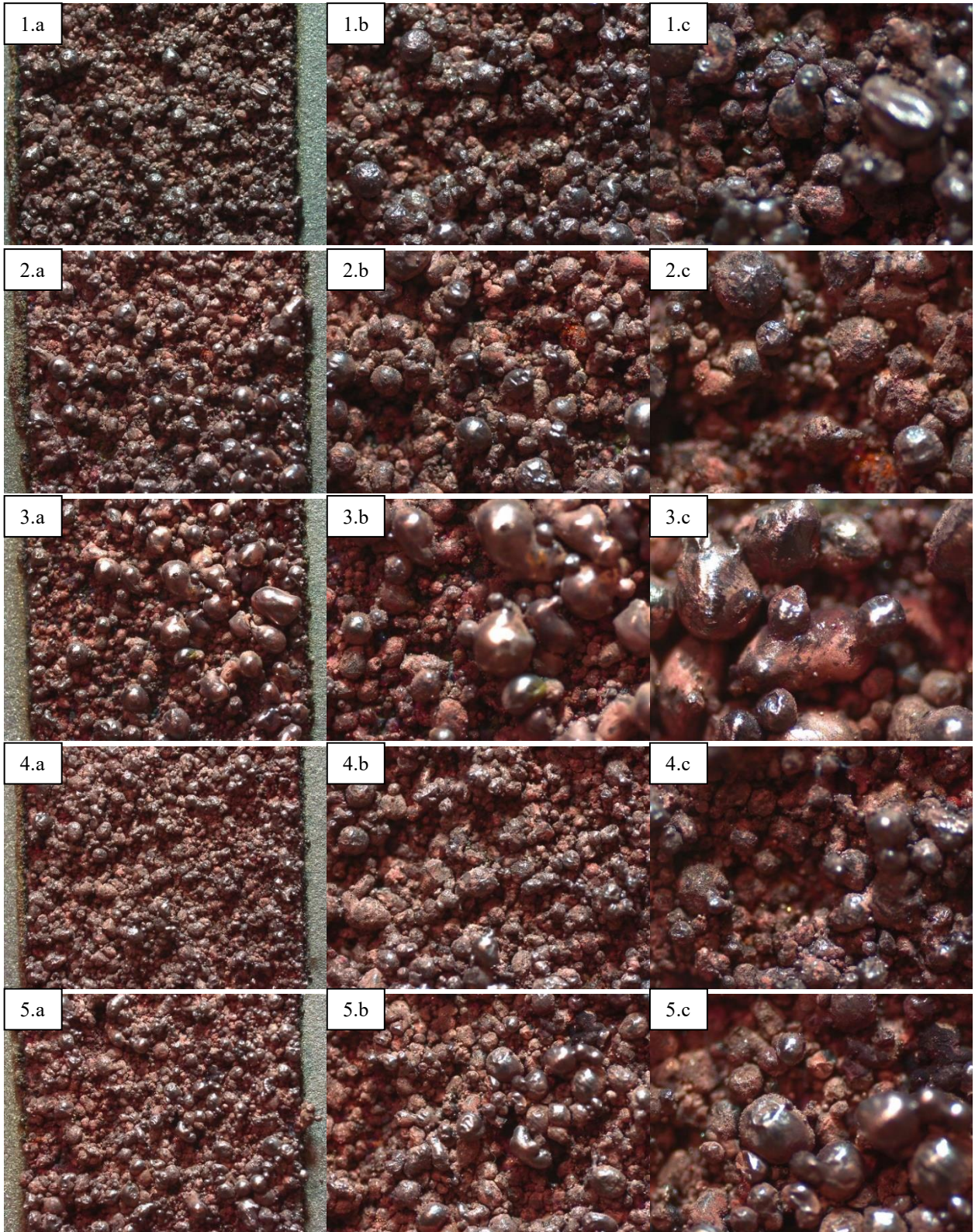


Figure A. 19 – Job 3. Samples numbered from 1 to 8. a) magnification at 1x, b) magnification at 2x, c) magnification at 4x

# JOB 4



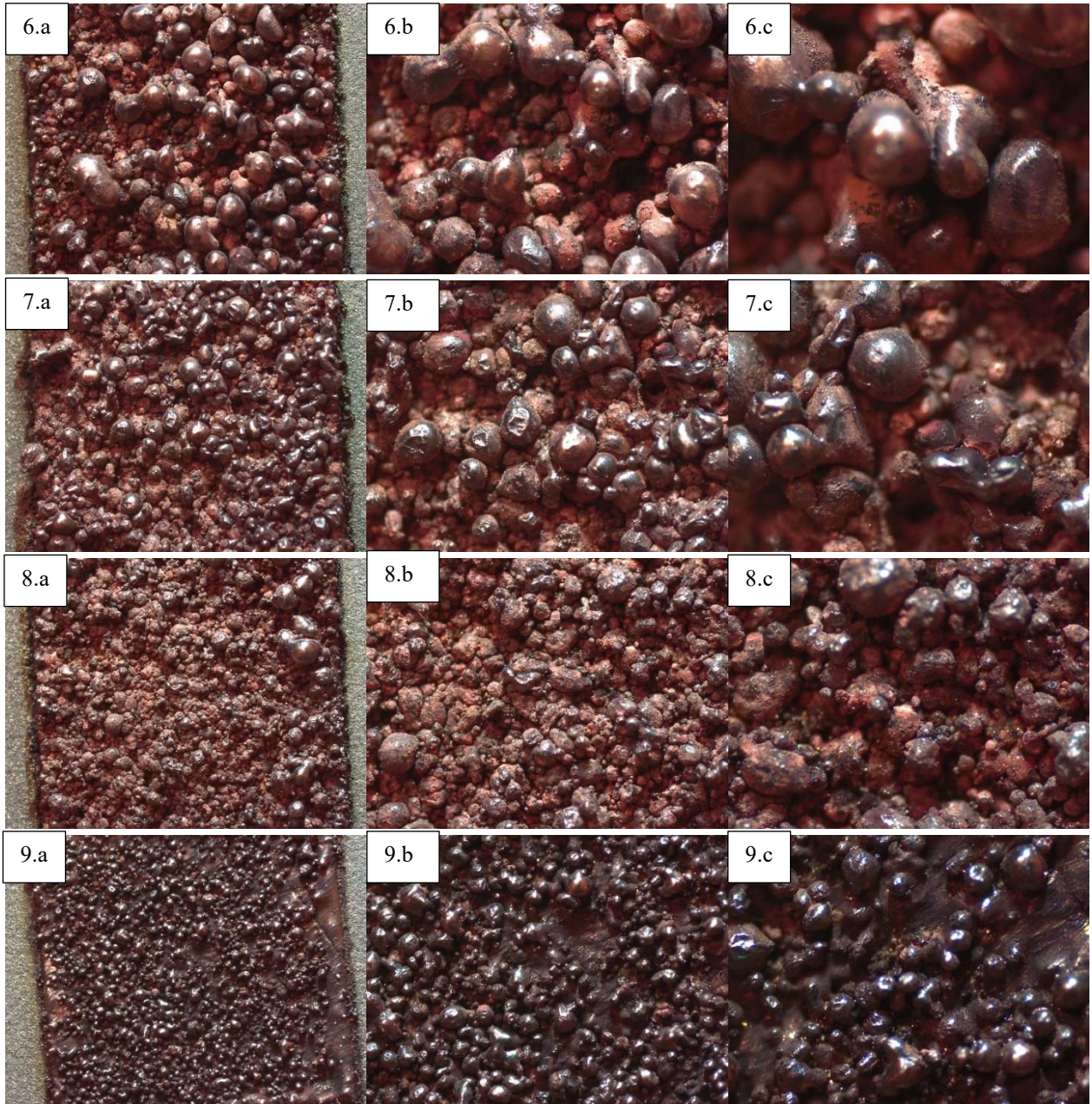


Figure A. 20 – Job 4. Samples numbered from 1 to 9. a) magnification at 1x, b) magnification at 2x, c) magnification at 4x